ABSTRACT

Title of dissertation: PROPERTIES OF METALLIC HELIMAGNETS

Kwan-Yuet Ho, Doctor of Philosophy, 2012

Dissertation directed by: Professor Theodore R. Kirkpatrick
Institute for Physical Science and Technology
and Department of Physics

This dissertation investigates various aspects of helimagnets. Helimagnets are magnets with spins aligned in helical order at low temperatures. It exists in materials of crystal structure lacking the spatial inversion symmetry. The helical order is due to the Dzyaloshinskii-Moriya (DM) mechanism. Examples of helimagnets include MnSi, FeGe and $Fe_{1-x}Co_xSi$.

A field theory appropriate for such magnets is used to derive the phase diagram in a mean-field approximation. The helical phase, the conical phase, the columnar phase and the non-Fermi-liquid (NFL) region in the paramagnetic phase are discussed. It is shown that the orientation of the helical vector along an external magnetic field within the conical phase occurs via two distinct phase transitions. The columnar phase, believed to be a Skyrmion lattice, is found to exist as Abrikosov Skyrmions near the helimagnetic phase boundary, and the core-to-core distance is estimated.

The Goldstone modes that result from the long-range order in the various phases are determined, and their consequences for electronic properties, in particu-

lar, the specific heat, single-particle relaxation rate and the electrical conductivity, are derived.

In addition, Skyrmion gases and lattices in helimagnets are studied, and the size of a Skyrmion in various phases is estimated. For isolated Skyrmions, the long distance tail is related to the magnetization correlation functions and exhibits power-law decay if the phase spontaneously breaks a continuous symmetry, but decays exponentially otherwise. The size of a Skyrmion is found to depend on a number of length scales. These length scales are related to the strength of DM interaction, the temperature, and the external magnetic field.

PROPERTIES OF METALLIC HELIMAGNETS

by

Kwan-Yuet Ho

Dissertation submitted to the Faculty of the Graduate School of the
University of Maryland, College Park in partial fulfillment
of the requirements for the degree of
Doctor of Philosophy
2012

Advisory Committee:
Professor Theodore R. Kirkpatrick, Chair/Advisor
Professor Bei Lok Hu
Professor Victor M. Yakovenko
Professor Michelle Girvan
Professor Devarajan Thirumalai (Dean's Representative)

Acknowledgments

Firstly, I would like to thank my supervisor, Prof. Theodore R. Kirkpatrick, for his guidance over the years. He is a very insightful physicist. He often challenges me with tough questions that guide me to think more deeply about the physics behind the systems I am working on. He is always available for discussion and makes constructive criticism. Besides his superb mentorship, he also demonstrates his kindness and generosity by inviting me to stay in his home as vacation. With his advice, my written English has significantly improved.

I cannot leave out Prof. Bei-lok Hu, who has helped me through in various stages of my graduate study. I worked on a project of two-dimensional Bose gas with him and Prof. Esteban Calzetta, before starting this dissertation project on helimagnets. Understanding my academic background that applied mathematics was the emphasis, he always stresses that I should have a physical picture in mind. He gave me a lot of advice about how to conduct scientific study.

I would like to thank Prof. Dietrich Belitz (in University of Oregon). Although I have not met him in person, he was very helpful in many aspects of this research project. He also passed a lot of job advertisements to me.

I also owe my gratitude to Prof. Esteban Calzetta (in Universidad de Buenos Aires-Ciudad Universitaria, Argentina), whom I collaborated with on the project of two-dimensional Bose gas. He is very patient that he explains theories and novel ideas clearly with details in electronic mails. He is so devoted to research that even during vacation trips he was eager to discuss physics.

I want to thank also to Prof. Lin Tian (in University of California, Merced), who introduced me to my first research project in my first year in Maryland.

I have to thank Prof. Chi Kwong Law (in The Chinese University of Hong Kong) for his supervision on my undergraduate final year project. He shared his experience of pursuing graduate study to prepare me the right attitude upon studying in Maryland. Every time I visit him in Hong Kong, he never hesitates to give me invaluable advice. I had the right attitude upon entering school in Maryland.

I would also like to thank all the graduate students in the Department of Physics. Anand Ramanathan provided me with details about the experiments he conducted, which are useful for my first published journal paper. I enjoyed discussing physics with Christopher Bertrand, who is friendly and helpful. I learned a lot in discussions with Meng Cheng, who is young, bright and energetic, about topology and its applications to condensed matter physics. I learned a lot from the discussions with Wang Kong Tse, who is very knowledgeable, and his industry motivates me a lot. Nathan Orloff is very nice in sharing about his experience of being a research scientist with me. Discussions with King Lam Hui, a biophysicist who is intelligent and humble, often inspires me to think in a different way. I enjoyed the time with Anzi Hu and Kaushik Mitra during my stay in NIST, whom I learned a lot from. I cannot forget the discussions with Jianhao Chen, Yi Cai and Wenxi Zhu. Last but not least, I owe my very gratitude to Sheung Wah Ng, who helped me through in settling down in the College Park area.

I would like to also thank my friends who are graduate students in other departments from Hong Kong in Maryland. I have to thank especially to Kan

Leung Cheng, my previous housemate, whom I have spent a lot of days through frustration in work and life over the years. I want to thank also to Kin Keung Ma, Cheuk Yiu Ip, Wai Shing Lee, Ching Pui Hung, Xuwen Chen, Yuk Hei Chan, Aaron Chan, Benedict Chan, Yue Hei Ng, Wai Lim Ku, Kayi Hui, Eva Yiu, Pui Yu Ling and Tak Chu Li. They have helped me passing many boring and lonely days in Maryland. Without their continuous encouragement and support, this thesis would never be possible.

I would like to thank my parents, who have supported me with unconditional love. Without their sacrifice and understanding, I would not have received such a good education and had the opportunity of going to school in Maryland.

I would like to thank my girlfriend, Sin Man Ng, for her continuous support in my dissertation work. She is considerate and smart. She is a good helper, who alleviates my stress by helping out on some of the daily necessity. We grow together in Christ, by mutually exchanging ideas about our understanding of God and endless encouragement. Her love is always a motivation for me to do better.

I would also like to express my gratitude to all the brothers and sisters in Christ in Greenbelt Fellowship, Chinese Bible Church of College Park. I have been growing with maturity in the fellowship. The fellowship imparts me with a right attitude in dealing with people and pursuing knowledge.

There are not enough trees to make paper for me to express my gratitude to people whom I have left out. Life is so good that I can say the words of thanksgiving day by day. I have to thank God for bringing me here from my home far away so that I learned how to rely on Him solely. He taught me with His Words and discipline

so that I can grow spiritually. He is so good that I am overwhelmed with His divine blessings and provision from time to time.

Table of Contents

List of Figures

Chapter 1

Introduction

1.1 History of magnetism

Magnets have been known since the beginning of human civilizations. A magnetic needle aligns with Earth's magnetic field, defining the astronomical true north. They have been used as compasses for navigation since the Age of Discovery in Western Europe in the 15th century. Despite its widespread application since the ancient times, the physics of magnetism was not understood until the 19th century when the theory of electromagnetism was constructed. Under the framework of Maxwell's equations, the motion of charged particles in a magnetic field can be described, [1] but the origin of magnetic dipoles in materials was still not given. The born of quantum mechanics in the 20th century increased our understanding on atomic structure. The magnetic behavior of a solid is now understood to be the collective effects of the magnetic dipoles produced by the orbital electrons, their spins, and the presence of external magnetic field. [2]

There are many kinds of magnetism. In paramagnetism, the magnetic dipoles align along the external magnetic field; whereas in diamagnetism, the dipoles align opposite to the field. In both cases, the dipoles arrange in random directions without any magnetic field, leading to a net zero magnetization.

There are, however, also spontaneous ordered arrangements of magnetic spin

even without magnetic field. In ferromagnetism, the magnetic dipoles tend to align in a certain direction even without an external magnetic field. This is due to the interaction between spins within the material. However, ferromagnetism is destroyed by thermal agitation. Above the Curie temperature, a material that exhibits ferromagnetism at lower temperature becomes paramagnetic. Antiferromagnetism is similar, except that the consecutive dipoles align in opposite directions and the transition temperature is called the Néel temperature.

1.2 Helimagnetism

Helimagnetism is another example of spontaneous ordered state, which we will focus in this thesis. The most well-known helimagnet is manganese silicide (MnSi).

MnSi is a B20 cubic crystal with space group $P2_13$, in which there is no spatial inversion symmetry, as shown in Fig. 2.1. It was found that MnSi was ordered below the temperature 30 K. [3] It was first classified as a weak itinerant ferromagnet. It was also suggested to be antiferromagnetic from its response to the magnetic field, but no additional magnetic reflections have ever been detected by neutron diffraction. [4] In 1976, a high resolution neutron diffraction study of MnSi was carried out. [5] The neutron beam was perpendicular to the applied magnetic field. Fig. 1.1 shows one of the typical measurement results. The solid circles in the figures indicate the peak positions of the Bragg reflections. The results of zero magnetic field show that there are peaks in four $\langle 111 \rangle$, separated from the center

by 0.035 $\mathring{\text{A}}^{-1}$. [1] This indicates MnSi has a helical spin structure [6] with a period of 180 $\mathring{\text{A}}$ in the $\langle 111 \rangle$ direction when $H = 0$, while the lattice constant is 4.56 $\mathring{\text{A}}$, see Table 1.1. The spin structure is shown in Fig. 1.2. A real-space Lorentz TEM image of the helimagnet $Fe_{0.5}Co_{0.5}Si$ was taken by Uchida *et. al.*, as shown in Fig. 1.3. [7, 8]

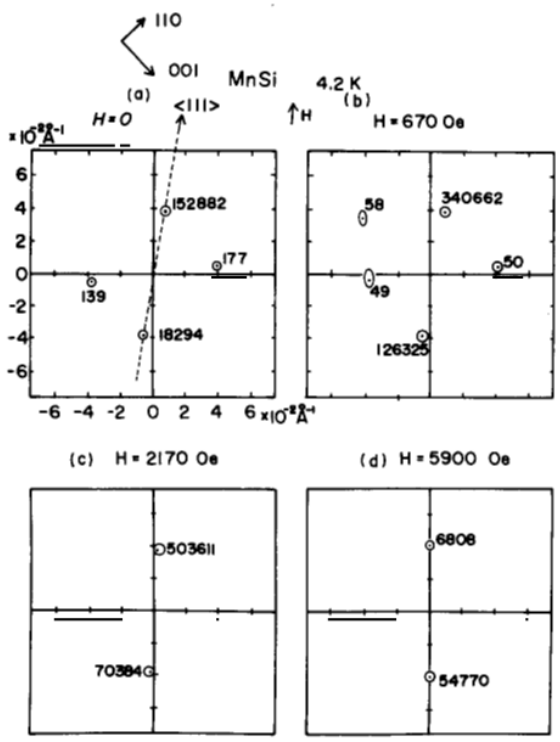

Figure 1.1: Neutron diffraction patterns of MnSi at 4.2 K for different magnetic fields (H). The magnetic field is applied along the vertical axis (close to $\langle 111 \rangle$ direction.)

Such helical order can be explained by the Dzyaloshinskii-Moriya (DM) mechanism, [9, 10] due to spin-orbit coupling. [11] It is written in terms of $\int d^3x\, \mathbf{M} \cdot \nabla \times \mathbf{M}$, which is allowed by symmetry in MnSi since its lattice structure lacks inversion sym-

[1] The difference in the peak intensity between satellites in the [111] direction was due to a slight misorientation of the sample. [5]

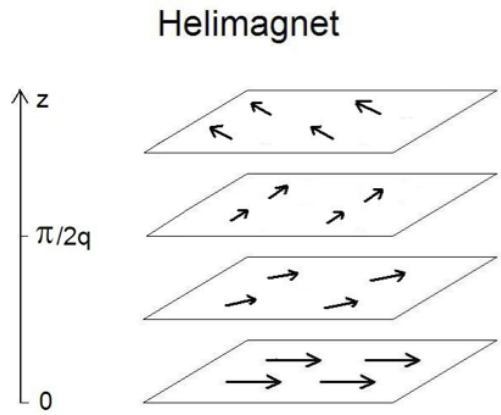

Figure 1.2: Mangetic ordering in a helimagnet. On each plane, there is a ferromagnetic order, but the direction of magnetization rotates along the helical direction. The arrow denotes the direction of the helix.

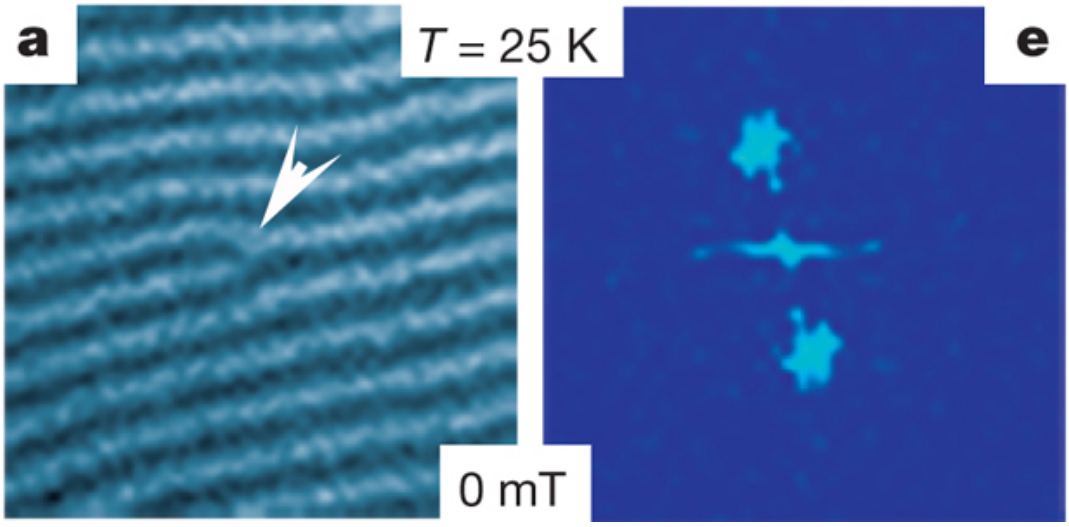

Figure 1.3: Lorentz TEM image of $Fe_{0.5}Co_{0.5}Si$ (left). The magnetic field is applied normal to the plane. The bright and dark colors refer to different directions of the spin. The helix is approximately vertical in the figure. The arrow indicates a dislocation. The corresponding FFT image is also plotted. (right)

metry. [12] As in Fig. 1.2, on any given plane perpendicular to the helix, there is ferromagnetic order, but the direction of the magnetization rotates as one goes along the direction of the helix. The helix is characterized by the pitch vector, denoted by $\mathbf{q}$. Its direction is the direction of the helix. Its modulus $q = |\mathbf{q}|$ is the helical wavenumber, where $\frac{2\pi}{q}$ is the helical wavelength, describing the distance that the ferromagnetic order repeats itself.

There are other metals and alloys exhibiting this kind of helical order at low temperatures. Examples include $Mn_{1-x}Fe_xSi$, [13] FeGe [14] and $Fe_{1-x}Co_xSi$ (for x between 0.2 and 0.95).[15, 16] Their transition temperatures, helical wavelength and lattice constants are tabulated in Table 1.1. A crystal of MnSi grown for experiments are shown in Fig. 1.4. The helical wavelength are typically 100 times larger than

Figure 1.4: A crystal of MnSi grown for experimental purpose.

the lattice constant. [2]

Increasing the magnetic field introduces a homogeneous component of the magnetic order, and for some helimagnets such as MnSi and FeGe, tilts the pitch vector $\mathbf{q}$ to the direction of the magnetic field. This is called the conical phase, as

[2]These helimagnets are known as Dzyaloshinskii-Moriya (DM) magnets. The DM interaction is due to spin-orbit coupling, as stated in Chapter 2. However, there are also helimagnets realized, such as $FeCl_3$ [17] and MnO_2, [18] that their helical wavelengths are of the same order as or at most 10 times the lattice constants. Helimagnetism of this kind is realized in XY model with nearest and second nearest neighbor coupling. [19, 20, 21]

shown in Fig. 1.5. Thermal agitation and a large external magnetic field destroy the helical order, and restore paramagnetism or ferromagnetism.

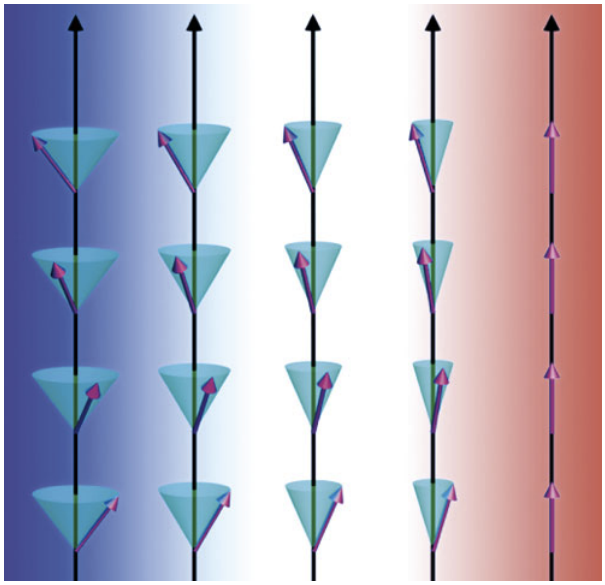

Figure 1.5: Conical phase in helimagnets. When the external magnetic field increases (from left to right), the homogeneous component of magnization increases and the helimagnetic amplitude decreases. (adapted from Ref. [22])

These helimagnets are also highly clean. For example, for MnSi, the value of $k_{\mathrm{F}}l \approx 3000$. [23] This makes the theoretical study of the transport properties in the ballistic weak disorder experimentally relevant. (See Chapter 5.)

Similar helical structures can also be found in cholestoric liquid crystal. Even the defects in cholesterics are also similar to the one in Fig. 1.3. [24]

A summary of the properties of MnSi can be found in Ref. [25].

Table 1.1: Lattice constants (a), helical wavelengths (Å) and transition temperature (T_c) of various DM helimagnets.

Material	a (Å)	$\frac{2\pi}{q}$ (Å)	T_c (K)
MnSi	4.56	180	29.5
FeGe	4.70	700	278.7
$Fe_{0.5}Co_{0.5}Si$	3.20	900	43.5
$Fe_{0.65}Co_{0.35}Si$	4.47	471	58.8
$Fe_{0.8}Co_{0.2}Si$	4.48	295	32.2
$Mn_{0.9}Fe_{0.1}Si$	4.55	100	6.8

1.3 Phase diagrams of helimagnets

The presense of DM interaction makes the phase diagram of helimagnets much richer than the other metals. The interaction, which is responsible for the helical order, is induced by spin-orbit coupling [11] characterized by a small dimensionless constant $g_{\rm so}$. Because the crystal-field effects are also due to spin-orbit coupling but of higher orders ($g_{\rm so}^2$), there should be some additional effects on the magnetic ordering.

The phase diagrams of MnSi, FeGe, $Fe_{0.5}Co_{0.5}Si$ and $Fe_{0.8}Co_{0.2}Si$ are shown in Figs. 1.6, [26] 1.7,[27] 1.8 [8] and 1.9 [16] respectively. For these helimagnets, $\mathbf{q}$ is in $\langle 111\rangle$ direction when there is no applied magnetic field. Increasing the magnetic field tilts $\mathbf{q}$ from $\langle 111\rangle$ direction to $\langle 001\rangle$ direction at a critical field H_{c1}. Further increasing the field increases the homogeneous magnetization and decreases the helimagnet which vanishes at another critical field H_{c2}. (See Chapter 3.) There

is a columnar phase [3] in all these diagams, which will be discussed in later parts of this thesis.

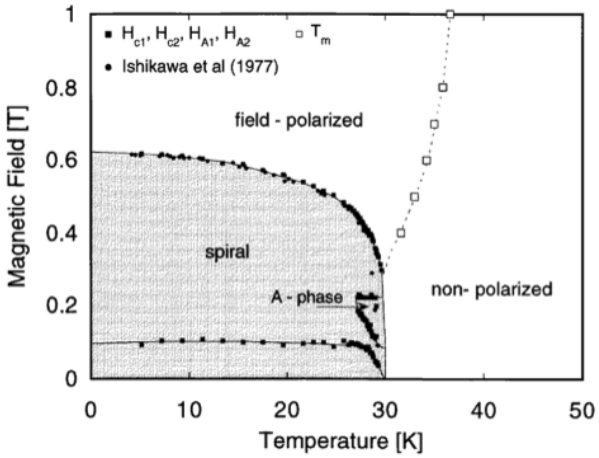

Figure 1.6: Phase diagram of MnSi.

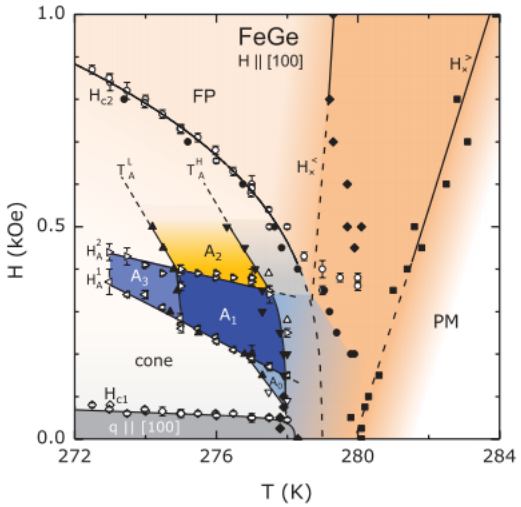

Figure 1.7: Phase diagram of FeGe.

Another interesting aspect of helimagnets such as MnSi is its sensitivity to hydrostatic pressure. With increasing pressure, the transition temperature T_c de-

[3]The columnar phase is also refereed to as "A phase" in the literature. The labels "A phase" in the figures in this thesis are the columnar phases.

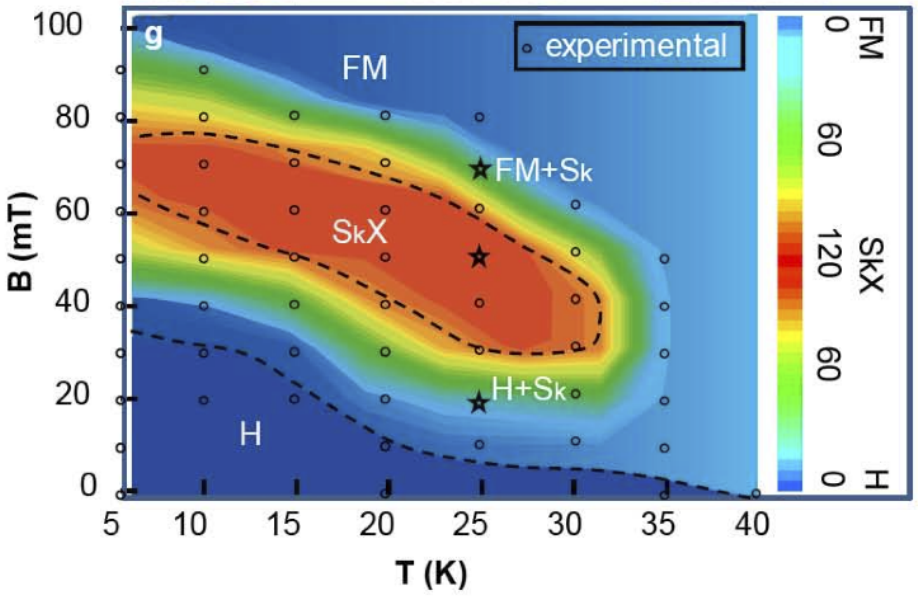

Figure 1.8: Phase diagram of $Fe_{0.5}Co_{0.5}Si$.

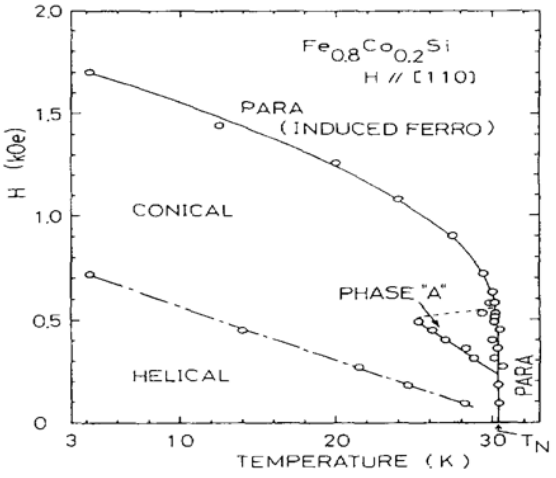

Figure 1.9: Phase diagram of $Fe_{0.8}Co_{0.2}Si$.

creases until it vanishes at $p = p_c \approx 14.6$kbar. [26, 28] The transition is second order or very weakly first order above a temperature of approximately 10 K, and strongly first order at lower temperatures, with a tricritical point separating the two regimes. These features have been explained as universal properties of quantum ferromagnets in an approximation that neglects the helical order at longer length scales. [29] The phase diagram in the T-p plane is shown in Fig. 1.11. If a magnetic field is applied in the vicinity of p_c, tricritical wings, i.e., surfaces of first-order transitions, emerge from the tricritical point that are believed to end in a pair of quantum critical points in the $T = 0$ plane. [23] This feature, which is depicted in Fig. 1.10, has been explained theoretically in Refs. [29, 30].

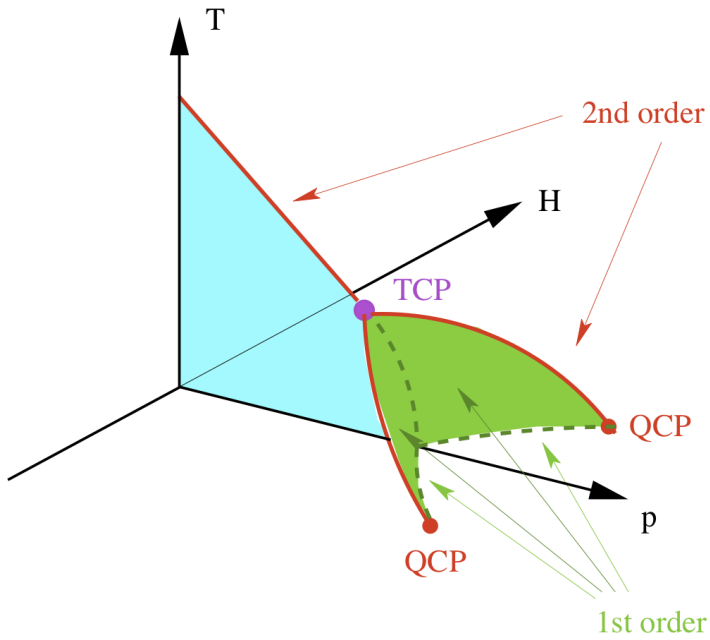

Figure 1.10: Schematic phase diagram of MnSi in the space spanned by T, p, and H showing the tricritical wings and quantum critical points (QCP).

There are also reports on an intermediate phase slightly above the transition

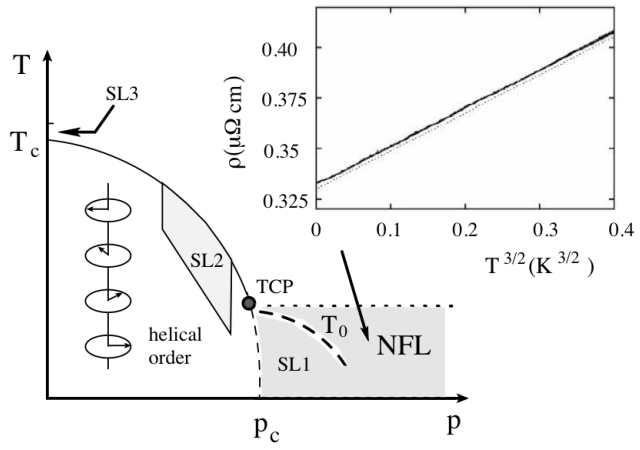

Figure 1.11: Schematic phase diagram of MnSi in the T-p plane. The tricritical point (TCP) separates a line of second order transitions (solid line) from a line of first-order transitions (dashed line). The inset shows the resistivity data from Ref. [23] in the non-Fermi-liquid (NFL) region. The boundary of the NFL region (dotted line) is not sharp. SL1, SL2, and SL3 refer to the possible spin-liquid phases or regions reported.

temperature at zero magnetic field, making the transition first order. This intermediate phase is chiral. This may be a spin liquid phase or Skyrmion liquid phase, or may be similar to blue phases of liquid crystal. [31, 32]

The columnar phase in MnSi and FeGe is also interesting. Unlike previous neutron diffraction experiments such as Fig. 1.1, Mühlbauer *et. al.* put the neutron beam to be parallel to the applied magnetic field, and found that the columnar phase exhibits sixfold symmetry, as shown in Fig. 1.12. [33] This configuration is a two-dimensional (2D) hexagonal periodic columnar structure on a plane which is perpendicular to the applied magnetic field, as shown in Fig. 1.14. [33] A similar six-fold pattern appears in $Fe_{0.8}Co_{0.2}Si$, as shown in Fig. 1.13. [34] This structure resembles a vortex lattice in type-II superconductors, [35] rotating Bose-Einstein

condensate (BEC), [36] the helical nanofilaments (HN) of smectic liquid crystals, [37, 38] and blue phase III (BP III) in cholesteric liquid crystals. [39] Later, a real-space observation using Lorentz TEM on the SkX phase of $Fe_{0.5}Co_{0.5}Si$ reveals the same hexagonal structure, as shown in Fig. 1.15. [8] And the same structure occurs near the room temperatures in FeGe, as shown in Fig. 1.16. [40] These individual magnetic vortices are believed to be Skyrmions. It was demonstrated through calculating its Skyrmion density, as shown in Fig. 1.17. [33] Its chirality nature suggests that DM interaction plays a role in stabilizing the lattice, making some physicists believe that this phase exists in helimagnets in general. The lattice of columns is a more stable ordered state of helimagnets.

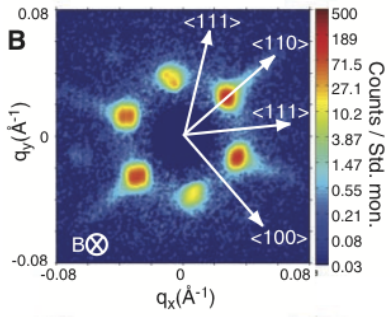

Figure 1.12: Neutron scattering data in the columnar phase of MnSi. The applied magnetic field is perpendicular to the paper. The six-fold pattern implies the two-dimensional hexagonal columnar structure.

1.4 Fluctuations and Goldstone modes

Even in the disordered phase of helimagnets, it was found that the fluctuations have a chiral nature. [41] Moreover, a number of phases of helimagnets break the

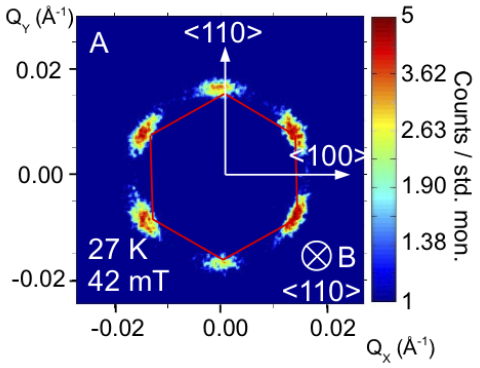

Figure 1.13: Neutron scattering data in the columnar phase of $Fe_{0.8}Co_{0.2}Si$. The applied magnetic field is perpendicular to the paper.

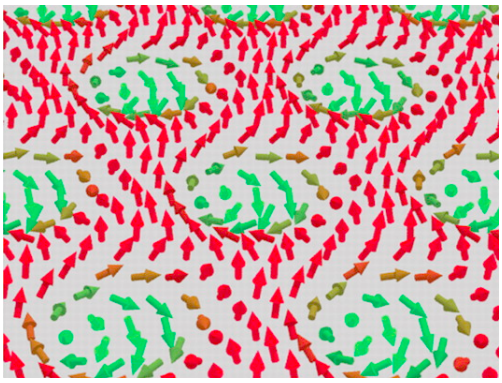

Figure 1.14: A hexagonal lattice of Skyrmions in the columnar phase of MnSi.

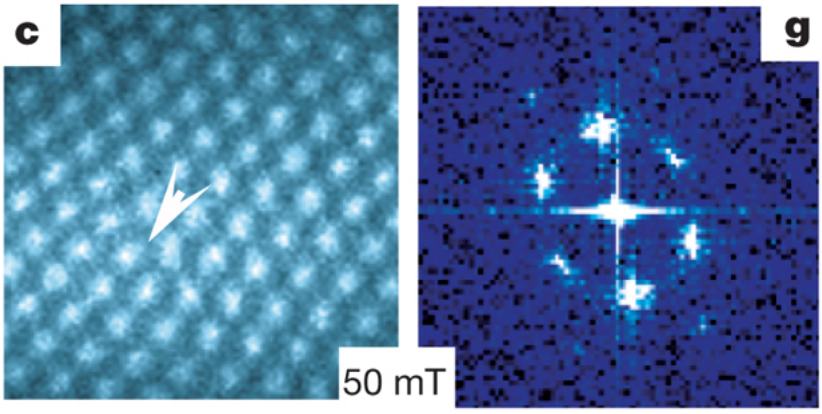

Figure 1.15: Lorentz TEM image of $Fe_{0.5}Co_{0.5}Si$ in the SkX phase at $T = 25$ K and $H = 50$ mT. (left) The corresponding FFT image is plotted. (right)

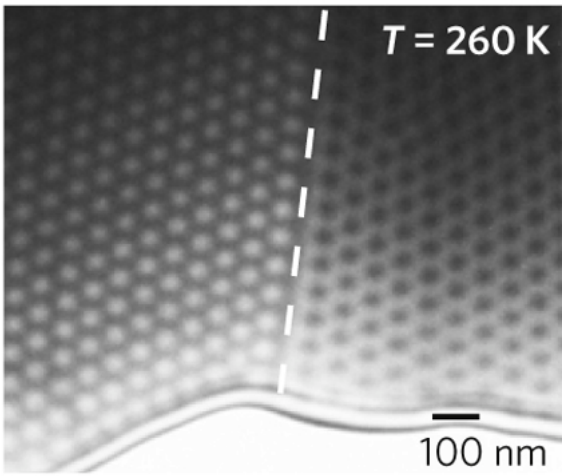

Figure 1.16: Lorentz TEM image of FeGe in the SkX phase at $T = 260$ K and $H = 0.1$ T.

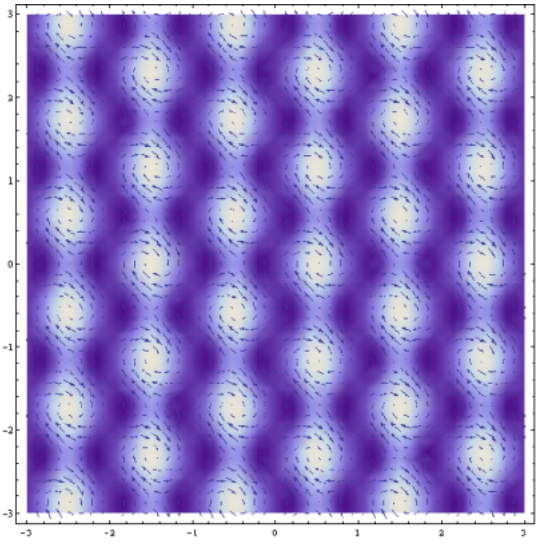

Figure 1.17: Spin configuration of the columnar phase in MnSi projected onto the x-y plane. The color denotes the Skyrmion density at different regions.

translational symmetry spontaneously. By Goldstone theorem, there are massless (or soft) modes associated with them. [42] Helimagnets have the same helical order as the cholestoric liquid crystal. Therefore they should have the same dispersion relation of the fluctuations given by [43, 24, 44]

$$\Omega \sim k_z^2 + c_\perp \mathbf{k}_\perp^4, \tag{1.1}$$

where $\mathbf{k}_\perp = (k_x, k_y)$. This is softer than ferromagnetic magnons (with spectrum k^2 [2]) because of the invariance of the helimagnet under the rotations of $\mathbf{q}$. The dispersion is anisotropic. These softer Goldstone modes make the helimagnet unstable due to Mermin-Wagner theorem, [45, 46] as a pure helimagnet is similar to a 2D ferromagnet, as shown in Fig. 1.2. [4] Therefore, the fluctuations of a helimagnet are more significant than those of a ferromagnet, causing measurable consequences.

External magnetic field and additional crystal-field effects, such as pinning, remove some of the symmetries of the system. However, they do not give the helimagnon a mass, but make them less soft. [48] (See Chapter 4.)

On the other hand, the columnar phase breaks the continuous translational symmetry on the lattice planes. Like the blue phase III in cholestoric liquid crystal, this phase has two Goldstone modes. [24] They are phonons of the compression and shear modes. Without magnetic field, the system is invariant under the rotation of

[4] A more rigorous way to see it is from its Goldstone mode in Eq. (1.1), as $\int d^3\mathbf{x} e^{i\mathbf{k}\cdot\mathbf{x}} \left(k_z^2 + \frac{\mathbf{k}_\perp^4}{2q^2}\right)^{-1} = \sqrt{2}\pi q \int d^2\mathbf{k}_\perp \frac{1}{\mathbf{k}_\perp^2} e^{i\mathbf{k}_\perp\cdot\mathbf{x}_\perp} e^{-\frac{\mathbf{k}_\perp^2}{\sqrt{2}q}z}$, which is essentially equivalent to the Goldstone modes in $d = 2$, which leads to logarithmic divergence, according to Mermin-Wagner theorem. [47, 46, 45]

the 2D lattice plane. This gives the Goldstone modes a dispersion relation [49, 24, 50]

$$\Omega \approx \mathbf{k}_{\perp}^2 + c_z k_z^4. \tag{1.2}$$

The 2D lattice forms columns of Skyrmions, and the column fluctuates about their equilibrium positions, [50] as shown in Fig. 1.18. An external magnetic field makes this mode less soft. [48] (See Chapter 4.)

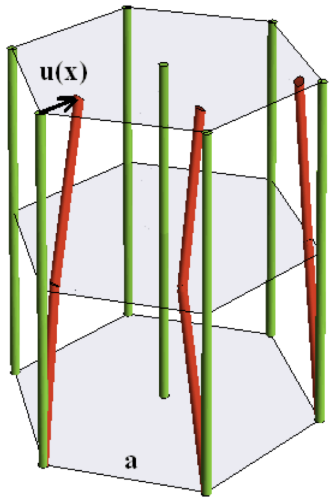

Figure 1.18: Fluctuations of columns in the A phase of MnSi.

These Goldstone modes indicate the fluctuations are huge, as seen in Eqs. (1.1) and (1.2). Due to these Goldstone modes, helimagnets exhibit transport properties different from Fermi liquids. [51] For example, it was found that in MnSi at pressure above 14.6 kbar, the resistivity has the temperature dependence of the form $\rho(T) = \rho_0 + AT^{\frac{3}{2}}$, as shown in Fig. 1.19, [23, 52] contrary to the result from Fermi liquid theory $\rho(T) = \rho_0 + AT^2$. [53] The existence of a two-dimensional lattice of Skyrmions shed lights to the explanation of this anomaly because of its anisotropic Goldstone modes. [50] Besides resistivity, other physical observables such as thermal

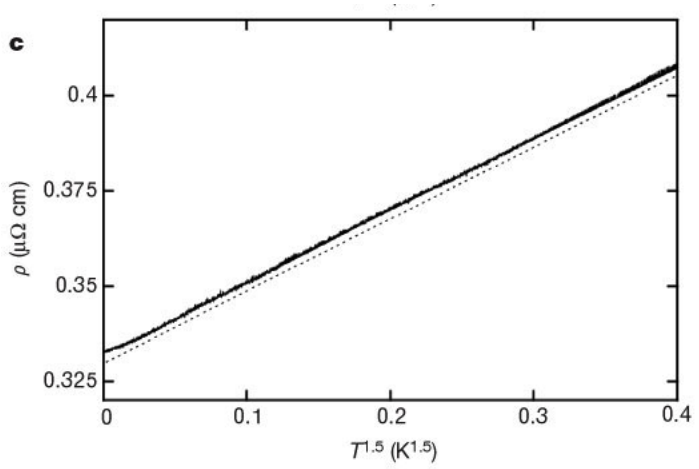

Figure 1.19: Experimental results of the resistivity of the disordered phase of MnSi at the pressure $p \approx 14.8$ kbar.

conductivity and specific heat are also different from those of a Fermi liquid.

The explanation of this unusual transport properties lies in the Goldstone modes, which couples to the conducting electrons, just like the electron-phonon interactions. The anisotropic dispersion relations of the Goldstone modes lead to non-analytic corrections to Fermi-liquid behaviors. [51] The effect of crystal fields and the presence of quenched disorder should also play a role. To see the coupling between helimagnons and the conduction electrons, one need microscopic model for helimagnets with fermionic degrees of freedom. The scattering matrix can be derived, which is used to calculate the single-particle relaxation rate and the electron-electron scattering rate. With this model, we can make predictions of the temperature dependence of these transport properties in various ordered phases of helimagnets in addition to the NFL phase. (See Chapter 5.)

1.5 Skyrmions in helimagnets

Skyrmions are excitations to the system. The Goldstone modes are also important in the long-range behavior of Skyrmions.

Skyrmions are non-trivial two-dimensional topological objects in various field theories. They were first used to model baryons in nuclear physics. [54] More recently, they have been discussed in quantum Hall ferromagnets, [55, 56] nematic liquid crystals, [57] p-wave superconductors, [58, 59] spinor BEC [60, 61] and topological insulators. [62] Now the Skyrmion lattice is also a candidate for the columnar phase in various helimagnets, with each column being one Skyrmion. Prior to this, a lattice of Skyrmions was predicted in systems with DM interactions. [63, 64, 65] On the other hand, a Skyrmion lattice may melt into a liquid of isolated Skyrmions. [56] Because of its topological nature, a Skyrmion cannot be created or annihilated through continuous deformation of the magnetic structure. An electron passing through a Skyrmion has its spin rotated once, as shown in Fig. 1.20. [66] (See Chapter 6.)

The topology of a Skyrmion is characterized by the winding number. Assume that the magnetization is given by

$$\mathbf{M}(\mathbf{x}) = m(\mathbf{x})\mathbf{n}(\mathbf{x}), \tag{1.3}$$

where $m(\mathbf{x})$ and $\mathbf{n}(\mathbf{x})$ denotes the magnitude and direction of $\mathbf{M}$. Then the winding number is defined as [67]

$$W = \int dx \int dy \frac{1}{4\pi} \mathbf{n} \cdot \left(\frac{\partial \mathbf{n}}{\partial x} \times \frac{\partial \mathbf{n}}{\partial y} \right). \tag{1.4}$$

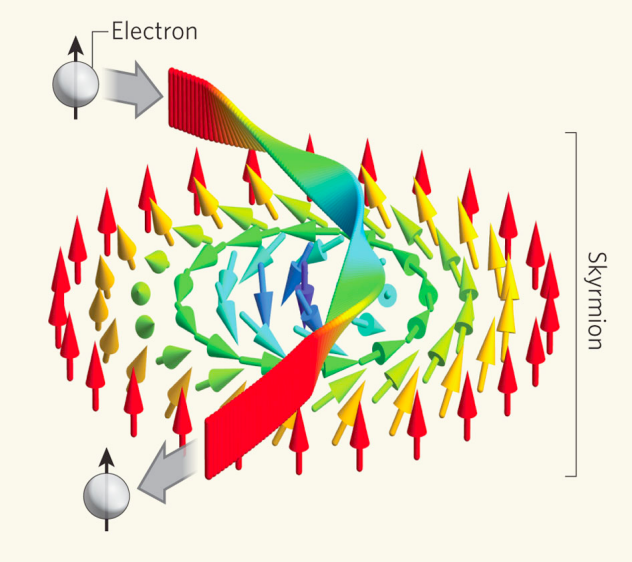

Figure 1.20: When an electron moves through a Skyrmion, its spin twists to adjust to the Skyrmionic configuration. (adapted from Ref. [66])

Upon continuous deformation of the configurations, the winding number W remains unchanged. The Skyrmion in Fig. 1.20 has $W = -1$.

1.5.1 Skyrmion lattice

The columnar phase was discovered and believed to be a Skyrmion lattice. In Ref. [33], the lattice is described as the superposition of three helimagnets perpendicular to the magnetic field, stabilized by the fluctuations, as in Eq. (3.13), [33] with six dominant Fourier modes as in the neutron scattering data in Figs. 1.12 and 1.13. This provides a good picture of the "vortex" lattice structure, but its periodic description does not convey the localized nature of each Skyrmion, which should have more Fourier modes. And this description fixes the core-to-core distance to the order of q^{-1}, which is not necessarily true since there exist other system

length scales. (See Chapter 2) The Abrikosov form of Skyrmion lattice [68] should be explored with more details to understand more about the details of the lattice structure. (See Chapters 3 and 7.)

1.5.2 Isolated Skyrmions

If the lattice of Skyrmions melts into a liquid of Skyrmion, the liquid is so dilute that the Skyrmions do not interact with one another. There are also previous studies suggesting that an isolated Skyrmion has a size of order q^{-1}. [63, 64, 65] However, there should be competitions of various length scales that contribute to the size of a Skyrmions.

Moreover, the definition of the size of a Skyrmion is ambiguous, because a Skyrmion affects the magnetic ordering globally. In the Skyrmion lattice, the size of Skrymion can be thought of as the core-to-core distance. But for an isolated Skyrmion, there is no core-to-core distance. We can define the size from the tail behavior, which is of the order of the correlation length ξ if the correlation function goes like $e^{-\frac{r}{\xi}}$. But when it is in an ordered phase such as conical phase or columnar phase, the correlation function is algebraic in distance such that we cannot read off correlation length. The size of the Skyrmion can also be estimated with its core solution as R, with a variable $f(\rho) \sim 1 - \frac{\rho}{R}$, where ρ is the radial distance from the core. [69] But this leads to size often given by q^{-1} as DM interaction is the first dominant interaction near the core. We need a better definition of the Skyrmion size. (See Chapter 7)

1.6 Outline of the thesis

In this thesis, we will discuss various aspects of the helimagnets. In Chapter 2, we will consider a model appropriate for the helimagents. We will explore the hierarchy of energy scales in the order of the spin-orbit coupling $g_{\rm so}$. We will list the physical length scales in the helimagnetic systems.

In Chapter 3, we will discuss, using mean-field theory, the ordered phases, including the pinned helical phase, elliptic conical phase, aligned conical phase and the A phase.

In Chapter 4, we will discuss the Goldstone modes of the ordered phases. We will give the expressions for the Goldstone modes, and give arguments why they have the forms as they are given.

In Chapter 5, we will give the temperature dependence of various transport properties for different ordered phases. We will derive it from the microscopic model of helimagnets by considering the electronic degrees of freedom and their fluctuations.

In Chapter 6, we will review the basics of Skyrmions. In Chapter 7, we will define the size of a Skyrmion in four ways, and evaluate it for each definition. We will discuss the role of spontaneous symmetry breaking on the magnetic ordering of Skyrmions.

In Chapter 8, we will end this thesis with a conclusion.

Chapter 2

Model for Helimagnets

In this chapter, we introduce the field-theoretical model that is appropriate for helimagnets. We explore the meaning and symmetry involved of various terms in the action. We also relate these terms to a hierarchy of energy scale in terms of the order of spin-orbit coupling, characterized by a small dimensionless constant $g_{\rm so}$. And we give the expression of various physical length scales in terms of the model.

2.1 Landau-Ginzburg-Wilson (LGW) functional

We consider a Landau-Ginzburg-Wilson (LGW) functional for a three-dimensional order parameter (OP) field $\mathbf{M} = M_x\hat{\mathbf{x}} + M_y\hat{\mathbf{y}} + M_z\hat{\mathbf{z}}$ whose expectation value is proportional to the magnetization. We will consider an action that is appropriate for MnSi and FeGe, which crystallize in the cubic B20 structure with space group $P2_13$, as shown in Fig. 2.1. We will organize the action according to the dependence of its various constituents on powers of the spin-orbit interaction $g_{\rm so}$. Within this scheme, we write

$$\mathcal{S}[\mathbf{M}] = \mathcal{S}_{\rm H}[\mathbf{M}] + \mathcal{S}_{\rm H'}[\mathbf{M}] + \mathcal{S}_{\rm DM}[\mathbf{M}] + \mathcal{S}_{\rm cf}[\mathbf{M}], \tag{2.1}$$

2.1.1 Classical Heisenberg model

The first two terms in Eq. (2.1)

$$\mathcal{S}_{\mathrm{H}}[\mathbf{M}] = \int_V d^3x \left[\frac{r}{2}\mathbf{M}^2(\mathbf{x}) + \frac{a}{2}\left(\nabla\mathbf{M}(\mathbf{x})\right)^2 + \frac{u}{4}\left(\mathbf{M}^2(\mathbf{x})\right)^2 - \mathbf{H}\cdot\mathbf{M}(\mathbf{x})\right] \quad (2.2a)$$

$$\mathcal{S}_{\mathrm{H}'}[\mathbf{M}] = \int_V d^3x \left[\frac{d}{2}\left(\nabla\cdot\mathbf{M}(\mathbf{x})\right)^2 + \frac{w}{4}\left(\nabla\mathbf{M}^2(\mathbf{x})\right)^2\right], \quad (2.2b)$$

are the terms the action for an isotropic classical Heisenberg ferromagnet in a homogeneous external magnetic field $\mathbf{H}$. $\int_V d^3x$ denotes a real-space integral over the system volume. $(\nabla\mathbf{M})^2$ stands for $\sum_{i,j=1}^{3} \partial_i M_j \partial^i M^j$, with $\partial_i \equiv \partial/\partial x_i$ the components of the gradient operator $\nabla \equiv (\partial_x, \partial_y, \partial_z)$. r, a, d, u, and w are the parameters of the Landau theory; they are of zeroth order in the spin-orbit coupling g_{so}. Eqs. (2.2) contain all analytic terms invariant under co-rotations of real space and OP space up to quartic order in $\mathbf{M}$ and bi-quadratic order in $\mathbf{M}$ and ∇. $\mathcal{S}_{\mathrm{H}}$ in Eq. (2.2a) contains the usual LGW term for ferromagnets, including the Zeeman term.

In $\mathcal{S}_{\mathrm{H}'}$ in Eq. (2.2b), there is one higher-order term, with coupling constant w, as an example of a class of terms that can stabilize unusual phases in helimagnets, although they are not of qualitative importance in ferromagnets. [1] [2]

[1] $\nabla\cdot(\mathbf{M}\times(\nabla\times\mathbf{M})) = (\nabla\times\mathbf{M})^2 - \mathbf{M}\cdot\nabla(\nabla\cdot\mathbf{M}) + \mathbf{M}\cdot\nabla^2\mathbf{M}$. [70]

[2] The term $(\nabla\cdot\mathbf{M})^2$ in $\mathcal{S}_{\mathrm{H}'}$ or equivalently (if combined with the $(\nabla\mathbf{M})^2$ term), $(\nabla\times\mathbf{M})^2$, is not usually considered in the theory of classical Heisenberg ferromagnets. This term, as well as a stronger one, $|\mathbf{k}\cdot\mathbf{M}(\mathbf{k})|^2/\mathbf{k}^2$ in Fourier space, results from the classical dipole-dipole interaction, which in turn results from the coupling of the order-parameter field to the electromagnetic vector potential, see Ref. [11]. These terms have small coefficients due to the relativistic nature of the dipole-dipole interaction, and therefore are usually neglected in the discussion of isotropic ferromagnets, despite the fact that they are renormalization-group relevant with respect to the

2.1.2 Dzyaloshinskii-Moriya (DM) interaction

The second term

$$\mathcal{S}_{\rm DM} = \frac{c}{2}\int_V d\mathbf{x}\ \mathbf{M}(\mathbf{x})\cdot(\nabla\times\mathbf{M}(\mathbf{x})), \tag{2.3a}$$

is the DM interaction term that favors a nonvanishing curl of the magnetization. The existence of this term hinges on the spin-orbit coupling, [3] [10, 11] as well as on the system not being invariant with respect to spatial inversion (due to the linear dependence on the gradient operator). An example of such system includes MnSi, a B20 cubic crystal with space group $P2_13$ as shown in Fig. 2.1. [72] This crystal structure is said to be noncentrosymmetric, i.e., lack of a spatial inversion center. [72] The coupling constant c is linear in $g_{\rm so}$, and on dimensional grounds we have

$$c = ak_{\rm F}g_{\rm so}, \tag{2.3b}$$

with $k_{\rm F}$ the Fermi wave number which serves as the microscopic inverse length scale. This can be considered the definition of $g_{\rm so}$. For MnSi, $g_{\rm so}\approx 0.05$. For all helimagnets listed in Table 1.1, $g_{\rm so}\ll 1$.

critical Heisenberg fixed point.[71] In the context of helimagnets, where many effects of qualitative interest are small due to the smallness of $g_{\rm so}$, it is less obvious whether these terms can be ignored. However, for the field configurations we will consider they are not qualitatively different from the $(\nabla\mathbf{M})^2$ term, and we will neglect them. The effect of dipole-dipole interaction on helimagnets will not be discussed in this thesis.

[3] The DM interaction can be derived by considering a Hamiltonian of free electrons and a term with spin-orbit coupling. By second-order perturbation, one can get the interaction energy in Eq. (2.3a). [10]

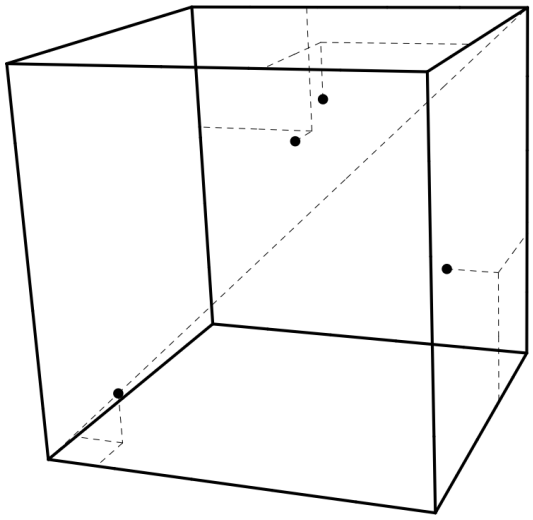

Figure 2.1: Crystal structure of MnSi and FeGe (tedrahedral $P2_13$). There are four metal atoms in the positions (x, x, x), $(x+\frac{1}{2}, \frac{1}{2}-x, -x)$, $(-x, x+\frac{1}{2}, \frac{1}{2}-x)$ and $(\frac{1}{2}-x, -x, x+\frac{1}{2})$. For MnSi, $x_{\rm Mn} = 0.137$ and $x_{\rm Si} = 0.835$.

2.1.3 Crystal-field effects

The preceding contributions to the action are all invariant under either separate rotations, or co-rotations, in spin (or magnetization) space and real space. The spin-orbit interaction couples the electron spin, and hence the magnetization, to the underlying lattice. Therefore, in addition to the rotationally invariant terms, any term that is invariant under elements of the space group connected with the crystal lattice is allowed. For the B20 structure of MnSi and FeGe, the appropriate space group is $P2_13$, [73] as in Fig. 2.1. To quartic order in $\mathbf{M}$, and bi-quadratic order in ∇ and $\mathbf{M}$, the allowed terms in the action are the crystal-field terms

$$\mathcal{S}_{\rm cf} = \int_V d\mathbf{x} \, \sum_{i=1}^{3} \left[\frac{b}{2} (\partial_i \, M_i(\mathbf{x}))^2 + \frac{b_1}{2} (\partial_i \, M_{i+1}(\mathbf{x}))^2 + \frac{v}{4} \, M_i^4(\mathbf{x}) \right], \tag{2.4a}$$

where $M_4 \equiv M_1$. The last term is the usual cubic anisotropy that is always present in a magnet on a cubic lattice, and

$$v = u' g_{\rm so}^4 \tag{2.4b}$$

with $|u'| \approx u$. Of the gradient-squared terms, the first term, the pinning term, also has cubic symmetry; the second one does not, but is invariant under elements of $P2_13$, which contains screw axes along the cubic directions that involves a two-fold rotations and half-lattice translation, and three-fold rotation axes along the $\langle 111 \rangle$ direction. [72] On dimensional grounds, we have

$$\begin{aligned} b &= a' g_{\rm so}^2, \\ b_1 &= a_1' \, g_{\rm so}^2, \end{aligned} \tag{2.4c}$$

with $|a'| \approx |a_1'| \approx a$.

The model including the terms with coefficients r, a, c, u and H in CP^1 representation (for studying Skyrmion lattice) and its saddle-point equations are detailed in Appendix B.

2.2 Energy scales

The various contributions to the action $\mathcal{S}$, and their dependencies on $g_{\rm so}$, imply a hierarchy of energy scales.

2.2.1 $O(g_{\rm so}^0)$

At zeroth order in $g_{\rm so}$, we have the microscopic scale, which is represented by the Fermi energy $\epsilon_{\rm F}$ and the Fermi wave number $k_{\rm F}$. Fluctuations renormalize this to the critical scale, which is represented by the magnetic ordering temperature $T_{\rm c}$ and the corresponding length scale. The physics at these scales is described by $\mathcal{S}_{\rm H}$, Eq. (2.2a). This affects the magnitude of the magnetic ordering for different ordered phases.

2.2.2 $O(g_{\rm so}^2)$

The chiral DM term is balanced by the rotationally invariant gradient squared term in Eq. (2.1) that makes magnetization gradients energetically costly. As a result, the relevant gradient or momentum scale is of $O(g_{\rm so})$, and hence the chiral wave number scale is given by the microscopic scale times $g_{\rm so}$. $\mathcal{S}_{\rm DM}$ contains one explicit factor of $g_{\rm so}$ and one gradient, and hence its contribution to the free energy is of $O(g_{\rm so}^2)$. The physics at this scale is described by $\mathcal{S}_{\rm DM}$ in Eq. (2.3a) in conjunction with $\mathcal{S}_{\rm H}$. The helical and conical phases are related to this scale through its helical period. The smallness of $g_{\rm so}$ gives a long helical wavelength.

2.2.3 $O(g_{\rm so}^4)$

At fourth order in $g_{\rm so}$, crystal-field effects come into play. They pin the helix, are small compared to the chiral energy scale by another factor of $g_{\rm so}^2$, and are described by $\mathcal{S}_{\rm cf}$, Eq. (2.4a). Since gradients are effectively of $O(g_{\rm so})$, the contributions

of all three terms in $\mathcal{S}_{\rm cf}$ to the free energy are of $O(g_{\rm so}^4)$. Crystal-field effects are generally very small due to the smallness of $g_{\rm so}$.

2.3 Physical length scales

There are a few physical length scales associated with the energy scales in Section 2.2 in various phases. Some of these length scales are related to the phases with details found in Chapter 3. The Goldstone modes will be expressed in these lengths in Chapter 4, and the sizes of Skyrmions in Chapter 7.

2.3.1 Pitch Wavenumber

The pitch wavenumber of the helix given by

$$q = \frac{c}{2a}. \tag{2.5}$$

It is proportional to the strength of DM interaction, and therefore $g_{\rm so}$. The helical period is $\frac{2\pi}{q}$, which is typically 100 times larger than the lattice constant, as shown in Table 1.1. Therefore, q is 100 times smaller than the Fermi wavenumber.

2.3.2 Thermal Correlation Lengths

There is a range for the correlations in fluctuations for each of the phases. The range is called the correlation length. This correlation length diverges when the relevant phase boundary or transition point is reached. [71]

The paramagnet is stable or metastable only for $r > 0$. The corresponding correlation length is given by ξ_p, which diverges when r approaches 0. In LGW

model, it is [71]

$$\xi_p = \sqrt{\frac{a}{r}}, \tag{2.6}$$

in both longitudinal and transverse directions.

The ferromagnet is stable or metastable only for $r < 0$. The longitudinal correlation length of the ferromagnet is given by

$$\xi_f = \sqrt{\frac{a}{2|r|}}, \tag{2.7}$$

which diverges for $r \to 0$. The transverse correlation length is infinite when there is no external magnetic field, i.e., $H = 0$. But it becomes finite when the field is present. It is defined by the magnetic length $\bar{l}_H$ in Eq. (2.11) and expressed approximately in Eq. (2.12c) for $r < 0$.

There are correlation lengths associated with the helimagnetic phases as well. Without magnetic field, the correlation length approaching the helimagnetic-paramagnetic phase transition from the paramagnetic phase ($r > aq^2$) is given by

$$\xi_h = \sqrt{\frac{a}{r - aq^2}} = \left(\frac{1}{\xi_p^2} - q^2\right)^{-\frac{1}{2}}. \tag{2.8}$$

If the phase transition is approaching from the helimagnetic phase ($r < aq^2$), it is given by

$$\xi_h' = \sqrt{\frac{a}{aq^2 - r}} = \left(q^2 - \frac{1}{\xi_p^2}\right)^{-\frac{1}{2}}. \tag{2.9}$$

Note that at the transition point between the helimagnet and paramagnet at $H = 0$,

$$q\xi_p = 1. \tag{2.10}$$

2.3.3 Magnetic Length

We define a magnetic length for the paramagnet and the ferromagnet without the DM interaction: [74]

$$\bar{l}_H = \sqrt{\frac{am}{H}}. \tag{2.11}$$

It is basically the thermal and magnetic field dependent transverse correlation length.

For paramagnet ($r > 0$), if $r \gg u^{\frac{1}{3}} H^{\frac{2}{3}}$, it is

$$\bar{l}_H \approx \xi_p. \tag{2.12a}$$

But for $r \ll u^{\frac{1}{3}} H^{\frac{2}{3}}$, $m \approx (u^{-1} H)^{\frac{1}{3}}$. Hence the length becomes

$$\bar{l}_H \approx \frac{a^{\frac{1}{2}}}{u^{\frac{1}{6}} H^{\frac{1}{3}}}, \tag{2.12b}$$

which is related to the mean-field critical exponent $\delta = 3$. [71]

For ferromagnet ($r < 0$), it is infinite for zero magnetic field. However, in the magnetic field, it is

$$\bar{l}_H \approx \frac{|r|^{\frac{1}{4}} a^{\frac{1}{2}}}{u^{\frac{1}{4}} H^{\frac{1}{2}}}. \tag{2.12c}$$

We expect this because the transverse fluctuations of ferromagnet have the spectrum schematically in the form $\omega(\mathbf{k}) = k^2 + H$, as in Eq. (4.3).

2.4 Conclusion

To summarize, we have introduced an LGW functional appropriate for a helimagnet. The functional contains a term of classical Heisenberg ferromagnet, a

DM interaction term that is induced by spin-orbit coupling, and the crystal-field terms. The DM interaction is responsible for stabilizing the helimagnet over the ferromagnet. The smallness of spin-orbit coupling gives a helical period larger than the lattice constant.

We then introduced the hierarchy of energy scales in ascending order of the spin-orbit coupling $g_{\rm so}$, and the terms in the action associated with each scale. In the end, we introduced various physical length scaled associated with the model.

Chapter 3

Ordered Phases of Helimagnets

In this chapter, we derive the mean-field phase diagram for systems described by the action given by Eq. (2.1). [48] We will use the hierarchy of energy scales, listed in the order of $g_{\rm so}$ in Section 2.2 to show how a more sophisticated phase diagram emerges as one keeps effects of higher order in $g_{\rm so}$.

To do so, we consider field configurations of the following form:

$$\mathbf{M}(\mathbf{x}) = m_{sp}^{+}\hat{\mathbf{e}}_{+}\cos(\mathbf{q}\cdot\mathbf{x}) + m_{sp}^{-}\hat{\mathbf{e}}_{-}\sin(\mathbf{q}\cdot\mathbf{x}) + \mathbf{m}_{||}. \tag{3.1a}$$

Here $\mathbf{m}_{||}$ is a homogeneous component of the magnetization, $m_{sp}^{\pm}$ are amplitudes of Fourier components with wave vector $\mathbf{q}$, and $\hat{\mathbf{e}}_{\pm}$ are two unit vectors that form a right-handed *dreibein* together with $\mathbf{q}$:

$$\hat{\mathbf{e}}_{+}\times\hat{\mathbf{e}}_{-} = \hat{\mathbf{q}}, \tag{3.1b}$$

$$\hat{\mathbf{q}}\times\hat{\mathbf{e}}_{+} = \hat{\mathbf{e}}_{-}, \tag{3.1c}$$

$$\hat{\mathbf{e}}_{-}\times\hat{\mathbf{q}} = \hat{\mathbf{e}}_{+} \tag{3.1d}$$

where $\hat{\mathbf{q}} = \frac{\mathbf{q}}{q}$. The sinusoidal terms in Eq. (3.1a) describe a helix with pitch vector $\mathbf{q}$. The helix is in general elliptically polarized, and it is useful to define a polarization parameter

$$\pi = \frac{m_1^{-}}{m_1^{+}}, \tag{3.2}$$

Special cases are circular polarization, $\pi = 1$, and linear polarization, $\pi = 0$ or

$\pi = \infty$. The motivation for the *ansatz* in Eqs. (3.1) is provided by the fact that it gives the functional form of the global minimum of the action $\mathcal{S}$ in Eq. (2.1) at some temperature and magnetic fields, if one neglects the crystal-field terms $\mathcal{S}_{\rm cf}$ in Eq. (2.4a); that is, for the action up to $O(g_{\rm so}^2)$.

We discuss different phases in the mean-field theory according to the hierarchy of the energy scale in Section 2.2. The schematic phase diagram is shown in Fig. 3.1. [48]

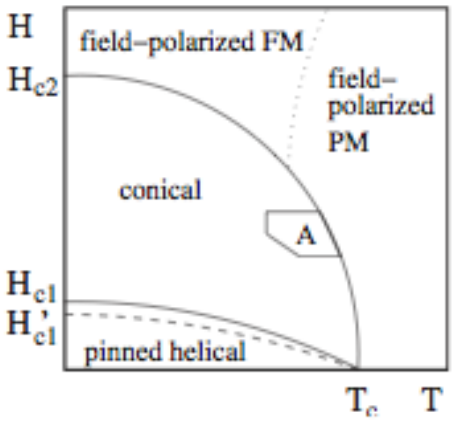

Figure 3.1: Schematic phase diagram of MnSi in the H-T plane showing the helical, conical, and A phases, as well as the field-polarized ferromagnetic (FM) and paramagnetic (PM) states.

Throughout this thesis, the z-axis is taken to the the direction of the magnetic field $\mathbf{H}$, i.e.,

$$\mathbf{H} = H\hat{\mathbf{z}}. \tag{3.3}$$

3.1 $O(g_{\rm so}^0)$: Ferromagnet

To zeroth order in $g_{\rm so}$ the system is approximated by a ferromagnet. According to the action $\mathcal{S}_{\rm H}$ in Eq. (2.2a), for $H = 0$ there is a second-order phase transition which in mean-field approximation occurs at $r = 0$. [71] Putting $m_{sp}^{\pm} = 0$ in Eq. 3.1a, the free energy density $f = \frac{\mathcal{S}}{V}$ is a function of $m_{||}$, and is

$$f(m_{||}) = \frac{r}{2} m_{||}^2 + \frac{u}{4} m_{||}^4. \tag{3.4}$$

To find the ground state,

$$\frac{df(m_{||})}{dm_{||}} = r m_{||} + u m_{||}^3 = 0. \tag{3.5}$$

It is the disordered paramagnet for $r > 0$, with zero magnetization, and the ordered ferromagnet for $r < 0$, with magnetization given by Eq. (A.3b)

$$m_{||} = M_F^{(0)} = \sqrt{\frac{|r|}{u}}, \tag{3.6}$$

so that its free energy density in mean-field approximation for $H = 0$, is

$$f_{FM} = f(m_{||} = M_F^{(0)}) = -\frac{r^2}{4u}. \tag{3.7}$$

For $H \neq 0$ there is a crossover at $r = 0$ from a paramagnetic state, where the magnetization extrapolates to zero for $H \to 0$, to a ferromagnetic state where the magnetization extrapolates to $m_{||} = \sqrt{\frac{|r|}{u}}$. Its free energy has the form

$$f(m_{||}) = \frac{r}{2} m_{||}^2 + \frac{u}{4} m_{||}^4 - H m_{||}, \tag{3.8a}$$

where $m_{||}$ is the solution of the mean-field equation of state

$$r m_{||} + u m_{||}^3 - H = 0. \tag{3.8b}$$

The solution of Eq. (3.8b) can be found in Appendix A.

This is just a classical Heisenberg model, so it cannot explain the tricritical point and the associated tricritical wings in Fig. 1.10. The latter emerge within a renormalized mean-field theory that takes into account the coupling of the magnetization to other electronic degrees of freedom.[29, 75] However, the ferromagnetic approximation suffices for understanding the gross features of the phase diagram in the T-p plane, as shown in Fig. 1.11.

3.2 $O(g_{\rm so}^2)$: Helimagnet, aligned conical phase

To second order in $g_{\rm so}$, we need to add the DM interaction term, Eq. (2.3a), to the action. This term favors a nonzero curl of the magnetization, with the direction of the curl depending on the sign of c. However, the spatial variation of $\mathbf{M}$ will be limited by the other gradient terms in the action, the $(\nabla\mathbf{M})^2$ term in particular. We thus expect a spatial modulation of $\mathbf{M}$ on a length scale on the order of $\frac{a}{c}$, or q^{-1} which is given by Eq. (2.5).

It is easy to check that the ansatz in Eq. (3.1a) solves the saddle-point equations for the action $\mathcal{S}_{\rm H} + \mathcal{S}_{\rm DM}$, with $\pi = 1$, i.e., $m_{sp}^- = m_{sp}^+ \equiv m_{sp}$, and $\hat{\mathbf{q}} = \hat{\mathbf{z}}$. The free energy density is a function of the variational parameters m_{sp}, $m_{||}$ and q, and given by

$$f(m_{sp}, m_{||}, q) = \frac{r + aq^2 - cq}{2} m_{sp}^2 + \frac{u}{4} m_{sp}^4 + \frac{r}{2} m_{||}^2 + \frac{u}{4} m_{||}^4 - H m_{||} + \frac{u}{2} m_{sp}^2 m_{||}^2. \quad (3.9)$$

To find the ground state, we take the following derivatives,

$$\left(\frac{\partial f}{\partial m_{sp}}\right)_{m_{||},q} = 0, \left(\frac{\partial f}{\partial m_{||}}\right)_{m_{sp},q} = 0, \left(\frac{\partial f}{\partial q}\right)_{m_{sp},m_{||}} = 0,$$

and we get

$$q = \frac{c}{2a}, \tag{3.10a}$$

$$m_{||} = \frac{H}{aq^2}, \tag{3.10b}$$

$$m_{sp} = m_H^2 - m_{||}^2, \tag{3.10c}$$

where

$$m_H^2 = \frac{aq^2 - r}{u}. \tag{3.10d}$$

A picture of this phase is depicted in Fig. 3.2.

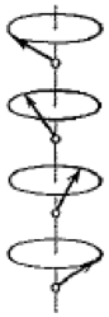

Figure 3.2: Spin orientation of an aligned conical phase. The magnetic field and the pitch vector is pointing along the vertical axis.

This solution is a minimum for $r < aq^2$ and $H < aq^2\sqrt{\frac{aq^2-r}{u}}$. With this, we have the critical field

$$H_{c2} = aq^2\sqrt{\frac{aq^2 - r}{u}}, \tag{3.11}$$

which defines the region of stability or metastability of the conical state in the phase

diagram in Fig. 3.1. [1] The aligned conical phase is actually a global minimum, as can be seen by writing the action as a sum of positive semi-definite terms that are individually minimized by this state. [33] The mean-field free energy density in that range is, by putting Eqs. (3.10) in Eq. (3.9),

$$f_{ACP} = \frac{-1}{2}\left[\frac{(aq^2 - r)^2}{2u} + \frac{H^2}{aq^2}\right]. \tag{3.12}$$

Eqs. (3.10) describe the helical phase for $H = 0$ and the conical phase for $0 < H < H_{c2}$. Comparing Eqs. (3.12) and (3.7) we see that the helical transition preempts the ferromagnetic one at $H = 0$.

For $H \to H_{c2}$ from below the helical component of the magnetization vanishes, and the free energy, Eq. (3.12), approaches that of the ferromagnet, Eqs. (3.8a). For $H > H_{c2}$, the equation of state and the free energy for the DM action $\mathcal{S}_{\rm H} + \mathcal{S}_{\rm DM}$ are the same as for a ferromagnet with action $\mathcal{S}_{\rm H}$.

These considerations account for the structure of the phase diagram shown in Fig. 3.1 except for the field H_{c1} and the columnar phase.

3.3 $O(g_{\rm so}^2)$: Helimagnet, columnar phase

3.3.1 Description of three helices perpendicular to the magnetic field

The neutron-scattering experiments by Mühlbauer *et al.* [33] showed a six-fold pattern in the Fourier space in the columnar phase, as shown in Fig. 3.3. This is consistent with the notion that the columnar phase is characterized by spin

[1] We refer to this state as the aligned conical phase, or simply conical phase, to distinguish it from the perpendicular conical phase discussed in Ref. [76].

textures that form line defects in the direction of the magnetic field, with the lines forming a hexagonal lattice, the A crystal, in the plane perpendicular to the field. This experimental observation led the authors of Ref. [33] to suggest a Skyrmion state consisting of three co-planar helices as underlying the A phase, which we will describe in details in the following paragraphs.

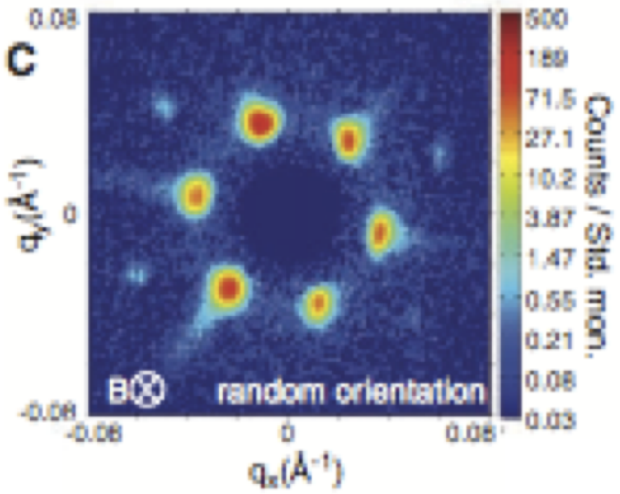

Figure 3.3: Sixfold symmetry exhibited in the neutron scattering experiment in the A phase of MnSi reported in Ref. [33].

Consider 3 helices which are perpendicular to the magnetic field (in $\hat{\mathbf{z}}$ direction). We write the ansatz

$$\mathbf{M} = m_\perp \hat{\mathbf{z}} + \sum_{i=1}^{3} m_0(\hat{\mathbf{x}}_i'' \cos(\mathbf{q}_i \cdot \mathbf{x} + \phi_i) + \hat{\mathbf{y}}_i'' \sin(\mathbf{q}_i \cdot \mathbf{x} + \phi_i)), \tag{3.13}$$

where all $\mathbf{q}_i$'s have the same magnitude q and $\sum_{i=1}^{3} \mathbf{q}_i = 0$. Define

$$\mathbf{q}_i = q\left(\cos\frac{2\pi(i-1)}{3}\hat{\mathbf{x}} + \sin\frac{2\pi(i-1)}{3}\hat{\mathbf{y}}\right), \tag{3.14}$$

for $i = 1, 2$ or 3. The unit vectors for each helix are

$$\hat{\mathbf{x}}_i'' = \sin\frac{2\pi(i-1)}{N}\hat{\mathbf{x}} - \cos\frac{2\pi(i-1)}{N}\hat{\mathbf{y}}, \tag{3.15}$$

$$\hat{\mathbf{y}}_i'' = -\hat{\mathbf{z}}, \tag{3.16}$$

for $i = 1, 2$ or 3. Then for any $i \neq j$, $\cos\frac{2\pi(i-j)}{3} = -\frac{1}{2}$. And

$$\langle\cos^2(\mathbf{q}_i\cdot\mathbf{x}+\phi_i)\cos^2(\mathbf{q}_j\cdot\mathbf{x}+\phi_j)\rangle = \frac{1}{4},$$
$$\langle\cos^2(\mathbf{q}_i\cdot\mathbf{x}+\phi_i)\sin^2(\mathbf{q}_j\cdot\mathbf{x}+\phi_j)\rangle = \frac{1}{4},$$
$$\langle\sin^2(\mathbf{q}_i\cdot\mathbf{x}+\phi_i)\sin^2(\mathbf{q}_j\cdot\mathbf{x}+\phi_j)\rangle = \frac{1}{4},$$
$$\langle\sin(\mathbf{q}_i\cdot\mathbf{x}+\phi_i)\cos(\mathbf{q}_i\cdot\mathbf{x}+\phi_i)\sin(\mathbf{q}_j\cdot\mathbf{x}+\phi_j)\cos(\mathbf{q}_j\cdot\mathbf{x}+\phi_j)\rangle = 0,$$

For the terms with three sines or cosines, the integral does not vanish only if i, j and k are all unequal. And the integral is given by

$$\langle\sin(\mathbf{q}_k\cdot\mathbf{x}+\phi_k)\cos(\mathbf{q}_i\cdot\mathbf{x}+\phi_i)\cos(\mathbf{q}_j\cdot\mathbf{x}+\phi_j)\rangle = \frac{1}{4}\sin(\phi_i+\phi_j+\phi_k),$$
$$\langle\sin(\mathbf{q}_k\cdot\mathbf{x}+\phi_k)\sin(\mathbf{q}_i\cdot\mathbf{x}+\phi_i)\sin(\mathbf{q}_j\cdot\mathbf{x}+\phi_j)\rangle = -\frac{1}{4}\sin(\phi_i+\phi_j+\phi_k).$$

The free energy density $f = \frac{\mathcal{S}_{\rm H}+\mathcal{S}_{\rm DM}}{V}$ is

$$\begin{aligned} f(m_\perp, m_0, q, \phi_1, \phi_2, \phi_3) &= \int d^3x \left\{ \left(\frac{r}{2}m_\perp^2 + \frac{u}{4}m_\perp^4 - Hm_\perp\right) \right. \\ &\quad + \left[\frac{3}{2}(r+aq^2-cq)m_0^2 + \frac{51u}{16}m_0^4\right] \\ &\quad \left. +3um_\perp^2 m_0^2 + \frac{9u}{4}m_\perp m_0^3\sin(\phi_1+\phi_2+\phi_3)\right\}. \end{aligned} \tag{3.17}$$

From Eq. (3.17), the three-helix state has the lowest free energy if the relative phases of the three helices satisfy

$$\sin(\phi_1+\phi_2+\phi_3) = -1, \tag{3.18}$$

The thermodynamic ground state is given by taking the derivatives

$$\left(\frac{\partial f}{\partial m_\perp}\right)_{m_0,q} = 0, \left(\frac{\partial f}{\partial m_0}\right)_{m_\perp,q} = 0, \left(\frac{\partial f}{\partial q}\right)_{m_0,m_\perp} = 0,$$

and for $m_0 \neq 0$,

$$r m_\perp + u m_\perp^3 + 6u m_0^2 m_\perp + \frac{9u}{4} m_0^3 \sin(\phi_1 + \phi_2 + \phi_3) - H = 0, \tag{3.19a}$$

$$\left[r + aq^2 - cq\right] + \frac{17u}{4} m_0^2 + 2u m_\perp^2 + \frac{9u}{4} m_0 m_\perp \sin(\phi_1 + \phi_2 + \phi_3) = 0, \tag{3.19b}$$

$$q = \frac{c}{2a}. \tag{3.19c}$$

Eqs. (3.19) can be solved numerically. A solution of this is plotted in Fig. 3.4. It describes a hexagonal array of line defects with the spin antiparallel to the magnetic field at the defect centers, and parallel at points on the cell boundaries, see Fig. 3.4, in qualitative agreement with the neutron scattering data.

The free energy difference between this state and the conical one has a minimum at $H \approx 0.4\, H_{c2}$, but it is still positive even at the minimum. However, Ref. [33] found that taking into account Gaussian fluctuations stabilizes the state with respect to the conical one. It should be noted that Eq. (3.13) is not a solution of the saddle-point equations for the action given by Eqs. (2.2) and (2.3a), and therefore cannot be a true local minimum of the free energy. [2] Also, the relation between this *ansatz* and what are commonly called Skyrmionic spin configurations, which *are* solutions of the saddle-point equations, [77, 68, 74] is not clear.

[2] While Eq. (3.13) is not a saddle point of the action, a true saddle point has been constructed numerically by perturbatively adding Fourier components in Ref. [33]. The quantitative difference between the true saddle point and Eq. (3.13) was found to be small.

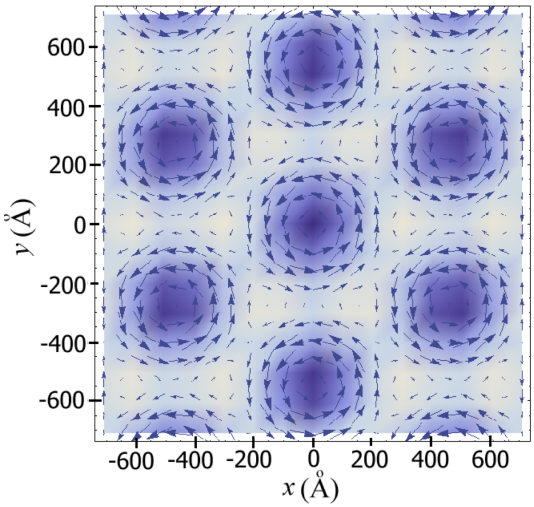

Figure 3.4: Spin configuration as given by the solution of Eq. (3.19) with the **q** vectors in the x-y plane, $q = 0.0133$, $m_\perp = 0.0146$, and $m_0 = 0.0323$. The arrows represent projections of the spins into the plane. The dark and light regions denote spin directions antiparallel and parallel to $\hat{z}$ (out of paper), respectively.

Earlier, Grigoriev *et. al.*[76] had proposed a single-helix state with the pitch vector oriented perpendicular to the external field. Although current experimental evidence favors a Skyrmion state as a candidate for the columnar phase, it is still of interest to discuss such a perpendicular conical state (PCS), since it might be a viable candidate for the ground state in some other part of the phase diagram of helimagnets. Such perpendicular helix is possible if the longitudinal magnetic susceptibility is larger than the transverse magnetic susceptibility. Similar helix can be found in cholestoric liquid crystals. [78, 24]

3.3.2 Abrikosov lattice

The description of the columnar phase in Eq. (3.13) is not an exact solution of the saddle-point equation of the model. However, an exact solution of the model as a Skyrmion lattice can be derived from the model. Numerical work on the exact decription of a Skyrmion lattice was derived. [64] On the other hand, it can be described as an Abrikosov lattice, as in vortex lattices in type-II superconductors [35] and rotating Bose-Einstein condensates (BEC). [36] It is convenient to use CP^1 representation because Skyrmions are like vortices in the representation (see Section 6.2). The details of this representation can be found in Appendix B, where we consider the model given by Eqs. (2.2) and (2.3a) only. The saddle-point equations in this representation are Eq. (B.6a) and Eq. (B.6b).

In Eq. (B.6b), the gauge $\mathbf{A}$ depends on $\mathbf{z}$ as in Eq. (B.4), leading to the non-linearity. To fix the gauge, set $\mathbf{A} = -hx\hat{\mathbf{y}}$. The dimension of h is that of the reciprocal of area, and it will be shown later that it is related to the area of a single Skyrmion site. Because of the periodic nature of the lattice, the term $-iqmn_\alpha\partial_\alpha z_i \to -iqm\langle n_\alpha\rangle\partial_\alpha z_i$ is ignored. This can be justified by the final solution. The term $-\frac{i}{2}qmz_i\partial_\alpha n_\alpha$ is also zero because the Skyrmions are azimuthal. Moreover, instead of keeping strictly $\mathbf{z}^\dagger\mathbf{z} = 1$, we relax the condition to $\langle\mathbf{z}^\dagger\mathbf{z}\rangle = 1$ where the average is over one lattice. Following Abrikosov, [35] one part of the solution is given by [68]

$$\mathbf{z} = \sqrt{\frac{\frac{h}{3^{\frac{1}{4}}\pi}}{1+|d_0|^2}}e^{iky}e^{-\frac{h}{2}\left(x+\frac{k}{h}\right)^2}\begin{bmatrix} 1 \\ d_0\sqrt{2h}\left(x+\frac{k}{h}\right)\end{bmatrix}, \tag{3.20a}$$

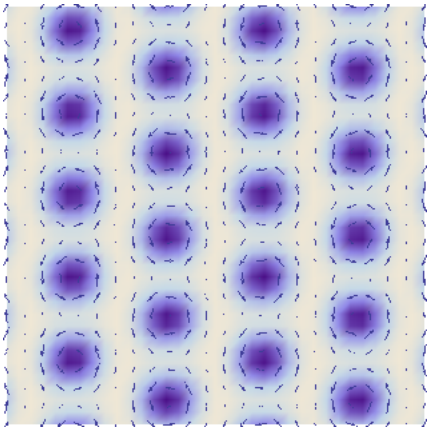

Figure 3.5: Hexagonal Skyrmion lattice described by (3.21), for $h \sim q^2$, where the vectors denote the projection of the spin on the plane, and the color denotes $n_z = z_i^* \sigma_z^{ij} z_j$ where deep blue denotes spin reversed from the magnetic field.

where the prefactor is for normalization, and

$$d_0 = -\frac{iq}{\sqrt{2h}} \frac{1}{\frac{1}{2} + \frac{H}{4ahm} + \sqrt{\frac{1}{4} + \frac{q^2}{2h} + \frac{H}{4ahm} + \left(\frac{H}{4ahm}\right)^2}}. \tag{3.20b}$$

Let l_x and l_y be the distances between cores along the x and y axes respectively, where $l_x l_y = \frac{2\pi}{h}$. Then $\mathbf{z}$ can be seen as the superposition of the above solution with different values of k where $k_j = \frac{2\pi j}{l_y}$, then

$$\mathbf{z} = \sqrt{\frac{\frac{h}{3^{\frac{1}{4}}\pi}}{1 + |d_0|^2}} \sum_{j=-\infty}^{\infty} c_j e^{i\frac{2\pi j}{l_y} y} e^{-\frac{h}{2}(x + j l_x)^2} \begin{bmatrix} 1 \\ d_0 \sqrt{2h}\,(x + j l_x) \end{bmatrix}. \tag{3.21}$$

For a triangular lattice, $c_j = c_{j+2}$. [79, 80] Choose c_j to be $\frac{1}{\sqrt{2}}$ and $\frac{i}{\sqrt{2}}$ for even and odd j's respectively. And $l_y = \frac{\sqrt{3}}{2} l_x$. Such configuration is plotted as shown in Fig. 3.5 for $h \sim q^2$, which denotes a Skyrmion lattice. On the other hand, a graph with spin projected on the basal plane (x-y plane) and a density plot of $n_z = z_i^* \sigma_z^{ij} z_j$ is plotted in Fig. 3.5.

To know the magnetization and the core size, we have to put Eq. (3.21) back to the action in Eq. (B.5) and determine them by variational method. Since the lattice is periodic, it is valid and convenient to consider the solution of a single site in Eq. (3.20a). Define

$$\tilde{h} = \frac{h}{q^2}, \tag{3.22a}$$

$$\mathcal{D} = \left[\frac{1}{2} + \frac{H}{4aq^2m\tilde{h}} + \sqrt{\frac{1}{4} + \frac{1}{2\tilde{h}} + \frac{H}{4aq^2m\tilde{h}} + \left(\frac{H}{4aq^2m\tilde{h}}\right)^2}\right]^{-1}, \tag{3.22b}$$

the free energy per unit volume of one Skyrmion in the lattice is given by

$$\frac{\mathcal{F}}{V} = \frac{r}{2}m^2 + \frac{u}{4}m^4 + aq^2m^2\frac{\tilde{h}\left(1+\frac{3\mathcal{D}^2}{2\tilde{h}}\right) - 2\mathcal{D}}{1+\frac{\mathcal{D}^2}{2\tilde{h}}} - Hm\frac{1-\frac{\mathcal{D}^2}{2\tilde{h}}}{1+\frac{\mathcal{D}^2}{2\tilde{h}}}. \tag{3.23}$$

Then we evaluate magnetization m and the reciprocal of core area h by minimizing the free energy. There exists no analytic closed form solution for m and h, but we do it by qualitative analysis. We expect that m is of the same order of magnitude of $m_{||}$ in the aligned conical phase or the paramagnet, and $\frac{h}{q^2} < 1$. Expanding Eq. (3.23) for small $\frac{h}{q^2}$, we get

$$\frac{\mathcal{F}}{V} \approx \frac{r}{2}m^2 + \frac{u}{4}m^4 - Hm + aq^2m^2\left(\frac{h}{q^2}\right) - \frac{4a^3q^6m^4}{H^2}\left(\frac{h}{q^2}\right)^2.$$

Minimizing it with respect to h and m, we get

$$\frac{h}{q^2} \approx \frac{H^2}{8a^2q^4m^2},$$

$$rm + um^3 - H \approx 0.$$

The second equation indicates that the magnetization is approximately equal to the paramagnet or ferromagnet. For small magnetic field $r > 0$, using Eq. (A.2a), we

get

$$h \approx \frac{1}{8q^2\xi_p^4}. \tag{3.24}$$

Therefore, the core-to-core distance goes like $q\xi_p^2$. We will discuss more about this result in Section 7.5. In this representation, we derived an Abrikosov lattice of Skyrmion as a solution to the saddle-point equation of the model given by Eqs. (2.2) and (2.3a).

3.4 $O(g_{\rm so}^4)$: Crystal-field effects

To fourth order in $g_{\rm so}$, we need to take into account the crystal-field terms shown in Eq. (2.4a). This makes the saddle-point equations very complicated, and no exact solution is known. We therefore take a variational approach by inserting Eq. (3.1a) into the action and minimizing with respect to the parameters of the *ansatz*. Of all the members of the class of functions represented by Eqs. (3.1) this will yield the one with the lowest free energy.

By writing Eq. (2.4a) we have fixed the coordinate system by choosing the crystallographic axes to be the $x, y, z \equiv 1, 2, 3$ axes. We thus are no longer free to choose the direction of $\mathbf{H}$, $m_{||}$, or $\mathbf{q}$. For simplicity, we will consider only the case of a magnetic field along the z-axis: $\mathbf{H} = (0, 0, H)$. Define $\hat{\mathbf{q}} \equiv \frac{\mathbf{q}}{q}$. We parameterize in terms of angles ϑ and φ as follows,

$$\hat{\mathbf{q}} = (\sin\vartheta\,\cos\varphi, \sin\vartheta\,\sin\varphi, \cos\vartheta) \equiv (\beta_1, \beta_2, \beta_3), \tag{3.25a}$$

with $\sum_{i=1}^{3} \beta_i^2 = 1$. This leaves one free parameter for $\hat{\mathbf{e}}_+$, namely, an azimuthal

angle φ_e:

$$\hat{\mathbf{e}}_+ = (\cos\vartheta\,\cos\varphi\,\sin\varphi_e - \sin\varphi\,\cos\varphi_e, \cos\vartheta\,\sin\varphi\,\sin\varphi_e + \cos\varphi\,\cos\varphi_e, -\sin\vartheta\,\sin\varphi_e). \tag{3.25b}$$

This uniquely determines $\hat{\mathbf{e}}_- = \hat{\mathbf{q}} \times \hat{\mathbf{e}}_+$. Finally, $m_{||}$ in general needs to be decomposed into components parallel and perpendicular, respectively, to $\mathbf{q}$. [81] However, while a perpendicular component can lead to a slightly lower free energy, it has no qualitative effects on the structure of the phase diagram, and we therefore restrict our ansatz to

$$\mathbf{m}_{||} = m_{||}\hat{\mathbf{q}}. \tag{3.25c}$$

We further assume that the system is sufficiently close to a second order or weakly first order phase transition that one can neglect the last term in Eq. (2.4a). With these approximations, the free energy does not depend on the angle φ_e and is completely parameterized in terms of six parameters, namely: two amplitudes, $m_{||}$ and $m_{sp} = \frac{[(m_{sp}^+)^2+(m_{sp}^-)^2]^{1/2}}{\sqrt{2}}$, the polarization parameter π, the modulus q, and the two direction angles ϑ and φ. We find

$$\begin{aligned} f(m_{||}, m_{sp}, \delta\pi, q, \vartheta, \varphi) \;=\; & \frac{1}{2}\delta t m_{||}^2 + \frac{r-aq^2}{2}(m_{||}^2 + m_{sp}^2) + \frac{u}{4}(m_{||}^2 + m_{sp}^2)^2 \\ & + \frac{1}{2}m_{sp}^2\left[\delta t + aq^2 - cq + \frac{1}{2}cq(\delta\pi)^2\right] - Hm_{||}\cos\vartheta \\ & + \frac{b}{4}m_{sp}^2 q^2 B_{\mathrm{s}}(\vartheta,\varphi) + \frac{b_1}{4}m_{sp}^2 q^2 B_{1\mathrm{s}}(\vartheta,\varphi) \\ & - \frac{b}{4}m_1^2 q^2 \delta\pi B_{\mathrm{a}}(\vartheta,\varphi) - \frac{b_1}{4}m_1^2 q^2 \delta\pi B_{1\mathrm{a}}(\vartheta,\varphi) + O(g_{\mathrm{so}}^8). \end{aligned} \tag{3.26a}$$

Here we have defined $\delta t = \frac{cq}{2}$ at this point. We also have made use of the fact that we

know, from Section 3.2, that the physical solution has the property $\pi = 1 + \delta\pi$ with $\delta\pi = O(g_{\rm so}^2)$, and have expanded in powers of $\delta\pi$. The angle-dependent functions in Eq. (3.26a) are

$$\begin{aligned} B_{\rm s,a}(\vartheta,\varphi) &= B^+(\vartheta,\varphi) \pm B^-(\vartheta,\varphi), \\ B_{\rm 1s,a}(\vartheta,\varphi) &= B_1^+(\vartheta,\varphi) \pm B_1^-(\vartheta,\varphi), \end{aligned} \tag{3.26b}$$

where

$$\begin{aligned} B^+(\vartheta,\varphi) &= 2\sin^2\vartheta\sin^2\varphi\cos^2\varphi, \\ B^-(\vartheta,\varphi) &= \sin^2\vartheta\cos^2\vartheta(1+\sin^4\varphi+\cos^4\varphi), \\ B_1^+(\vartheta,\varphi) &= \sin^2\vartheta\cos^4\varphi+\cos^2\vartheta\sin^2\varphi, \\ B_1^-(\vartheta,\varphi) &= \sin^4\vartheta\sin^2\varphi+\cos^4\vartheta\cos^2\varphi \\ &\quad +\sin^2\vartheta\cos^2\vartheta\sin^2\varphi\cos^2\varphi. \end{aligned} \tag{3.26c}$$

We now need to minimize the free energy with respect to the six parameters. We will first consider the case $H = 0$ to understand the pinning of the helix by the crystal-field terms, and then determined the effects of a magnetic field. Furthermore, in order to keep the discussion transparent we will initially restrict ourselves to an *ansatz* with a circular polarization, $\delta\pi = 0$. This suffices to understand the existence of the critical field H_{c1}. We will then generalize the *ansatz* to allow for a non-circular polarization and show that this leads to a splitting of the transition at H_{c1}, with a first order transition from a circularly polarized helix to an elliptically polarized one at a critical field $H'_{c1} < H_{c1}$ preceding the alignment transition at H_{c1}.

3.4.1 Pinning of the helix

We consider the system at $H = 0$ and initially restrict our *ansatz* to the case of circular polarization, $\delta\pi = 0$. The remaining angular dependence in the free energy, Eq. (3.26a), is contained in the functions $B_{\rm s}$ and $B_{\rm 1s}$. Minimizing with respect to φ we find that there are two cases.

Case (1): $\varphi = 0, \frac{\pi}{2}, \pi, \frac{3\pi}{2}$. This implies $\hat{\mathbf{q}} = (0, \pm\sin\vartheta, \cos\vartheta)$ or $(\pm\sin\vartheta, 0, \cos\vartheta)$, and $B_{\rm s} = \frac{1}{2}\sin^2 2\vartheta$, $B_{\rm 1s} = \sin^2\vartheta + \cos^4\vartheta$. Minimizing with respect to ϑ leads to two subcases:

Case (1a): $2b < b_1$. The free energy is minimized by $\vartheta = \frac{\pi}{4}, \frac{3\pi}{4}, \frac{5\pi}{4}, \frac{7\pi}{4}$, which implies $\hat{\mathbf{q}} = \frac{(1,0,1)}{\sqrt{2}}$ or equivalent.

Case (1b): $2b > b_1$. The free energy is minimized by $\vartheta = 0, \frac{\pi}{2}, \pi, \frac{3\pi}{2}$, which implies $\hat{\mathbf{q}} = (1, 0, 0)$ or equivalent.

Case (2): $\varphi = \frac{\pi}{4}, \frac{3\pi}{4}, \frac{5\pi}{4}, \frac{7\pi}{4}$. This implies $\hat{\mathbf{q}} = (\frac{\sin\vartheta}{\sqrt{2}}, \frac{\sin\vartheta}{\sqrt{2}}, \cos\vartheta)$ or equivalent, and $B_{\rm s} = 1 - \frac{\sin^4\vartheta}{2} - \cos^4\vartheta$, $B_{\rm 1s} = 1 - \sin^2\vartheta + \frac{3\sin^4\vartheta}{4}$. Minimizing with respect to ϑ yields

Case (2a): $2b < b_1$. The free energy is minimized by $\vartheta = \pm\arcsin\sqrt{\frac{2}{3}}$, which implies $\hat{\mathbf{q}} = \frac{(1,1,1)}{\sqrt{3}}$ or equivalent.

Case (2b): $2b > b_1$. The free energy is minimized by $\vartheta = 0, \pi$, which implies $\hat{\mathbf{q}} = (0, 0, \pm 1)$.

By comparing the resulting free energies for these cases we see that Case (1b) provides the minimum for $b > \frac{b_1}{2}$, whereas Case (2a) provides the minimum for

$b < \frac{b_1}{2}$. This is a generalization of the result obtained in Ref.[73], which considered a model with $b_1 = 0$.

In helimagnets such as MnSi and FeGe, the pinning is observed to be in the $\langle 1,1,1\rangle$-directions, which implies $b < \frac{b_1}{2}$, and we will mostly consider this case from now on. Minimizing the free energy with respect to q, we find

$$q = \frac{c}{2\left[a + \frac{b+b_1}{3}\right]}, \tag{3.27}$$

which generalizes Eq. (2.5). Minimizing with respect to m_1 we finally have

$$f = -\frac{(r-\delta t)^2}{4u}, \tag{3.28a}$$

where

$$\delta t = \frac{c^2}{4\left[a + \frac{b+b_1}{3}\right]}. \tag{3.28b}$$

These results are valid for $H = 0$ and $b < \frac{b_1}{2}$.

3.4.2 The alignment transition, and the critical field H_{c1}

For $H > 0$ we expect the pitch vector to move away from $(1,1,1)$ towards $(0,0,1)$. The calculation proceeds as for $H = 0$, except that now the minimization with respect to ϑ yields an H-dependent result. For Case (2a) we find

$$\beta_3 \equiv \cos\vartheta = \begin{cases} 1 & \text{if } H \geq H_{c1} \\ \frac{1}{3}\left(1 + \frac{2H^2}{{H_{c1}}^2}\right) & \text{if } H < H_{c1}, \end{cases} \tag{3.29a}$$

where (remember $r < \delta t$ and $b < b_1/2$ in the ordered phase for Case (2a))

$$H_{c1}^2 = \frac{(r-\delta t)\left(b - \frac{b_1}{2}\right)(\delta t)^2}{ua}. \tag{3.29b}$$

The helical pitch vector $\hat{\mathbf{q}}$ thus moves continuously along the shortest path from its initial value, $\frac{(1,1,1)}{\sqrt{3}}$ at $H = 0$, to $(0, 0, 1)$ at $H = H_{c1}$, and remains in that position for $H > H_{c1}$. There thus is a second order transition at $H = H_{c1}$ [81] that we refer to as the alignment transition. An inspection shows that Case (1b) has a larger free energy for all $H < H_{c1}$.

For reference in the next subsection we mention that if one expands the free energy for small values of ϑ, and looks for the instability of the solution with $\vartheta = 0$, one finds that the latter occurs at $H = H_{c1}$, as expected.

3.4.3 The polarization transition, and the critical field H'_{c1}

The circular polarization *ansatz* we have used so far explains the two critical fields H_{c1} and H_{c2} observed in MnSi. However, the solution obtained in this way misses a qualitative feature, as was first pointed out in Ref. [82] on symmetry grounds. Since in general $b \neq b_1$, the crystal-field contribution to the action, Eq. (2.4a), is not invariant under $x \leftrightarrow y$. As a result, there is no reason for the x and y-components of $\hat{\mathbf{q}}$ to become nonzero at the same value of H as H is lowered from above, yet the solution constructed in the previous subsection has this property. Clearly, this is a result of the fact that our *ansatz* with circular polarization possesses cubic symmetry, while the action does not. In general, one therefore expects two separate transitions in the vicinity of H_{c1}; one where the x-component of $\hat{\mathbf{q}}$ becomes nonzero, and a separate one where the y-component becomes nonzero. We now show that this expectation is borne out if we allow for a non-circular polarization of the

helix, which breaks the cubic symmetry of the *ansatz*.

Consider the full Eq. (3.26a), allowing for $\delta\pi \neq 0$. Minimizing with respect to φ we see that there are two distinct cases.

Case (1): $\varphi = 0, \frac{\pi}{2}, \pi, \frac{3\pi}{2}$ and $\delta\pi$ arbitrary. Minimizing with respect to $\delta\pi$ yields

$$\delta\pi(\vartheta) = \frac{q}{2c}\left[bB_{\mathrm{a}}(\vartheta) + b_1 B_{1\mathrm{a}}(\vartheta)\right]. \tag{3.30a}$$

That is, the polarization is in general elliptical. We have $B^+ = 0$, $B^- = 2\sin^2\vartheta\cos^2\vartheta$, which leads to

$$B_{\mathrm{s,a}} = \pm\frac{1}{2}\sin^2 2\vartheta, \tag{3.30b}$$

$$B_{1\mathrm{s}} = \sin^2\vartheta + \cos^4\vartheta. \tag{3.30c}$$

Considering $B_{1\mathrm{a}}$, we find two subcases. The first one is

Case (1)(i): $\varphi = 0, \pi$, which implies

$$\hat{\mathbf{q}} = (\pm\sin\vartheta, 0, \cos\vartheta), \tag{3.31a}$$

and

$$B_{1\mathrm{a}} = \sin^2\vartheta - \cos^4\vartheta. \tag{3.31b}$$

The second one is

Case (1)(ii): $\varphi = \frac{\pi}{2}, \frac{3\pi}{2}$, which implies

$$\hat{\mathbf{q}} = (0, \pm\sin\vartheta, \cos\vartheta), \tag{3.32a}$$

and

$$B_{1s,a} = \cos^2\vartheta \pm \sin^4\vartheta. \tag{3.32b}$$

The second case is

Case (2): $\varphi = \frac{\pi}{4}, \frac{3\pi}{4}, \frac{5\pi}{4}, \frac{7\pi}{4}$ and

$$\delta\pi = 0. \tag{3.33a}$$

That is, the polarization is circular. This implies

$$\hat{\mathbf{q}} = \left(\frac{1}{\sqrt{2}} \sin\vartheta, \frac{1}{\sqrt{2}} \sin\vartheta, \cos\vartheta \right), \tag{3.33b}$$

and

$$B_{\rm s} = 1 - \frac{1}{2}\sin^4\vartheta - \cos^4\vartheta, \tag{3.33c}$$

$$B_{1,{\rm s}} = 1 - \sin^2\vartheta + \frac{3}{4}\sin^4\vartheta \tag{3.33d}$$

Now first consider the case $H = 0$. Minimizing with respect to ϑ one finds that, for $b < \frac{b_1}{2}$, Case (2) yields the lower free energy. [3] The physical solution is thus a circularly polarized helix pinned in the $\langle 1,1,1\rangle$ directions, and the relaxation of the condition we had imposed in Sec. 3.4.1 does not change anything. For $b > \frac{b_1}{2}$, the physical solution is an elliptically polarized helix pinned in the $\langle 0,0,1\rangle$ directions.

Next we consider a solution with $\vartheta = 0$, which we expect to be stable for sufficiently large H. It is easy to see that Case (1), which takes advantage of the possibility of an elliptical polarization, has a free energy that is lower than that of Case (2) by a term of $O(g_{\rm so}^6)$ everywhere in the conical phase, i.e., for $H < H_{c2}$. We next look for the instability of the $\vartheta = 0$ solution at small H, which can be found by

[3] More precisely, the criterion is $b < b_1/2 - 3b_1^2 q/c$. The reason for this correction is the $(\delta\pi)^2$ term in the free energy, Eq. (3.25a). We neglect this and other corrections that are of higher order in $g_{\rm so}$. For instance, there are higher-order corrections to H_{c1}.

expanding the action to second order in ϑ and looking for the zero of the coefficient of the quadratic term. As expected, this instability occurs at a field $H_{c1} = O(g_{so}^3)$. To leading order in g_{so}, H_{c1} is given by Eq. (3.29b). The values of H_{c1} for the two cases are different, but the difference is only of $O(g_{so}^5)$ and is irrelevant for the following argument.

We now have the following situation. For $H < H_{c1}$, the free energy of Case (1) is lower by a term of $O(g_{so}^6)$. However, we know that at $H = 0$ the free energy of Case (2) is lower by a term of $O(g_{so}^4)$. The two solutions cross at a field H'_{c1} given by

$$\frac{H'_{c1}}{H_{c1}} = 1 - \frac{1}{2}\sqrt{\frac{3b_1^2}{4a|b - \frac{b_1}{2}|}} = 1 - O(g_{so}^4), \tag{3.34}$$

see Fig. 3.6.

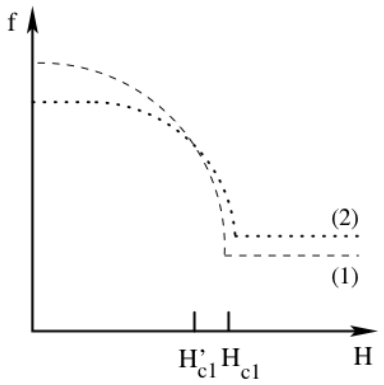

Figure 3.6: Schematic plot of the free energy density as a function of H for Case (1) (dashed line) and Case (2) (dotted line), respectively.

At this value of H, the state will change discontinuously from an elliptically polarized helix with a pitch vector given by either Eq. (3.31a) or (3.32a) to a circularly polarized one with a pitch vector given by Eq. (3.33b).

We now have the following progression of phases and phase transitions as the magnetic field is lowered from a value greater than H_{c2}: $H > H_{c2}$: Field-polarized state, no helix. $H = H_{c2} \propto g_{\rm so}^2$: Second-order transition to a conical state with an elliptically polarized helix, $\hat{\mathbf{q}} = (0, 0, 1)$. $H = H_{c1} \propto g_{\rm so}^3$: Second-order transition to a conical state with elliptical polarization as above, but $\hat{\mathbf{q}} = (0, \sin\vartheta, \cos\vartheta)$. ϑ increases from zero with decreasing H. $H = H'_{c1} = H_{c1}[1 - O(g_{\rm so})]$: First-order transition to a conical state with circular polarization and $\hat{\mathbf{q}} = (\frac{1}{\sqrt{2}} \sin\vartheta, \frac{1}{\sqrt{2}} \sin\vartheta, \cos\vartheta)$. ϑ increases from its value at H'_{c1} with decreasing H. $H = 0$: System reaches helical state with circular polarization and $\hat{\mathbf{q}} = \frac{(1,1,1)}{\sqrt{3}}$.

The phase diagram is thus predicted to have the structure shown in Fig. 3.1, with the second order alignment transition at H_{c1} followed by a first-order polarization (and re-alignment) transition at H'_{c1}. The latter has so far not been observed experimentally.

It is an explicit realization of the type of transition first predicted by Walker [82] on symmetry grounds. It needs to be stressed that the detailed features of this transition are restricted by our *ansatz*, Eqs. (3.1); the states obtained are not true minima of the action. However, the basic physical idea, which is expected to be realized in the true ground state as well, is as follows. In the conical phase, where the helical pitch vector is aligned with the magnetic field, the system can take advantage of the lack of cubic symmetry of the action, Eq. (2.4a), by forming a helix with a non-circular polarization. This leads to an energy gain, compared to a circularly polarized state, of order $g_{\rm so}^6$. However, it forces the pitch vector into either the $y = 0$ or $x = 0$ plane, i.e., Case (1) above. At low fields, these states have a free energy

that is larger by a term of $O(g_{\rm so}^4)$ than the states with the pitch vector along a cubic diagonal, which requires a circular polarization. The competition between these two effects leads to the first order transition at H_{c1}, where both the polarization and the orientation of the pitch vector change discontinuously.

The preceding discussion pertains to the case $b < b_1$. It is worthwhile noting that the case $b > b_1$ is qualitatively different since the polarization is elliptical for any value of the magnetic field, see the remark after Eqs. (3.33). In this case, the transition at H'_{c1} is a re-alignment transition, but not a polarization transition.

3.4.4 Pinning of the columnar phase and the NFL region

Experimentally, the columnar phase is found to be pinned very weakly, and theoretical considerations conclude that the pinning potential is only of $O(g_{\rm so}^6)$. [33] This is a consequence of its six-fold rotation symmetry. Similarly one expects the (average) direction of the fluctuating defect lines in the NFL region to be pinned only very weakly.

3.5 Beyond classical mean-field theory

We have treated the phase transitions that we have discussed in this chapter within classical mean-field theory, and the question arises what changes will result from the consideration of fluctuations, classical or quantum. One example of the effects of fluctuations is the tricritical point and the associated tricritical wings shown in Fig. 1.10, which result from quantum fluctuations that can be taken into

account within a renormalized mean-field theory. [29, 75] Elsewhere in the phase diagram, fluctuations are also of qualitative importance. Consider, for instance, the transition from the conical phase to the field-polarized phase at the critical field H_{c2}, see Fig. 3.1. The transition is characterized by the vanishing of the one-dimensional order parameter m_{sp}, the amplitude of the helix, see Eqs. (3.10). The action is invariant under $m_{sp} \to -m_{sp}$, and we therefore expect this transition at nonzero temperature to be in the universality class of the classical Ising model. [71] At zero temperature the statics and the dynamics will couple, [83, 84, 85] and one expects the quantum phase transition to be described by Hertz's model [83] (see Appendix D) with a scalar order parameter. Quantum phase transition in itinerant helimagnet has been studied in Refs. [86] and [87].

3.6 Conclusion and Discussion

In this chapter, through mean-field theory, the phase diagram is a helimagnet is given as shown in Fig. 3.1. Our model gives the phases of the paramagnet, ferromagnet, conical phase, pinned helical phase, and the columnar phase. They were all found in experiments on helimagnets such as MnSi, FeGe and $Fe_{0.8}Co_{0.2}Si$, with their measured phase diagrams in Figs. 1.6, 1.7 and 1.9 respectively.

We have also predicted an elliptical conical phase, just beneath the critical field H_{c1}, due to the crystal-field effects.

On the other hand, we have not studied the phase diagram due to the change of pressure. The disordered phase at $p > p_c$ is analogous to the blue phase III in

cholestoric liquid crystal. [88] There are known hexagonal columnar phase in the liquid crystals. The blue phase III is believed to be an amorphous state, melted from these hexagonal structures. [39]

Similarly, the Skyrmion lattice approximately described by Eqs. (3.13) or (3.21) can melt, which will lead to a Skyrmion liquid. In such a state the line defects shown in Fig. 3.4 still exist, but they no longer form a lattice. Rather, their fluctuations in the plane perpendicular to the line, which are illustrated in Fig. 1.18, have become so large that the long-range order is destroyed. Such a state has recently been proposed to represent the NFL region shown in Fig. 1.11. [50] Although it is not an ordered phase, such a state has much in common with the columnar phase and we will discuss it in the context of the ordered phases. Further studies are needed to understand the nature of the NFL state.

Chapter 4

Goldstone Modes of Ordered Phases

Goldstone's theorem [42] states that if a continuous symmetry described by a Lie group G is spontaneously broken, with the remaining subgroup in the broken-symmetry phase being H (not to be confused with the magnetic field), then in the ordered phase there are n soft or massless modes, with n equal to the dimensionality of the coset space G/H. [89, 90] All of the ordered states discussed in Chapter 3 break a continuous symmetry, and therefore there must be one or more soft modes in each of the ordered phases. [1] The number and functional form of the Goldstone modes in the various phases can be determined from general arguments. In this chapter, we will do so, and augment these arguments by explicit calculations in some cases where this is feasible. Via a coupling to the conduction electrons, the Goldstone modes have interesting consequences for various observables.

[1] Strictly speaking, this is true only within a continuum model. In real magnets, the underlying lattice means that translational as well as rotational invariance is broken already in the disordered phase, and no truly massless modes will result from the order. However, since all of the phases of interest show some kind of helical order with a characteristic wave number q that obeys $qa \ll 1$, with a the lattice constant, the masses of the pseudo-Goldstone modes are exponentially small, see the discussion in Ref. [44]. Any gaps in the excitation spectra are thus unobservably small, and I will ignore this effect in this thesis.

4.1 $O(g_{\rm so}^0)$: Ferromagnons

To zeroth order in $g_{\rm so}$ the system is a ferromagnet. (See Section 3.1.) The relevant symmetry is the rotation group, $G = O(3)$, which in the ordered state is spontaneously broken to $H = O(2)$. Hence there are $\dim(O(3)/O(2)) = 2$ Goldstone modes, the well-known ferromagnons (FM). Their dispersion relation for small wave numbers is [71]

$$\omega_{\rm FM}(\mathbf{k}) = D\mathbf{k}^2, \tag{4.1}$$

with D the spin wave stiffness, which depends on the magnetization and vanishes as the magnetization goes to zero.

The easiest way to derive this result is to consider a nonlinear σ model version of the Heisenberg action. [90] Neglecting fluctuations of the amplitude of the magnetization, which can be shown to be massive, one parameterizes the order parameter

$$\mathbf{M}(\mathbf{x}) = m_{||} \begin{pmatrix} \pi_1(\mathbf{x}) \\ \pi_2(\mathbf{x}) \\ \sqrt{1 - \pi_1^2(\mathbf{x}) - \pi_2^2(\mathbf{x})} \end{pmatrix} \tag{4.2}$$

and expands the action to bilinear order in $\pi_{1,2}$. Here, $m_{||}$ is the solution of Eq. (3.8b). If we neglect the small relativistic term with coupling constant d in Eq. (2.2b), the resulting quadratic form has two identical eigenvalues

$$\lambda = \frac{m_{||}}{2} \left(a\, \mathbf{k}^2 + H \right) \tag{4.3}$$

For $H = 0$, one has $\lambda(\mathbf{k} \to 0) \to 0$, which reflects the two Goldstone modes. Physically, the homogeneous transverse magnetic susceptibility diverges. This is the

static manifestation of the spontaneously broken continuous symmetry. Determining the dynamics requires an additional step. One either needs to solve an appropriate Langevin equation within a classical context, [71] or treat the problem quantum mechanically. [83] Either way one obtains Eq. (4.1) with $D \propto m_{||}$.

4.2 $O(g_{\rm so}^2)$: Helimagnons

When the spin-orbit coupling is taken into account, we have the various phases involving helical spin textures discussed in Chapter 3. For all of these phases the relevant symmetry is the translational one. Let T be the Lie group of one-dimensional translations. Then the action is invariant under $G = T \otimes T \otimes T \equiv T^3$.

4.2.1 Symmetry arguments

Consider the aligned conical state (ACS) discussed in Section 3.2, from which the unpinned helical phase emerges as a special case at $H = 0$. T^3 is broken down to T^2 (translations in the two directions perpendicular to $\hat{\mathbf{q}} = \hat{\mathbf{H}}$), so we expect one Goldstone mode. At $H = 0$, one expects the soft fluctuations in the ordered phase to be phase fluctuations of the helix, and one might naively expect them to be governed by an action $S = \int d\mathbf{x}\ (\nabla\phi(\mathbf{x}))^2$, with ϕ the phase variable, which would lead to a soft eigenvalue proportional to $\mathbf{k}^2$, as in the ferromagnons. However, the ordered state is also invariant under rotations of $\mathbf{q}$, which can be written as a phase fluctuation with a nonvanishing gradient, so this cannot be the correct answer. The lowest-order term allowed by rotational symmetry that involves the gradients

perpendicular to $\mathbf{q}$ is of the form $(\nabla_\perp^2 u)^2$, with u a generalized phase variable, and this leads to an eigenvalue, or inverse order parameter susceptibility, proportional to the square of [2]

$$\omega_{\rm HM}(\mathbf{k}) = \sqrt{c_{||}\, k_{||}^2 + c_\perp\, \mathbf{k}_\perp^4}. \tag{4.4}$$

The spin wave corresponding to a helimagnon is shown in Fig. 4.1. [44] The dy-

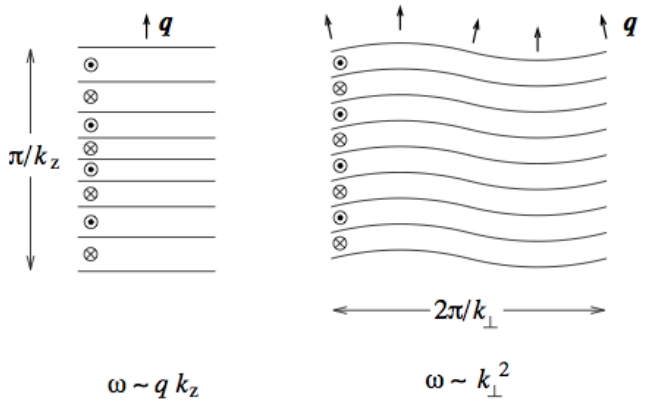

Figure 4.1: Sketch of a longitudinal (left) and transverse (right) helimagnon. The solid lines delineate planes of spins pointing out of (dotted) or into (crossed circle) the paper plane.

namics again require additional considerations, which lead to a resonance frequency that is proportional to the square root of the inverse susceptibility, unlike the ferromagnetic case, and this is expressed in Eq. (4.4). [3] These results were first obtained

[2]These arguments are the same as for cholesteric or smectic liquid crystals, see Ref. [24]. It should be noted, however, that the result is slightly different for electronic smectics and helical magnets, respectively, whereas for liquid crystals there is no difference between smectics and cholesterics in this respect, see Ref. [91].

[3]It is not entirely obvious that the dynamical part of the action density is $(\partial_t u)^2$, which leads to the square root in Eq. (4.4). Establishing this requires an explicit calculation, see Ref. [44].

by means of an explicit calculation for both classical and quantum helimagnets in Ref. [44].

A magnetic field breaks the rotational invariance, so a $\mathbf{k}_\perp^2$-term will be present in the dispersion relation. The prefactor is expected to be analytic in H, and we thus expect for the dispersion relation of this "conimagnon", the Goldstone mode of the ACS in Eqs. (3.10),

$$\omega_{\mathrm{ACS}}(\mathbf{k}) = \sqrt{c_{||}\, k_{||}^2 + c'_\perp\, \mathbf{k}_\perp^2 + c_\perp\, \mathbf{k}_\perp^4}, \tag{4.5}$$

with $c'_\perp \propto H^2$.

4.2.2 Model calculation

For the action to $O(g_{\mathrm{so}}^2)$, Eqs. (3.10) constitute an exact saddle-point solution, and we can perform an explicit calculation of the Goldstone mode. A complete parameterization of fluctuations about the saddle point can be written

$$\mathbf{M}(\mathbf{x}) = \big(m_{||} + \delta m_{||}(\mathbf{x})\big) \begin{pmatrix} \pi_1(\mathbf{x}) \\ \pi_2(\mathbf{x}) \\ \sqrt{1-\pi_1^2(\mathbf{x})-\pi_2^2(\mathbf{x})} \end{pmatrix} + \frac{m_{sp}+\delta m_{sp}(\mathbf{x})}{\sqrt{1+\psi^2(\mathbf{x})}} \begin{pmatrix} \cos(qz+\varphi_0(\mathbf{x})) \\ \sin(qz+\varphi_0(\mathbf{x})) \\ \psi(\mathbf{x}) \end{pmatrix}. \tag{4.6}$$

The first term is the nonlinear σ-model for the homogeneous magnetization from Section 4.1, and the second one parameterizes fluctuations of the helix in terms of an amplitude modulation, a phase φ_0, and a third component ψ. [44] The amplitude fluctuations one expects to be massive, and an explicit calculation confirms this, so

we drop $\delta m_{||}$ and δm_{sp}. The field $\psi(\mathbf{x})$ is conveniently written

$$\psi(\mathbf{x}) = \varphi_+(\mathbf{x})\cos(\mathbf{q}\cdot\mathbf{x}) + \varphi_-(\mathbf{x})\sin(\mathbf{q}\cdot\mathbf{x}), \tag{4.7}$$

which ensure that $\varphi_\pm$ and φ_0 at zero wave number both correspond to $\mathbf{M}$ at wave number q. Double counting is avoided by restricting the theory to wave numbers small compared to q. If we use Eq. (4.6) in the action to $O(g_{\rm so}^2)$, Eqs. (2.2a) and (2.3a), and expand to bilinear order in the fluctuations $(\phi_1,\phi_2,\phi_3,\phi_4,\phi_5) \equiv (\varphi_0,\varphi_+,\varphi_-,\pi_1,\pi_2)$, we obtain a Gaussian action

$$\mathcal{S}^{(2)} = \frac{am_{sp}^2}{2V}\sum_{\mathbf{k}}\sum_{i=1}^{5}\phi_i(\mathbf{k})\gamma_{ij}(\mathbf{k})\phi_j(-\mathbf{k}), \tag{4.8a}$$

where

$$\gamma(\mathbf{k}) = \begin{pmatrix} k^2 & -iqk_y & iqk_x & 0 & 0 \\ iqk_y & q^2+\frac{k^2}{2}+\frac{1}{\xi_h'^2}\frac{H^2}{H_{c2}^2} & -iqk_z & 0 & \frac{1}{\xi_h'^2}\frac{H^2}{H_{c2}^2} \\ -iqk_x & iqk_z & q^2+\frac{k^2}{2}+\frac{1}{\xi_h'^2}\frac{H^2}{H_{c2}^2} & \frac{1}{\xi_h'^2}\frac{H^2}{H_{c2}^2} & 0 \\ 0 & 0 & \frac{1}{\xi_h'^2}\frac{H^2}{H_{c2}^2} & \frac{m_{||}^2}{m_{sp}^2}\left(q^2+k^2+\frac{1}{\xi_h'^2}\right) & 2iqk_z\frac{m_{||}^2}{m_{sp}^2} \\ 0 & \frac{1}{\xi_h'^2}\frac{H^2}{H_{c2}^2} & 0 & -2iqk_z\frac{m_{||}^2}{m_{sp}^2} & \frac{m_{||}^2}{m_{sp}^2}\left(q^2+k^2+\frac{1}{\xi_h'^2}\right) \end{pmatrix}. \tag{4.8b}$$

Of the five eigenvalues, one goes to zero for $\mathbf{k}\to 0$, in agreement with the expectation from the symmetry arguments given above. It takes the form

$$\lambda_1 = \alpha k_z^2 + \beta\mathbf{k}_\perp^2 + \delta\mathbf{k}_\perp^4, \tag{4.9a}$$

with coefficients

$$\alpha = 1, \tag{4.9b}$$

$$\beta = \frac{\xi_h'^{-2}}{q^2+\xi_h'^{-2}}\left(\frac{H}{H_{c2}}\right)^2, \tag{4.9c}$$

$$\delta = \frac{1}{2q^2(q^2+\xi_h'^{-2})^3}\left\{\left[q^2+\frac{1}{\xi_h'^2}\left(1-\frac{H^2}{H_{c2}^2}\right)\right]^3-\frac{1}{\xi_h'^2}\frac{H^2}{H_{c2}^2}\left[q^4+\frac{1}{\xi_h'^4}\left(1-\frac{H^2}{H_{c2}^2}\right)^2\right]\right\}. \tag{4.9d}$$

This result is consistent with Eq. (4.5). For $H = 0$, which implies $m_{sp} = 0$, it reduces to the helimagnon result of Ref. [44]. In addition, there are four massive eigenvalues that appear in pairs. At zero wave number, they are

$$\lambda_2 = \lambda_3 \equiv \lambda_\varphi = q^2[1+\frac{1}{q^2\xi_h'^2}\frac{H^2}{H_{c2}^2}+O(H^4)], \tag{4.10a}$$

$$\lambda_3 = \lambda_4 \equiv \lambda_\pi = \frac{q^2H^2}{H_{c2}^2-H^2}[1+\frac{1}{\xi_h'^2}\frac{H_{c2}^2-H^2}{H_{c2}^2}]+O(H^4). \tag{4.10b}$$

We recognize λ_φ as representing the massive helimagnon modes, [44] modified by the presence of homogeneous magnetization $m_{||}$, and λ_π as the massive (due to the presence of a magnetic field) ferromagnons, Eq. (4.3), modified by the presence of helimagnetic component m_{sp}. The massless helimagnon mode is given by Eq. (7.10).

4.3 $O(g_{\rm so}^2)$: Goldstone modes in the columnar phase and the NFL region

The helical states that have been proposed as candidates for the A phase and were discussed in Section 3.3.1 are not saddle-point solutions of the action,

which precludes a model calculation of the Goldstone modes resulting from this type of order. [4] The solution in Section 3.3.2 is exact, but the fluctuation around it is still yet to be studied. However, assuming that the order is stabilized by some mechanism, the functional form of the soft modes can still be determined by symmetry arguments analogous to those put forward in the previous subsection.

Like all other columnar phases, the state described by Eq. (3.13) or Eq. (3.21) is invariant only under translations in one direction, viz., the direction perpendicular to the plane of helices. The same is true for any state that is characterized by columnar order, so this property does not depend on the precise nature of the columns. Any such state will thus have $\dim(T^3/T) = 2$ Goldstone modes. This was to be expected: Since the columns form a two-dimensional lattice, there should be two generalized phonon modes, namely, a compression mode and a shear mode. In zero magnetic field, the energy would still be invariant under global rotations of the skyrmion lattice. Hence, the soft eigenvalue can have no k_z^2 contribution. For $H \neq 0$ this is no longer true, and we thus expect

$$\lambda = \alpha \mathbf{k}_\perp^2 + \beta k_z^4 + \gamma k_z^2, \tag{4.11}$$

for the soft eigenvalue, with $\gamma \propto H^2$, and

$$\omega_{\mathrm{SL}}(\mathbf{k}) = \sqrt{c_\perp \mathbf{k}_\perp^2 + c_z' k_z^2 + c_z k_z^4}, \tag{4.12}$$

for the dispersion relation, with $c_\perp, c_z = O(1)$ and $c_z' = O(H^2)$.

[4] After our paper [48] was published, the spectrum of the Goldstone modes of this three-helix form of Skyrmion lattice was derived in Ref. [92].

If the NFL region can be interpreted as a molten A crystal (see Chapter 3), then one of the two Goldstone modes, the compression mode, will persist as long as their is columnar structure. This is analogous to the fact that longitudinal phonons, or ordinary sound, exist in a liquid, whereas in a crystal one has transverse phonons or shear modes in addition. The NFL region extends to $H = 0$, where the dispersion relation of the compressional Goldstone mode is given by Eq. (4.12) with $c_z' = 0$ to first order in $g_{\rm so}$.

4.4 $O(g_{\rm so}^4)$: Effects of the crystal-field terms

4.4.1 Symmetry arguments

Now consider the crystal-field terms in the action that first appear at $O(g_{\rm so}^4)$, Eq. (2.4a). For simplicity, let us consider the term with coupling constant b (the pinning term) with $H = 0$. It breaks rotational invariance, which invalidates the argument that leads to the absence of a $\mathbf{k}_\perp^2$-term in the soft mode resonance frequency. The system must remain stable regardless of the sign of b, and we thus expect for the dispersion relation of the helimagnons in the pinned helical state

$$\omega_{\rm HM}(\mathbf{k}) = \sqrt{c_{||} k_{||}^2 + c_\perp'' \mathbf{k}_\perp^2 + c_\perp \mathbf{k}_\perp^4}, \tag{4.13}$$

with $c_\perp'' \propto |b|$, which replaces Eq. (4.4). For the more general model given by Eqs. (2.1) - (2.4), b_1, v, and H will also contribute to the elastic constant $c_\perp''$.

4.4.2 Model calculation

We now check this expectation by means of an explicit calculation. For the model with only the first of the crystal-field terms present, we have an exact saddle-point solution, namely,

$$\mathbf{M}(\mathbf{x}) = m_{sp}\left[\hat{\mathbf{e}}_+ \cos(\mathbf{q}\cdot\mathbf{x}) + \hat{\mathbf{e}}_- \sin(\mathbf{q}\cdot\mathbf{x})\right], \tag{4.14a}$$

with $\hat{\mathbf{e}}_+$, $\hat{\mathbf{e}}_-$, and $\mathbf{q}$ a *dreibein*, and

$$m_{sp} = \sqrt{\frac{aq^2 - r}{u}}, \tag{4.14b}$$

where

$$\mathbf{q} = q \begin{cases} \frac{(1,1,1)}{\sqrt{3}} & \text{if } b < 0 \\ (1,0,0) & \text{if } b > 0, \end{cases} \tag{4.14c}$$

$$q = \begin{cases} \frac{c}{2\left(a+\frac{b}{3}\right)} & \text{if } b < 0 \\ \frac{c}{2a} & \text{if } b > 0. \end{cases} \tag{4.14d}$$

The parameterization of fluctuations about this state is given by the second term in Eq. (4.6):

$$\mathbf{M}(\mathbf{x}) = (m_{sp} + \delta m_{sp})\left[\hat{\mathbf{e}}_+ \cos(\mathbf{q}\cdot\mathbf{x} + \varphi_0(\mathbf{x})) + \hat{\mathbf{e}}_- \sin(\mathbf{q}\cdot\mathbf{x} + \varphi_0(\mathbf{x})) + \hat{\mathbf{q}}\psi(\mathbf{x})\right], \tag{4.15}$$

with $\psi(\mathbf{x})$ given by Eq. (4.7). We again drop the massive amplitude fluctuations and expand the action to quadratic order in the phase fluctuations. The Gaussian action is of the form

$$\mathcal{A}^{(2)}[\varphi_i] = \frac{m_1^2}{2} \sum_{\mathbf{k}} \sum_{\alpha=0,\pm} \varphi_\alpha(\mathbf{k}) \Gamma_{\alpha\beta}(\mathbf{k}) \varphi_\beta(\mathbf{k}). \tag{4.16}$$

The explicit form of the matrix Γ depends on the sign of b. Neglecting rapidly fluctuating Fourier components proportional to $e^{in\mathbf{q}\cdot\mathbf{x}}$ with $n \geq 2$ one finds

$$\begin{aligned}\frac{\mathcal{A}^{(2)}[\delta\mathbf{M}]}{m_{sp}^2} &= \frac{1}{2}\int d\mathbf{x}\varphi_0(\mathbf{x})\left[r + aq^2 - cq + um_{sp}^2 + \frac{b}{2}\sum_{i=1}^{3} q_i^2\left[(\hat{e}_+^i)^2 + (\hat{e}_-^i)^2\right]\right]\varphi_0(\mathbf{x}) \\ &+\frac{1}{4}\int d\mathbf{x}\ \sum_{\alpha=\pm}\varphi_\alpha(\mathbf{x})\left[r + aq^2 + um_{sp}^2 + bq^2\sum_{i=1}^{3}\hat{q}_i^4\right]\varphi_\alpha(\mathbf{x}) \\ &-\frac{1}{2}bq^2\int d\mathbf{x}\ \sum_{\alpha=\pm}\sum_{i=1}^{3}\hat{e}_\alpha^i\hat{q}_i^3\varphi_0(\mathbf{x})\varphi_\alpha(\mathbf{x}) + (\text{gradient terms}) \qquad (4.17)\end{aligned}$$

An explicit calculation shows that

$$\sum_{i=1}^{3}\hat{q}_i^2\left[(\hat{e}_+^i)^2 + (\hat{e}_-^i)^2\right] = 1 - f(\hat{\mathbf{q}}), \qquad (4.18a)$$

$$\sum_{i=1}^{3}\hat{q}_i^4 = f(\hat{\mathbf{q}}), \qquad (4.18b)$$

with

$$f(\hat{\mathbf{q}}) = \beta_1^4 + \beta_2^4 + \beta_3^4, \qquad (4.18c)$$

where $\beta_{1,2,3}$ are the direction cosines of $\hat{\mathbf{q}}$. Furthermore,

$$\sum_{i=1}^{3}\hat{e}_\alpha^i\,(\hat{q}_i)^3 = 0 \qquad (4.18d)$$

for $\alpha = +, -$ and for both $\hat{\mathbf{q}} = \frac{(1,1,1)}{\sqrt{3}}$ and $\hat{\mathbf{q}} = (1,0,0)$. Then φ_0-φ_α vertices vanish. Using the equation of state, Eq. (4.14b), we see that the φ_0-φ_0 vertex and the φ_α-φ_α vertices all vanish. At zero wave number we thus have one zero eigenvalue that corresponds to one Goldstone mode, in agreement with the expectation from Section 4.2.1.

We next calculate the gradient-squared terms. Geometric identities similar to those expressed in Eqs. (4.18) allow to determine the vertices. One finds a Gaussian

action of the form given by Eq. (4.16). For $b > 0$, the matrix Γ is given by

$$\Gamma(\mathbf{k}) = \begin{pmatrix} a\mathbf{k}^2 + \frac{b}{2}\mathbf{k}_\perp^2 & -i\frac{c}{2}k_y & -i\frac{c}{2}k_x \\ i\frac{c}{2}k_y & \frac{cq}{2} + \frac{a}{2}\mathbf{k}^2 + \frac{b}{2}k_z^2 & i(a+b)qk_z \\ i\frac{c}{2}k_x & -i(a+b)qk_z & \frac{cq}{2} + \frac{a}{2}\mathbf{k}^2 + \frac{b}{2}k_z^2 \end{pmatrix} . \tag{4.19}$$

For $b < 0$, the matrix Γ takes the form

$$\begin{aligned} \Gamma_{00}(\mathbf{k}) &= \left(a + \frac{b}{3}\right) k^2, \\ \Gamma_{0+}(\mathbf{k}) &= \Gamma_{+0}(\mathbf{k})^* = i\left(\frac{c}{2} + \frac{bq}{3}\right)\frac{1}{\sqrt{2}}(k_{||} - 3k_z) + \frac{b}{2\sqrt{6}}(k_x^2 - k_y^2), \\ \Gamma_{0-}(\mathbf{k}) &= \Gamma_{-0}(\mathbf{k})^* = i\left(\frac{c}{2} + \frac{bq}{3}\right)\frac{1}{\sqrt{2}}(k_x - k_y) - \frac{b}{2\sqrt{6}}(k_x^2 + k_y^2 - 2k_z^2), \\ \Gamma_{++}(\mathbf{k}) &= \Gamma_{--}(\mathbf{k}) = \frac{cq}{2} + \frac{1}{2}\left(a + \frac{b}{3}\right) k^2, \\ \Gamma_{+-}(\mathbf{k}) &= \Gamma_{-+}(\mathbf{k})^* = i\left(a + \frac{b}{3}\right) qk_{||} \end{aligned} \tag{4.20}$$

An inspection of the eigenvalues shows that in either case there is one eigenvalue λ that vanishes as $\mathbf{k} \to 0$ and hence represents the Goldstone mode, as expected from the symmetry argument given above. To order $k_{||}^2$ and $\mathbf{k}_\perp^4$ we find

$$\lambda = \begin{cases} ak_{||}^2 + \frac{b}{2}\mathbf{k}_\perp^2 + \frac{a+b}{2}\frac{\mathbf{k}_\perp^4}{q^2}, & \text{if } b > 0, \\ \left(a + \frac{b}{3}\right)k_{||}^2 + \frac{2}{3}|b|\mathbf{k}_\perp^2 + \frac{a+b+O(g_{\rm so}^4)}{2}\frac{\mathbf{k}_\perp^4}{q^2}, & \text{if } b < 0. \end{cases} \tag{4.21}$$

In the case $b < 0$ we have neglected terms proportional to $b^2 = O(g_{\rm so}^4)$ in the prefactor of $\frac{\mathbf{k}_\perp^4}{q^2}$. This result agrees with the functional form obtained by symmetry arguments alone, Eq. (4.13), and for $b = 0$ it correctly reduces to the result for the isotropic model in Eq. (4.4). [44]

4.4.3 Generalized helimagnons

We can now summarize the results for the single-helix phases discussed above as follows. In the helical and conical phases, including pinning effects, there is a single Goldstone mode with a resonance frequency

$$\omega_0(\mathbf{k}) = \sqrt{c_{||} k_{||}^2 + \tilde{c}_\perp \mathbf{k}_\perp^2 + c_\perp \mathbf{k}_\perp^4}, \tag{4.22}$$

with $\tilde{c}_\perp = O(H^2, g_{\rm so}^2)$ small compared to $c_{||}$ and $c_\perp$. This comprises Eqs. (4.5) and (4.13). From our results, we can also see the crossover between the regimes where $\tilde{c}_\perp$ is dominated by pinning and magnetic field effects, respectively. Eqs. (4.16), (4.21), (4.8a) and (4.9) imply that deep inside the ordered phase $\tilde{c}_\perp$ is well represented by

$$\tilde{c}_\perp \propto |b| + a\frac{H^2}{H_{c2}^2}. \tag{4.23}$$

Since $H_{c1}^2 \approx H_{c2}^2 \frac{|b|}{a}$,, it follows that $\tilde{c}_\perp$ is dominated by pinning and magnetic field effects for $H < H_{c1}$ and $H > H_{c1}$, respectively.

4.4.4 Columnar phase, and NFL region

In the columnar phase, pinning effects are weaker than in the helical phase due to the hexagonal nature of the lattice. When this weak pinning is taken in to account, the Goldstone mode is thus given by Eq. (4.12) with $c_z' = O(g_{\rm so}^6, H^2)$. While in MnSi the columnar phase is observed only in an external magnetic field, there is no intrinsic reason why in some other system it could not be stable in a zero field. The Goldstone modes in such a system would be given by Eq. (4.12) with an extremely small c_z'. By the same argument, in the NFL region at $H = 0$ we expect a Goldstone mode given by Eq. (4.12) with $c_z' = O(g_{\rm so}^6)$.

4.5 Temperature regimes of the generalized helimagnons

The analytical structures of the various Goldstone modes, and the fact that the various elastic coefficients have very different magnitudes, leads to the formation of different temperature regimes that are dominated by different physics. We now explain this using the generalized helimagnons, Eq. (4.22), as an example; the argument for the other cases works analogously. As far as the coupling of the magnetic Goldstone mode to the electronic degrees of freedom is concerned, the resonance frequency ω_0 scales as the temperature, $\omega_0 \sim T$. If we scale $k_{||}$ with $\frac{T}{\sqrt{c_{||}}}$ and $k_\perp$ with $\frac{\sqrt{T}}{c_\perp^{1/4}}$, we obtain

$$\omega_0(\mathbf{k}) = T\sqrt{k_{||}^2 + \mathbf{k}_\perp^2 \frac{\tilde{c}_\perp}{T\sqrt{c_\perp}} + \mathbf{k}_\perp^4}, \tag{4.24}$$

where k now denotes the scaled, dimensionless, wave number. For $T \gg \frac{\tilde{c}_\perp}{\sqrt{c_\perp}}$ the symmetry-breaking $\mathbf{k}_\perp^2$ term is negligible, and the Goldstone mode is effectively what it would be in a rotationally invariant system. In this regime the physics is dominated by universal hydrodynamic effects that are independent of the microscopic details of the solid and analogous to the corresponding effects in liquid crystals. In the opposite limit, $T \ll \frac{\tilde{c}_\perp}{\sqrt{c_\perp}}$, the crystal-field effects due to the underlying ionic lattice, or the external magnetic field, if present, dominate and the Goldstone mode has the same functional form as (anisotropic) acoustic phonons. Due to the smallness of $\tilde{c}_\perp$ the universal hydrodynamic regime is sizable, and it is in this region that the most interesting effects of the magnetic order manifest themselves in the electronic properties of the system. This is true especially if the Goldstone mode appears in zero magnetic field and the pinning is very small, such as in the NFL region or a

(so far hypothetical) A phase in zero field.

We finally mention that the generalized helimagnon dispersion relation as given by Eq. (4.22) is valid only for wave numbers $k < q$. As a result, the anisotropy dominates the temperature dependence of observables only for temperatures [93]

$$T \ll T_q = \sqrt{c_{||}}\, q. \tag{4.25}$$

T_q thus provides an upper bound for the universal hydrodynamic regime.

Distinguishing between the universal hydrodynamic regime and the crystal-field regime is essential in deriving the electronic properties of the helimagnets, see Chapter 5.

4.6 Conclusion

To summarize, we have found that the (single) Goldstone mode in the pinned helical and conical phases is given by Eq. (4.22). In the pinned helical phase, the parallel direction is determined by the crystal-field effects that pin the helix; in the conical phase, it is the direction of the magnetic field (which we have chosen to be the z-direction for all of our considerations). The elastic constant $\tilde{c}_\perp$ is small compared to the other elastic constants. In the pinned helical phase it is of $O(g_{\rm so}^2)$, and in the conical phase it is of $O(H^2)$. By contrast, $c_{||}$ and $c_\perp$ are of $O(g_{\rm so})$ and $O(g_{\rm so}^0)$, and of $O(H^0)$, respectively.

In the columnar phase, there are two Goldstone modes whose dispersion relation is given by Eq. (4.12). The elastic constant c_z' is small of $O(H^2)$ and $O(g_{\rm so}^6)$ compared to the others. In the NFL region, the single Goldstone mode is also given

by Eq. (4.12), with $c_z' = O(g_{\rm so}^6)$.

Chapter 5

Electronic Properties of Different Phases

In this chapter, we discuss the consequences of the Goldstone modes in Chapter 4 on various transport properties of the helimagnet, via a coupling between the Goldstone modes and the conduction electrons. We derive the consequences for the specific heat, the single-particle relaxation rate, and the thermal and electrical resistivities. The temperature dependence of the specific heat can be found readily. For other properties, we have to first consider a microscopic model in terms of electronic degrees of freedom that leads to the helimagnet, and build in the Goldstone bosons as the fluctuations. The single-particle relaxation rate and the transport relaxation rate can be derived from the microscopic model.

In all cases we consider the contribution of the Goldstone mode in isolation; it comes in addition to all other contributions to these observables, and the results given are valid for $T \ll T_q$, given by Eq. (4.25).

In this chapter, we use units such that $k_{\mathrm{B}} = \hbar = 1$.

5.1 Specific heat

Any well-defined (i.e., not overdamped) excitation with a dispersion relation $\omega(\mathbf{k})$ yields a contribution to the specific heat C given by [71]

$$C(T) = \frac{\partial}{\partial T} \frac{1}{V} \sum_{\mathbf{k}} \omega(\mathbf{k}) n_{\mathrm{B}}(\omega(\mathbf{k})). \tag{5.1}$$

Here $n_{\mathrm{B}}(x) = \frac{1}{\exp\left(\frac{x}{T}\right)-1}$ is the Bose distribution function, and V is the system volume. This allows one to determine the contributions to the specific heat by the various Goldstone modes.

5.1.1 Generalized helimagnons

We first consider the helical and aligned conical phase. The dispersion relation is given by Eq. (4.22). Performing the integral in Eq. (5.1) yields

$$C(T) = \text{const.} \times \begin{cases} \frac{T^3}{\sqrt{c_z}\tilde{c}_\perp} & \text{if } T \ll \frac{\tilde{c}_\perp}{\sqrt{c_\perp}} \\ \frac{T^2}{\sqrt{c_z c_\perp}} & \text{if } T \gg \frac{\tilde{c}_\perp}{\sqrt{c_\perp}} \end{cases} , \tag{5.2}$$

The universal hydrodynamic result, $C(T) \propto T^2$ is subleading to, but distinct from, the Fermi-liquid result $C(T) \propto T + O(T^3 \ln T)$. [53] At asymptotically low temperatures it crosses over to a T^3 behavior consistent with the acoustic-phonon-like dispersion relation in either the pinned helical phase or the aligned conical phase at asymptotically small wave numbers.

5.1.2 Columnar phase

In the columnar phase, we find from Eq. (4.12) in conjunction with Eq. (5.1)

$$C(T) = \text{const.} \times \begin{cases} \frac{T^3}{c_\perp c_z'} & \text{if } T \ll c_z'/\sqrt{c_z} \\ \frac{T^{5/2}}{c_\perp c_z^{1/4}} & \text{if } T \gg \frac{c_z'}{\sqrt{c_z}} \ . \end{cases} \tag{5.3}$$

5.2 Microscopic model for helimagnets

5.2.1 The action in terms of canonical variables

To get the relaxation times, we need a model beyond the LGW functional so that the electronic degrees of freedom are considered. In Refs. [44, 93], an effective action for clean itinerant electrons in the presence of long-range helical magnetic order, and helical magnetic fluctuations interacting with the electronic degrees of freedom was derived. This action can be written as

$$S_{\rm eff}[\bar{\psi},\psi] = S_0[\bar{\psi},\psi] + \frac{\Gamma_{\rm t}^2}{2}\int dxdy\, \delta n_{\rm s}^i(x)\chi_{\rm s}^{ij}(x,y)\delta n_{\rm s}^j(y), \tag{5.4}$$

where $n_{\rm s}^i(x) = \bar{\psi}_\alpha(x)\sigma^i_{\alpha\beta}\psi_\beta(x)$ is the electronic spin density, σ^i $(i = 1, 2, 3)$ denotes the Pauli matrices, $\delta n_{\rm s}^i = n_{\rm s}^i - \langle n_{\rm s}^i\rangle$ is the spin density fluctuation, $\Gamma_{\rm t}$ is the spin-triplet interaction amplitude, and $\int dx = \int d^3x \int_0^{1/T} d\tau$. In Eq. (5.4), S_0 denotes an action,

$$S_0[\bar{\psi},\psi] = \tilde{S}_0[\bar{\psi},\psi] + \int dx\, \mathbf{H}_0(\mathbf{x})\cdot\mathbf{n}_{\rm s}(x), \tag{5.5a}$$

where,

$$\mathbf{H}_0(\mathbf{x}) = \Gamma_{\rm t}\langle\mathbf{n}_{\rm s}(x)\rangle = \Gamma_{\rm t}\mathbf{m}(x) \tag{5.5b}$$

is proportional to the average magnetization $\mathbf{m}(\mathbf{x}) = \langle\mathbf{n}_{\rm s}(\mathbf{x})\rangle$. In the helimagnetic state,

$$\mathbf{H}_0(\mathbf{x}) = \lambda[\cos(\mathbf{q}\cdot\mathbf{x})\hat{\mathbf{x}} + \sin(\mathbf{q}\cdot\mathbf{x})\hat{\mathbf{y}}], \tag{5.5c}$$

where we will take the pitch vector $\mathbf{q}$ to point in the z-direction, $\mathbf{q} = q\hat{\mathbf{z}}$, and $\lambda = \Gamma_{\rm t} m_{sp}$ is the Stoner gap, with m_{sp} the helimagnetic amplitude. $\tilde{S}_0$ in Eq. (5.5a) contains the action for non-interacting band electrons plus, possibly, an interaction

in the spin-singlet channel. Finally, fluctuations of the helimagnetic order are taken into account by generalizing $\mathbf{H}_0$ to a fluctuating classical field $\mathbf{H}(x) = \Gamma_{\rm t}\mathbf{M}(x) = b\mathbf{H}_0 + \Gamma_{\rm t}\delta\mathbf{M}(x)$, where $\mathbf{M}(x)$ represents the spin density averaged over the quantum mechanical degrees of freedom. $\chi_{\rm s}^{ij}(x,y) = \langle \delta M_i(x)\delta M_j(y)\rangle$ in Eq. (5.4) is the magnetic susceptibility in the helimagnetic state, and the action (5.4) has been obtained by adding a part that governs the fluctuations $\delta\mathbf{M}$ to the electronic part, and then integrating out $\delta\mathbf{M}$.

The susceptibility $\chi_{\rm s}$ was calculated, [44] and is related to the Goldstone modes for helimagnetic phases in Eq. (4.22), or A phase in Eq. (4.12). For example, the helimagnon is given in terms of magnetization fluctuations that can be parameterized by

$$\delta M_x(x) = -m_{sp}\phi(x)\sin qz \tag{5.6a}$$

$$\delta M_y(x) = m_{sp}\phi(x)\cos qz. \tag{5.6b}$$

$\delta M_z = 0$ in an approximation that suffices to determine the leading behavior of observables. In Eqs. (5.6), ϕ is a phase variable. In Fourier space, the phase-phase correlation function in the long-wavelength and low-frequency limit is,

$$\chi(k) \equiv \langle \phi(k)\phi(-k)\rangle = \frac{1}{2N_{\rm F}}\frac{q^2}{3k_{\rm F}^2}\frac{1}{\omega_0^2(\mathbf{k}) - (i\Omega)^2}\ , \tag{5.7}$$

with $N_{\rm F}$ the electronic density of states per spin at the Fermi surface, $k_{\rm F}$ the Fermi wave number, [1] and $k = (\mathbf{k}, i\Omega)$. The bosonic Matsubara frequency is given by [94]

$$i\Omega \equiv i\Omega_n = i2\pi Tn, \tag{5.8}$$

[1] Due to the Stoner splitting, one strictly speaking has to distinguish between Fermi-surface properties, such as the Fermi wave number, the density of states at the Fermi surface etc., in

where $n = 0, \pm 1, \pm 2$, etc. The pole frequency is either Eqs. (4.22) or (4.12). For later reference, we also list its spectral function

$$\chi''(\mathbf{k}, u) = \mathrm{Im}\,\chi(\mathbf{k}, i\Omega \to u + i0) = \frac{\pi}{12 N_{\mathrm{F}}} \frac{q^2}{k_{\mathrm{F}}^2} \frac{1}{\omega_0(\mathbf{k})} \left[\delta(u - \omega_0(\mathbf{k})) - \delta(u + \omega_0(\mathbf{k}))\right]. \tag{5.9}$$

This specifies the action given in Eq. (5.4). In Fourier space, and neglecting any spin-singlet interaction, it can be written,

$$S_{\mathrm{eff}}[\bar{\psi}, \psi] = S_0[\bar{\psi}, \psi] + S_{\mathrm{int}}[\bar{\psi}, \psi], \tag{5.10a}$$

$$S_0[\bar{\psi}, \psi] = \sum_p (i\omega - \xi_{\mathbf{p}}) \sum_\sigma \bar{\psi}_\sigma(p)\psi_\sigma(p) + \lambda \sum_p \left[\bar{\psi}_\uparrow(p)\psi_\downarrow(p+q) + \bar{\psi}_\downarrow(p)\psi_\uparrow(p-q)\right], \tag{5.10b}$$

$$S_{\mathrm{int}}[\bar{\psi}, \psi] = -\frac{\lambda^2}{2} \frac{T}{V} \sum_k \chi(k) \left[\delta n_{\uparrow\downarrow}(k-q) - \delta n_{\downarrow\uparrow}(k+q)\right] \left[\delta n_{\uparrow\downarrow}(-k-q) - \delta n_{\downarrow\uparrow}(-k+q)\right], \tag{5.10c}$$

where V is the system volume, and

$$i\omega \equiv i\omega_n = i2\pi T \left(n + \frac{1}{2}\right), \tag{5.10d}$$

(where $n = 0, \pm 1, \pm 2, \ldots$) is a fermionic Matsubara frequency,

$$n_{\sigma_1\sigma_2}(k) = \sum_p \bar{\psi}_{\sigma_1}(p)\psi_{\sigma_2}(p-k), \tag{5.10e}$$

and

$$\delta n_{\sigma_1\sigma_2}(k) = n_{\sigma_1\sigma_2}(k) - \langle n_{\sigma_1\sigma_2}(k)\rangle. \tag{5.10f}$$

the two Stoner bands. For a weak helimagnet the differences between these quantities are small, and we will systematically neglect them. This amounts to working to lowest order in the small parameter $\frac{\lambda}{\epsilon_F}$.

Here $p = (\mathbf{p}, i\omega)$, and q denotes the four-vector $(\mathbf{q}, 0)$. In Eq. (5.10b), $\xi_{\mathbf{p}} = \epsilon_{\mathbf{p}} - \epsilon_F$, with ϵ_F the Fermi energy, and $\epsilon_{\mathbf{p}}$ the single-particle energy-momentum relation. The latter we will specify in Eq. (5.21) below.

In the above effective action, S_0 represents noninteracting electrons on the background of helimagnetic order that has been taken into account in a mean-field or Stoner approximation. Fluctuations of the helimagnets or columnar phase lead to an effective interaction between the electrons via an exchange of helimagnons or phonons in the columnar phase. This is reflected by the term S_{int}, and the effective potential is proportional to the susceptibility χ.

5.2.2 Canonical transformation to quasiparticle variables

The action S_0 in Eq. (5.10b) above is not diagonal in either the spin index or the wave number. A cursory inspection shows that by a suitable combination of the fermion fields it is possible to diagonalize S_0 in spin space. It is much less obvious that it is possible to find a transformation that simultaneously diagonalizes S_0 in wave number space. This makes the calculation of transport properties very complicated as in Ref. [93]. In what follows we construct such a transformation, i.e. we map the electronic helimagnon problem onto an equivalent problem in which space is homogeneous, according to the transformation scheme detailed in Ref. [95].

Let us define a canonical transformation of the electronic Grassmann fields $\bar{\psi}$

and ψ to new quasiparticle fields $\bar{\eta}$ and η, which also are Grassmann-valued, by

$$\bar{\psi}_\uparrow(p) = \frac{[\bar{\eta}_\uparrow(p) + \alpha_{\mathbf{p}}\,\bar{\eta}_\downarrow(p)]}{\sqrt{1+\alpha_{\mathbf{p}}^2}}, \tag{5.11a}$$

$$\bar{\psi}_\downarrow(p) = \frac{[\bar{\eta}_\downarrow(p-q) - \alpha_{\mathbf{p}-\mathbf{q}}\,\bar{\eta}_\uparrow(p-q)]}{\sqrt{1+\alpha_{\mathbf{p}-\mathbf{q}}^2}}, \tag{5.11b}$$

$$\psi_\uparrow(p) = \frac{[\eta_\uparrow(p) + \alpha_{\mathbf{p}}\eta_\downarrow(p)]}{\sqrt{1+\alpha_{\mathbf{p}}^2}}, \tag{5.11c}$$

$$\psi_\downarrow(p) = \frac{[\eta_\downarrow(p-q) - \alpha_{\mathbf{p}-\mathbf{q}}\eta_\uparrow(p-q)]}{\sqrt{1+\alpha_{\mathbf{p}-\mathbf{q}}^2}}. \tag{5.11d}$$

The coefficient $\alpha_{\mathbf{p}}$ is determined by inserting the Eqs. (5.11) into Eq. (5.10b) and requiring this noninteracting part of that action to be diagonal in the spin labels. This requirement can be fulfilled by choosing it to be real and frequency independent, and given by

$$\alpha_{\mathbf{p}} = \frac{1}{2\lambda}\left[\xi_{\mathbf{p}+\mathbf{q}} - \xi_{\mathbf{p}} + \sqrt{(\xi_{\mathbf{p}+\mathbf{q}} - \xi_{\mathbf{p}})^2 + 4\lambda^2}\right]. \tag{5.12}$$

The transformation of variables changes the path integration measure as follows:

$$\begin{aligned} D[\bar{\psi},\psi] &\equiv \prod_{p,\sigma} d\bar{\psi}_\sigma(p) d\psi_\sigma(p) \\ &= \prod_{p,\sigma} d\bar{\eta}_\sigma(p) d\eta_\sigma(p) = D[\bar{\eta},\eta], \end{aligned} \tag{5.13}$$

with Jacobian equal to unity. Then the partition function is given by

$$Z = \int D[\bar{\psi},\psi] e^{S_{\text{eff}}[\bar{\psi},\psi]} = \int D[\bar{\eta},\eta] e^{S_{\text{eff}}[\bar{\eta},\eta]}. \tag{5.14}$$

In terms of these new Grassmann fields the Jacobian is unity, and the noninteracting part of the action reads

$$S_0[\bar{\eta},\eta] = \sum_{p,\sigma} [i\omega - \omega_\sigma(\mathbf{p})]\,\bar{\eta}_\sigma(p)\eta_\sigma(p). \tag{5.15a}$$

Here $\sigma = (\uparrow, \downarrow) \equiv (1, 2)$, and

$$\omega_{1,2}(\mathbf{p}) = \frac{1}{2}\left[\xi_{\mathbf{p}+\mathbf{q}} + \xi_{\mathbf{p}} \pm \sqrt{(\xi_{\mathbf{p}+\mathbf{q}} - \xi_{\mathbf{p}})^2 + 4\lambda^2}\,\right]. \tag{5.15b}$$

The noninteracting quasiparticle Green function thus is

$$G_{0,\sigma}(p) = \frac{1}{i\omega - \omega_\sigma(\mathbf{p})}\ . \tag{5.15c}$$

Physically, the Eqs. (5.15) represent soft fermionic excitations about the two Fermi surfaces that result from the helimagnetism splitting the original band. This Gaussian action is diagonal in wave number space, so the quasiparticle system is homogeneous.

The interacting part of the action consist of two pieces. One contains terms that couple the two Fermi surfaces. Because there is an energy gap, namely, the Stoner gap λ, between these surfaces, these terms always lead to exponentially small contributions to the electronic properties at low temperatures, and will be neglected here. The second piece is, in terms of the quasiparticle fields,

$$S_{\rm int}[\bar\eta, \eta] = -\frac{\lambda^2 q^2}{8m_{\rm e}^2}\frac{T}{V}\sum_k \chi(k)\delta\rho(k)\delta\rho(-k). \tag{5.16a}$$

Here we have defined

$$\rho(k) = \sum_p \gamma(\mathbf{k}, \mathbf{p}) \sum_\sigma \bar\eta_\sigma(p)\eta_\sigma(p-k), \tag{5.16b}$$

with

$$\gamma(\mathbf{k}, \mathbf{p}) = \frac{2m_{\rm e}}{q}\frac{\alpha_{\mathbf{p}} - \alpha_{\mathbf{p}-\mathbf{k}}}{\sqrt{1+\alpha_{\mathbf{p}}^2}\sqrt{1+\alpha_{\mathbf{p}-\mathbf{k}}^2}}\ , \tag{5.16c}$$

where $m_{\rm e}$ is the electron effective mass, and

$$\delta\rho_\sigma(k) = \rho_\sigma(k) - \langle\rho_\sigma(k)\rangle. \tag{5.16d}$$

An important feature of this result is the vertex function $\gamma(\mathbf{k},\mathbf{p})$, which is proportional to $\mathbf{k}$ for $\mathbf{k}\to 0$. The physical significance is that ϕ is a phase, and hence only the gradient of ϕ is physically meaningful. Therefore, the ϕ-susceptibility χ must occur with a gradient squared in Eq. (5.16a). [2] Also note the wave number structure of the fermion fields in Eq. (5.16b), it the same as in a homogeneous problem.

5.2.3 Nonmagnetic disorder

In the presence of nonmagnetic disorder there is an additional term in the action. In terms of the original Grassmann variables, it reads

$$S_{\rm dis}[\bar\psi,\psi]=\int d^3x\sum_\sigma u(\mathbf{x})\bar\psi_\sigma(x)\psi_\sigma(x). \tag{5.17}$$

Here $u(\mathbf{x})$ is a random potential that we assume to be governed by a Gaussian distribution with a variance given by

$$\{u(\mathbf{x})\,u(\mathbf{y})\}_{\rm dis}=\frac{1}{2\pi N_{\rm F}\tau}\,\delta(\mathbf{x}-\mathbf{y}). \tag{5.18}$$

Here $\{\ldots\}_{\rm dis}$ denotes an average with respect to the Gaussian probability distribution function, and τ is the (bare) elastic mean-free time. Inserting the Eqs. (5.11) into Eq. (5.17) yields $S_{\rm dis}[\bar\eta,\eta]$. Ignoring terms that couple the two Fermi surfaces (which lead to exponentially small effects at low temperatures) yields

$$\begin{aligned} S_{\rm dis}[\bar\eta,\eta] &= \sum_{\mathbf{k},\mathbf{p}}\sum_{i\omega}\sum_\sigma \frac{1+\alpha_{\mathbf{k}}\alpha_{\mathbf{p}}}{\sqrt{(1+\alpha_{\mathbf{k}}^2)(1+\alpha_{\mathbf{p}}^2)}}u(\mathbf{k}-\mathbf{p}) \\ &\quad\times\bar\eta_\sigma(\mathbf{k},i\omega)\eta_\sigma(\mathbf{p},i\omega). \end{aligned} \tag{5.19}$$

[2] In the formalism of Ref. [93] this feature became apparent only after complicated cancellations; in the current formalism it is automatically built in.

5.2.4 Explicit quasiparticle action

So far we have been very general in our discussion. In order to perform explicit calculations, we need to specify certain aspects of our model. First of all, we make the following simplification. In most of our calculations below we will work in the limit where $\lambda \gg v_{\rm F} q = \frac{2\epsilon_F q}{k_{\rm F}}$ with $v_{\rm F}$ the Fermi velocity; i.e., the Stoner splitting of the Fermi surfaces is large compared to the Fermi energy times the ratio of the pitch wave number to the Fermi momentum. Since the dominant contributions to the observables will come from wave vectors on the Fermi surface, this implies that we can replace the transformation coefficients $\alpha_{\mathbf{p}}$, Eq. (5.12), by unity in Eq. (5.19), and in the denominator of Eq. (A.3d). In particular, this means that the disorder potential in Eq. (5.19) couples to the quasiparticle density:

$$S_{\rm dis}[\bar{\eta}, \eta] = \sum_{\mathbf{k},\mathbf{p}} u(\mathbf{k}-\mathbf{p}) \sum_{i\omega} \sum_{\sigma} \bar{\eta}_\sigma(\mathbf{k}, i\omega)\eta_\sigma(\mathbf{p}, i\omega). \tag{5.20}$$

Second, we must specify the electronic energy-momentum relation $\epsilon_{\mathbf{p}}$. Many of the electronic effects in metallic helimagnets are stronger when the underlying lattice and the resulting anisotropic energy-momentum relation is taken into account, as opposed to working within a nearly-free electron model. [93] We will assume a cubic lattice, as appropriate for helimagnets such as MnSi, so any terms consistent with cubic symmetry are allowed. To quartic order in $\mathbf{p}$ the most general $\epsilon_{\mathbf{p}}$ consistent with a cubic symmetry can be written

$$\epsilon_{\mathbf{p}} = \frac{\mathbf{p}^2}{2m_{\rm e}} + \frac{\nu}{2m_{\rm e}k_{\rm F}^2}(p_x^2 p_y^2 + p_y^2 p_z^2 + p_z^2 p_x^2), \tag{5.21}$$

with ν a dimensionless measure of deviations from a nearly-free electron model. Generically one expects $\nu = O(1)$. Other quartic terms that are consistent with a

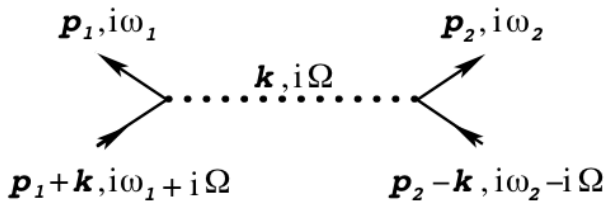

Figure 5.1: The effective quasiparticle interaction due to helimagnons.

cubic symmetry, e.g., the cubic anisotropy $k_x^4 + k_y^4 + k_z^4$ can be obtained by adding an isotropic $(\mathbf{k}^2)^2$ term to Eq. (5.21). Cases for $\nu = 0$ and $\nu \neq 0$ yield different temperature dependences for transport coefficients. [93]

With this model, and assuming $\lambda \gg q v_{\rm F}$, which is typically satisfied, given the weakness of the spin-orbit interaction, we obtain for the interaction part of the action from Eqs. (5.16)

$$\begin{aligned} S_{\rm int} &= -\frac{T}{V}\sum_{k,p_1,p_2} V(k;\mathbf{p}_1,\mathbf{p}_2)\sum_{\sigma_1}\left[\bar\eta_{\sigma_1}(p_1+k)\eta_{\sigma_1}(p_1) - \langle\bar\eta_{\sigma_1}(p_1+k)\eta_{\sigma_1}(p_1)\rangle\right] \\ &\quad\times\sum_{\sigma_2}\left[\bar\eta_{\sigma_2}(p_2-k)\eta_{\sigma_2}(p_2) - \langle\bar\eta_{\sigma_2}(p_2-k)\eta_{\sigma_2}(p_2)\rangle\right], \end{aligned} \tag{5.22}$$

where the effective potential is

$$V(k;\mathbf{p}_1,\mathbf{p}_2) = V_0\chi(k)\gamma(\mathbf{k},\mathbf{p}_1)\gamma(-\mathbf{k},\mathbf{p}_2). \tag{5.23a}$$

Here,

$$V_0 = \frac{\lambda^2 q^2}{8m_{\rm e}^2}, \tag{5.23b}$$

and,

$$\gamma(\mathbf{k},\mathbf{p}) = \frac{1}{2\lambda}\left[k_z + \frac{\nu}{k_{\rm F}^2}\left(k_z\mathbf{p}_\perp^2 + 2(\mathbf{k}_\perp\cdot\mathbf{p}_\perp)p_z\right)\right] + O(k^2). \tag{5.23c}$$

The effective interaction is depicted diagrammtically in Fig. 5.1.

Examining the Eqs. (5.22) and (5.23), we see two important features. First, the effective potential is indeed proportional to $\mathbf{k}^2\chi(k)$. As was mentioned after Eq. (5.16d), this is required for a phase fluctuation effect. Second, the effective interaction is long-ranged, due to the singular nature of the susceptibility $\chi(k)$ at long wave lengths and low frequencies, see Eq. (5.7). This is a consequence of the soft mode, the helimagnon, that mediates the interaction.

In summary, we now have the following quasiparticle action:

$$S_{\rm QP}[\bar{\eta},\eta] = S_0[\bar{\eta},\eta] + S_{\rm int}[\bar{\eta},\eta] + S_{\rm dis}[\bar{\eta},\eta], \tag{5.24a}$$

with S_0 from Eqs. (5.15), $S_{\rm int}$ from Eqs. (5.22) and (5.23), and $S_{\rm dis}$ given by Eq. (5.20). The partition function is given by

$$Z = \int D[\bar{\eta},\eta]\, e^{S_{\rm QP}[\bar{\eta},\eta]}, \tag{5.24b}$$

with a canonical measure

$$D[\bar{\eta},\eta] = \prod_{p,\sigma} d\bar{\eta}_\sigma(p) d\eta_\sigma(p). \tag{5.24c}$$

5.2.5 Screening of the quasiparticle interaction

The quasiparticle interaction potential shown in Eqs. (5.23) must be screened, and an important question is whether this will change its long-ranged nature. In the usual ladder or random-phase approximation the screened potential $V_{\rm sc}$ is determined by an integral equation that is shown graphically as, like Dyson's equation,

[94]

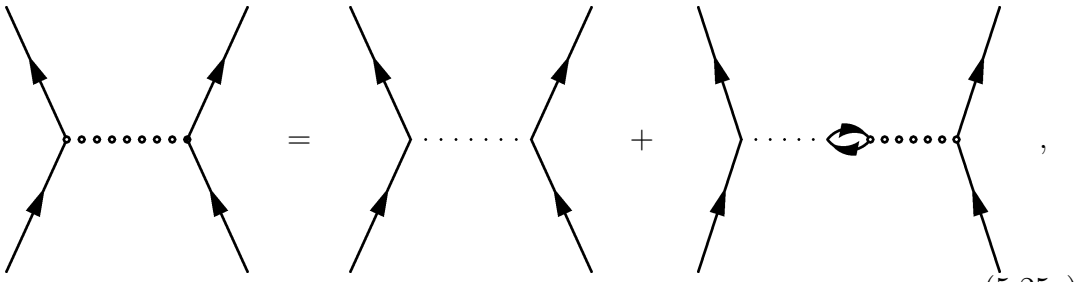

(5.25a)

and analytically given by

$$V_{\rm sc}(k;\mathbf{p}_1,\mathbf{p}_2) = V(k;\mathbf{p}_1,\mathbf{p}_2) + \frac{T}{V}\sum_{p_3} V(k;\mathbf{p}_1,\mathbf{p}_3)\sum_{\sigma} G_{0,\sigma}(p_3-k)G_{0,\sigma}(p_3)V_{\rm sc}(k;\mathbf{p}_3,\mathbf{p}_2). \tag{5.25b}$$

It is convenient to define a screening factor $f_{\rm sc}$ by writing

$$V_{\rm sc}(k;\mathbf{p}_1,\mathbf{p}_2) = V(k;\mathbf{p}_1,\mathbf{p}_2) f_{\rm sc}(k;\mathbf{p}_1,\mathbf{p}_2). \tag{5.26}$$

Inserting Eq. (5.26) in Eq. (5.25b) leads to an algebraic equation for $f_{\rm sc}$ with a solution

$$f_{\rm sc}(k;\mathbf{p}_1,\mathbf{p}_2) = \frac{1}{1 - V_0 \frac{1}{V}\sum_{\mathbf{p}} \gamma(\mathbf{k},\mathbf{p})\gamma(-\mathbf{k},\mathbf{p})\chi_{\rm L}(\mathbf{p},i\Omega)}, \tag{5.27a}$$

where

$$\chi_{\rm L}(\mathbf{p},i\Omega) = -T\sum_{i\omega}\sum_{\sigma} G_{0,\sigma}(\mathbf{p},i\omega)G_{0,\sigma}(\mathbf{p},i\omega - i\Omega). \tag{5.27b}$$

The most interesting effect of the screening is at $k \to 0$, and therefore we need to consider only $\chi_{\rm L}(\mathbf{p}, i\Omega = i0) \equiv \chi_{\rm L}(\mathbf{p})$. This is essentially the Lindhard function, [96] and we use the approximation $\frac{1}{V}\sum_{\mathbf{p}} |\mathbf{p}|^n \chi_{\rm L}(\mathbf{p}) \approx k_{\rm F}^n N_{\rm F}$. Neglecting prefactors of $O(1)$ this yields

$$\frac{1}{V}\sum_{\mathbf{p}} \gamma(\mathbf{k},\mathbf{p})\,\gamma(-\mathbf{k},\mathbf{p})\chi_{\rm L}(\mathbf{p}) \approx \frac{N_{\rm F}}{4\lambda^2}\left[(1+\nu)^2 k_z^2 + \nu^2 \mathbf{k}_\perp^2\right].$$

We finally obtain

$$V_{\rm sc}(k;\mathbf{p}_1,\mathbf{p}_2) = V_0\chi_{\rm sc}(k)\gamma(\mathbf{k},\mathbf{p}_1)\gamma(-\mathbf{k},\mathbf{p}_2), \tag{5.28a}$$

where

$$\chi_{\rm sc}(k) = \frac{1}{2N_{\rm F}}\frac{q^2}{3k_{\rm F}^2}\frac{1}{\tilde{\omega}_0^2(\mathbf{k})-(i\Omega)^2}. \tag{5.28b}$$

Here for pure helimagnons,

$$\tilde{\omega}_0^2(\mathbf{k}) = \tilde{c}_z k_z^2 + V_0\frac{\nu^2}{24}\frac{q^2}{k_{\rm F}^2\lambda^2}\mathbf{k}_\perp^2 + c_\perp\mathbf{k}_\perp^4, \tag{5.28c}$$

with

$$\tilde{c}_z = c_z\left[1+\frac{q^2}{k_{\rm F}^2}\left(\frac{\epsilon_{\rm F}}{\lambda}\right)^2\right], \tag{5.28d}$$

where [44, 95]

$$c_z = \lambda^2\frac{q^2}{36}k_{\rm F}^4, \tag{5.28e}$$

$$c_\perp = \frac{\lambda^2}{96}k_{\rm F}^4. \tag{5.28f}$$

We see that the screening has two effects on the frequency $\tilde{\omega}_0$ that enters the screened potential instead of the helimagnon frequency ω_0. First, it renormalizes the elastic constant c_z by a term of order $\left(\frac{q}{k_{\rm F}}\right)^2(\frac{\epsilon_{\rm F}}{\lambda})^2$. This is a small effect as long as $qv_{\rm F} \ll \lambda$. Second, it leads to a term proportional to $\mathbf{k}_\perp^2$ in $\tilde{\omega}_0^2$. Such a term also exists in the helimagnon frequency proper, since the cubic lattice in conjunction with spin-orbit effects breaks the rotational symmetry that is responsible for the absence of a $\mathbf{k}_\perp^2$ term in ω_0, and it is of order $\frac{bc_zq^2\mathbf{k}_\perp^2}{k_{\rm F}^2}$, with $b = 0(1)$. The complete expression for $\tilde{\omega}_0^2$ is thus given by

$$\tilde{\omega}_0^2(\mathbf{k}) = \tilde{c}_z k_z^2 + \tilde{b}c_z\left(\frac{q}{k_{\rm F}}\right)^2\mathbf{k}_\perp^2 + c_\perp\mathbf{k}_\perp^4, \tag{5.29a}$$

with

$$\tilde{b} = b + (\epsilon_{\rm F}/\lambda)^2. \tag{5.29b}$$

This puts a lower limit on the temperature range where the isotropic helimagnon description is valid. In the absence of screening, this lower limit is given by

$$T > T_{\rm so} = b\lambda \left(\frac{q}{k_{\rm F}}\right)^4. \tag{5.30a}$$

This lower limit reflects the spin-orbit interaction effects that break the rotational symmetry, and it is small of order $(q/k_{\rm F})^4$. Screening changes this condition to

$$T > \tilde{T}_{\rm so} = \tilde{b}\lambda \left(\frac{q}{k_{\rm F}}\right)^4, \tag{5.30b}$$

which is still small provided $qv_{\rm F} \ll \lambda$. We will therefore ignore the screening in the remainder of this thesis.

Similar argument for the negligence of quasiparticle screening holds for the columnar phase.

5.3 Transport properties of a clean helimagnet

5.3.1 Single particle relaxation rates

In this section, we determine the single-particle relaxation rate due to interactions in conical phase and columnar phase, and its modification due to disorder in ballistic limit.

To this end we calculate the quasiparticle self energy for an action $S_0 + S_{\rm int}$ from Eqs. (5.15a), (5.22) and (5.23c). To first order in the interaction there are two

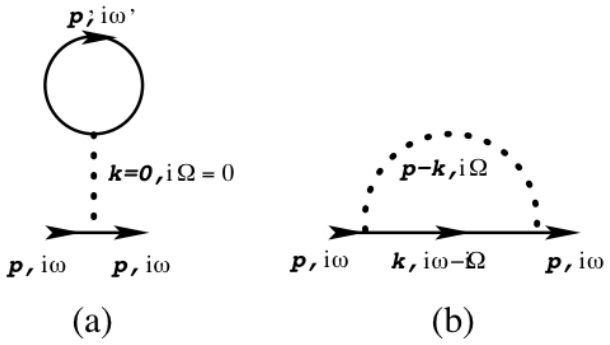

Figure 5.2: Hartree (a), and Fock (b), contributions to the quasiparticle self energy due to the effective interaction potential V (dotted line).

self-energy diagrams are shown in Fig. 5.2. The direct or Hartree contribution, in Fig. 5.2(a), is purely real and hence does not contribute to the scattering rate. The exchange or Fock contribution, in Fig. 5.2(b), is given by

$$\Sigma_\sigma(p) = -\frac{T}{V}\sum_k V(k;\mathbf{p}-\mathbf{k},\mathbf{p})G_{0,\sigma}(k-p). \tag{5.31}$$

We consider the Fermi surface given by $\omega_1(\mathbf{p}) = 0$, with $\omega_1(\mathbf{p})$ given in Eq. (5.15b). The single-particle relaxation rate is given by $\frac{1}{\tau(\mathbf{k},\epsilon)} = -2\mathrm{Im}\,\Sigma_1(\mathbf{k},\epsilon+i0)$. With Eqs. (5.15c) and (5.23) in Eq. (5.31), we find

$$\frac{1}{\tau(\mathbf{k},\epsilon)} = 2\int_{-\infty}^{\infty} du \sum_{\mathbf{p}} \left[n_{\mathrm{B}}\left(\frac{u}{T}\right) + n_{\mathrm{F}}\left(\frac{\epsilon+u}{T}\right)\right] V''(\mathbf{p}-\mathbf{k};\mathbf{k},\mathbf{p};u)\delta(\epsilon+u-\omega_1(\mathbf{p})). \tag{5.32}$$

Here

$$n_{\mathrm{B}}(x) = \frac{1}{e^x-1}, \tag{5.33a}$$

$$n_{\mathrm{F}}(x) = \frac{1}{e^x+1}, \tag{5.33b}$$

are the Bose and Fermi distribution functions, respectively, and $V''(\mathbf{k};\mathbf{p}_1,\mathbf{p}_2;u) = \mathrm{Im}\,V(k=(\mathbf{k},i\Omega\to u+i0);\mathbf{p}_1\,\mathbf{p}_2)$ is the spectrum of the potential. [97] To find the

relaxation rate, we calculate

$$\frac{1}{\tau(\mathbf{k})} \equiv \frac{1}{\tau(\mathbf{k}, \epsilon = 0)}, \tag{5.34}$$

where $\epsilon = 0$ and $\omega_1(\mathbf{k}) = 0$ on the Fermi surface.

The single-particle relaxation rate, and hence the thermal conductivity, will be calculated in Section 5.3.3.

5.3.2 Electrical conductivity

In this section, we set up a standard technical formalism for transport theory in the context of the effective model for metallic helimagnets. The electrical conductivity tensor σ_{ij} can be expressed in terms of an equilibrium current-current correlation function by means of the Kubo formula

$$\sigma_{ij}(i\Omega) = \frac{i}{i\Omega} \left[\pi_{ij}(i\Omega) - \pi_{ij}(i\Omega = 0) \right], \tag{5.35a}$$

where

$$\begin{aligned} \pi_{ij}(i\Omega) &= -e^2 T \sum_{i\omega_1, i\omega_2} \frac{1}{V} \sum_{\mathbf{p}_1, \mathbf{p}_2} j_i(\mathbf{p}_1) j_j(\mathbf{p}_2) \\ &\quad \times \sum_{\sigma_1, \sigma_2} \langle \bar{\eta}_{\sigma_1}(\mathbf{p}_1, i\omega_1) \eta_{\sigma_1}(\mathbf{p}_1, i\omega_1 + i\Omega) \bar{\eta}_{\sigma_2}(\mathbf{p}_2, i\omega_2) \eta_{\sigma_2}(\mathbf{p}_2, i\omega_2 - i\Omega) \rangle, \end{aligned} \tag{5.35b}$$

is the current-current susceptibility or polarization function, with $\bar{\eta}$ and η the fermionic fields. $\langle \ldots \rangle$ denotes an average with respect to the action in Eqs. (5.24). For simplicity we suppress the index n. And

$$j(\mathbf{p}) = \frac{\partial \epsilon_{\mathbf{p}}}{\partial \mathbf{p}}, \tag{5.36}$$

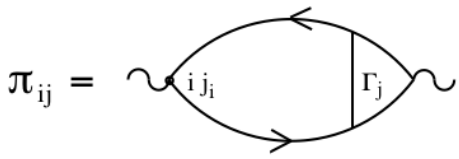

Figure 5.3: Graphical representation of the polarization function. The directed solid lines denote Green functions.

is the current vertex. The conductivity here is actually the transport coefficient for the quasiparticles described by the fermionic fields $\bar{\eta}$ and η. The physical conductivity is given in terms of the electron fields $\bar{\psi}$ and ψ, which are related to the quasiparticle fields by the transformation given in Eqs. (5.11). However, we will work to lowest order in the small parameter $\frac{q}{k_{\rm F}}$, [3] and to this accuracy the quasiparticle conductivity is the same as the physical conductivity, as can readily be seen from Eqs. (5.11).

The four-point fermionic correlation function in Eq. (5.35b) is conveniently expressed in terms of Green functions $\mathcal{G}$ and a vector vertex function $\mathbf{\Gamma}$ with components Γ^i,

$$\pi_{ij}(i\Omega) \;=\; -e^2 T \sum_{i\omega} \frac{1}{V} \sum_{\sigma} i j_i(\mathbf{p}) \mathcal{G}_\sigma(\mathbf{p}, i\omega) \mathcal{G}_\sigma(\mathbf{p}, i\omega - i\Omega) \Gamma^j_\sigma(\mathbf{p}; i\omega, i\omega - i\Omega), \tag{5.37}$$

see Fig. 5.3. This expression is valid if the Green function $\langle \eta_{\sigma_1}(\mathbf{p}_1, i\omega_1) \bar{\eta}_{\sigma_2}(\mathbf{p}_2, i\omega_2) \rangle$ is diagonal in both momentum and spin. For the effective model here, this is the case (whereas it was not the case in Ref. [93]), and $\mathcal{G}$ is expressed in terms of the

[3] For long-wavelength helimagnets, q is small compared to $k_{\rm F}$. For MnSi, $q = 0.035$ Å^{-1} and $k_{\rm F} = 1.45$ Å^{-1}. Hence $\frac{q}{k_{\rm F}} \approx 0.02 \ll 1$.

self energy Σ by means of the usual Dyson equation

$$\mathcal{G}_\sigma(\mathbf{p}, i\omega) = \frac{1}{G_{0,\sigma}^{-1}(\mathbf{p}, i\omega) - \Sigma_\sigma(\mathbf{p}, i\omega)}. \tag{5.38}$$

Here G_0 is the bare Green function by Eq. (5.15c). Eqs. (5.37) and (5.38) just shift the problem into the determination of the self energy Σ and the vertex function $\mathbf{\Gamma}$.

In the clean limit, it is well known that care must be taken to treat the self energy Σ, which enters the Green function $\mathcal{G}$, and the vertex function $\mathbf{\Gamma}$ consistently in a conserving approximation. [98] The simplest consistent approximation, which is equivalent to the Boltzmann equation, is to treat the self energy in a self-consistent Born approximation, and the vertex function in a ladder approximation. [99] The self energy is given by the Schwinger-Dyson equation in Eq. (5.31), and

$$\begin{aligned} & \mathbf{\Gamma}_\sigma(\mathbf{p}; i\omega, i\omega - i\Omega) \\ = \; & i\mathbf{j}(\mathbf{p}) - \frac{1}{V}\sum_{\mathbf{k}} T \sum_{i\Omega'} V(\mathbf{k}; \mathbf{p}-\mathbf{k}, \mathbf{p}; i\Omega') \mathcal{G}_\sigma(\mathbf{p}-\mathbf{k}, i\omega - i\Omega') \mathcal{G}_\sigma(\mathbf{p}-\mathbf{k}, i\omega - i\Omega' - i\Omega) \\ & \qquad \times \mathbf{\Gamma}_\sigma(\mathbf{p}-\mathbf{k}; i\omega - i\Omega', i\omega - i\Omega' - i\Omega), \end{aligned} \tag{5.39}$$

which is the Bethe-Salpeter equation, for the vertex function. In what follows, we consider the contribution from the pole $\omega_1(\mathbf{p})$ and drop the spin label elsewhere. In the end, the contribution from the pole $\omega_2(\mathbf{p})$ can simply be added.

If we define a scalar vertex function γ by $\mathbf{\Gamma}(\mathbf{p}; i\omega, i\omega - i\Omega) = i\mathbf{j}(\mathbf{p})\gamma(\mathbf{p}; i\omega, i\omega - i\Omega)$, we find that γ obeys an integral equation

$$\begin{aligned} \gamma(\mathbf{p}; i\omega, i\omega - i\Omega) \; = \; & 1 - \frac{1}{V}\sum_{\mathbf{k}} T \sum_{i\Omega'} \frac{\mathbf{j}(\mathbf{p}) \cdot \mathbf{j}(\mathbf{p}-\mathbf{k})}{\mathbf{j}^2(\mathbf{p})} V(\mathbf{k}; \mathbf{p}-\mathbf{k}, \mathbf{p}; i\Omega') \\ & \times \mathcal{G}(\mathbf{p}-\mathbf{k}, i\omega - i\Omega') \mathcal{G}(\mathbf{p}-\mathbf{k}, i\omega - i\Omega' - i\Omega) \\ & \times \gamma(\mathbf{p}-\mathbf{k}; i\omega - i\Omega', i\omega - i\Omega' - i\Omega). \end{aligned} \tag{5.40}$$

The polarization function and conductivity tensors are diagonal, $\sigma_{ij}(i\Omega) = \delta_{ij}\,\sigma(i\Omega)$. The sum over fermionic Matsubara frequencies in Eq. (5.40) can be transformed into an integral along the real axis by standard methods. This procedure yields two terms where the frequency arguments of the Green functions lie on the same side of the real axis, and two other terms where they lie on opposite sides. Only the latter contribute to the leading result as the self energy goes to zero. Since the real part of the self energy just renormalizes the Fermi energy, and the imaginary part, which gives the relaxation rate, indeed goes to zero as $T \to 0$, we need to keep only these retarded-advanced combinations for the purpose of determining the leading low-temperature dependence of the conductivity. The Kubo formula for the static conductivity $\sigma = \lim_{\Omega\to 0} \mathrm{Re}\,\sigma(i\Omega \to \Omega + i0)$ becomes

$$\sigma = \frac{e^2}{3\pi}\int_{-\infty}^{\infty}\frac{d\epsilon}{4T}\frac{1}{\cosh^2\left(\frac{\epsilon}{2T}\right)}\frac{1}{V}\sum_{\mathbf{p}}\left(\mathbf{j}(\mathbf{p})\right)^2\left|\mathcal{G}(\mathbf{p},\epsilon+i0)\right|^2\gamma(\mathbf{p};\epsilon+i0,\epsilon-i0). \quad (5.41)$$

The Green functions in Eq. (5.41) ensure that the dominant contribution to the sum over wave vectors in the limit of a vanishing self energy comes from $\mathbf{p}$ such that $\xi_{\mathbf{p}} = \epsilon$. Furthermore, since ϵ scales with T, for the leading temperature dependence we can neglect all ϵ-dependencies that do not occur in the form $\frac{\epsilon}{T}$. In a nearly-free electron model, with a spherical Fermi surface with Fermi wave number k_{F}, and $\mathbf{j}(\mathbf{p}) = \frac{\mathbf{p}}{m_{\mathrm{e}}}$ with m_{e} the effective electron mass, we thus have

$$\sigma = \frac{e^2 k_{\mathrm{F}}^2}{3m_{\mathrm{e}}^2}\int_{-\infty}^{\infty}\frac{d\epsilon}{4T}\frac{1}{\cosh^2\left(\frac{\epsilon}{2T}\right)}\frac{\Lambda(\epsilon)}{\Gamma_0(\epsilon)}. \quad (5.42a)$$

Here we have defined

$$\Lambda(\epsilon) \equiv \frac{1}{V}\sum_{\mathbf{p}} \delta(\xi_{\mathbf{p}})\gamma(\mathbf{p};\epsilon+i0,\epsilon-i0), \tag{5.42b}$$

$$\Gamma_0(\epsilon) \equiv -\frac{1}{V}\sum_{\mathbf{p}} \delta(\xi_{\mathbf{p}})\mathrm{Im}\,\Sigma(\mathbf{p},\epsilon+i0), \tag{5.42c}$$

and we neglect the real part of the self energy, which only redefines the zero of energy.

Using analogous arguments, we find from Eq. (5.40) that Λ obeys an integral equation

$$\Lambda(\epsilon) = 1 - N_{\mathrm{F}} \int du \bar{V}''(u) \left[n_{\mathrm{B}}\left(\frac{u}{T}\right) + n_{\mathrm{F}}\left(\frac{\epsilon+u}{T}\right)\right] \frac{\Lambda(\epsilon+u)}{\Gamma_0(\epsilon+u)}. \tag{5.43}$$

Here

$$\bar{V}''(u) = \frac{1}{S_{\mathrm{F}}^2}\frac{1}{V^2}\sum_{\mathbf{k},\mathbf{p}} \delta(\xi_{\mathbf{k}})\delta(\xi_{\mathbf{p}})V''(\mathbf{k}-\mathbf{p};\mathbf{k},\mathbf{p};u)\frac{\mathbf{k}\cdot\mathbf{p}}{k^2} \tag{5.44a}$$

with $S_{\mathrm{F}} = \frac{1}{V}\sum_{\mathbf{k}} \delta(\xi_{\mathbf{k}})$, is an $l = 1$ average of the spectrum of the potential over the Fermi surface. For the purpose of finding the leading temperature dependence of the conductivity, it can be written

$$\bar{V}''(u) = \bar{V}_0''(u) - \bar{V}_1''(u), \tag{5.44b}$$

with

$$\bar{V}_n''(u) = \frac{1}{2k_{\mathrm{F}}^2}\int_0^{2k_{\mathrm{F}}} dp\, p \left(p^2/2k_{\mathrm{F}}^2\right)^n V''(p,u). \tag{5.44c}$$

The integral equation in Eq. (5.43) is not easy to solve. However, in an approximation that replaces $\frac{\Lambda(\epsilon+u)}{\Gamma_0(\epsilon+u)}$ under the integral by $\frac{\Lambda(\epsilon)}{\Gamma_0(\epsilon)}$, [4] it turns into an

[4]Details of the analysis can be found in Ref. [100], which discusses the structure of the integral equation for the vertex function $\Lambda(\epsilon)$ in Eq. (5.43). It was shown that it leads to the

algebraic equation whose solution is

$$\Lambda(\epsilon) = \frac{\Gamma_0(\epsilon)}{\Gamma_1(\epsilon)}, \tag{5.45a}$$

Here we have used the fact that, in the limit of a small self energy, one find from Eqs. (5.42c) and (5.31),

$$\Gamma_0(\epsilon) = -N_{\rm F} \int du\, \bar{V}_0''(u) \left[n_{\rm B}\left(\frac{u}{T}\right) + n_{\rm F}\left(\frac{\epsilon+u}{T}\right)\right], \tag{5.45b}$$

and we have defined

$$\Gamma_1(\epsilon) = -N_{\rm F} \int du\, \bar{V}_1''(u) \left[n_{\rm B}\left(\frac{u}{T}\right) + n_{\rm F}\left(\frac{\epsilon+u}{T}\right)\right]. \tag{5.45c}$$

We see that the vertex function Λ effective replaces the single-particle relaxation rate Γ with the transport relaxation rate Γ_1. To see the relation between the two, we recall that the frequency u scales with the temperature. For potentials where the frequency scales with some (positive) power of the wave number, Γ_1 will thus depend on a higher power of the temperature as $T \to 0$ than Γ. [5] It has to be stressed that the approximate solution, Eq. (5.45a), of the integral equation, Eq.

same temperature dependence of conductivity derived from the Boltzmann equation in the case of electron-phonon interaction (i.e., the Block-Grüneisen law). For helimagnon case, it also leads to the same temperature dependences in Ref. [93].

[5] As an example, consider the case of electron scattering by acoustic phonons, where $V''(p,u) \propto cp\,[\delta(u-cp) - \delta(u+cp)]$, with c the speed of sound. In this case, $\Gamma_0(\epsilon) \propto T^3\,\gamma_0(\epsilon/T)$, whereas $\Gamma_1(\epsilon) \propto T^5\,\gamma_1(\epsilon/T)$, where

$$\gamma_n(y) = \int_0^\infty dx\, x^{2(n+1)}\,[2n_{\rm B}(x) + n_{\rm F}(x+y) + n_{\rm F}(x-y)]\,. \tag{5.46}$$

In this case, the single-particle scattering rate shows a T^3 dependence, whereas the transport scattering rate, and hence the resistivity, display the familiar Bloch-Grüneisen law, $\sigma \propto T^5$. [99]

(5.43), yields the asymptotically exact temperature dependence (although not the prefactor) of the conductivity. It can been seen from the fact that the asymptotic solution reproduces the lowest-order variational solution of the Boltzmann equation. [101]

5.3.3 Summary of transport properties of a clean helimagnet

With the microscopic model developed from Section 5.2, the temperature dependence of the single-particle relaxation rate, as well as that of the electrical transport relaxation rate or the electrical resistivity, can be obtained. The single-particle relaxation rate is given by putting $\epsilon = 0$ (Fermi surface) in Eq. (5.32),

$$\frac{1}{\tau(\mathbf{k})} = 2\int_{-\infty}^{\infty} \frac{du}{\sinh\frac{u}{T}} \frac{1}{V}\sum_{\mathbf{p}} V''(\mathbf{p}-\mathbf{k};\mathbf{k},\mathbf{p};u)\delta(u-\omega_1(\mathbf{p})), \tag{5.47}$$

where the scattering potential $V''(\mathbf{p}-\mathbf{k};\mathbf{k},\mathbf{p};u)$ is given by Eq. (5.23). On the other hand, the electrical transport relaxation time, which determines the electrical resistivity, is effectively given by averaging a similar expression over the Fermi surface,

$$\frac{1}{\tau_{\mathrm{el}}^{tr}} = \frac{1}{N_{\mathrm{F}}}\int_{-\infty}^{\infty} \frac{du}{\sinh\frac{u}{T}} \frac{1}{V^2}\sum_{\mathbf{p},\mathbf{k}} \frac{(\mathbf{p}-\mathbf{k})^2}{k_{\mathrm{F}}^2} V''(\mathbf{p}-\mathbf{k};\mathbf{k},\mathbf{p};u)\delta(u-\omega_1(\mathbf{p}))\delta(\omega_1(\mathbf{k})). \tag{5.48}$$

We can compare this with the transport rate in Eq. (5.45c). Note the additional, compared to Eq. (5.47), factor of $(\mathbf{p}-\mathbf{k})^2$ under the integral in Eq. (5.48). This is characteristic of the description of electrical transport in a Boltzmann approximation and leads to a temperature dependence of the electrical resistivity that is different from that of the single-particle relaxation rate. [101, 102] In contrast, in

a Boltzmann description of thermal transport this additional factor is absent, and the temperature dependence of the thermal conductivity is given by that of the single-particle relaxation rate. [102]

For a non-spherical Fermi surface (i.e., $\nu \neq 0$ in Eq. (5.21)), and for generic wave vectors $\mathbf{k}$, the temperature scaling behavior of the single-particle relaxation rate $1/\tau \equiv 1/\tau(\mathbf{k})$, the thermal resistivity $\rho_{\rm th}$, and the electrical resistivity $\rho_{\rm el}$ can be represented schematically by the expressions

$$\frac{1}{\tau} \sim \rho_{\rm th} \sim \int dp_{||} \int d\mathbf{p}_{\perp}^2 \, \frac{\mathbf{p}_{\perp}^2 + p_{||}^2}{\sinh \frac{\omega_0(\mathbf{p})}{T}} \frac{\delta(\omega_0(\mathbf{p}) - p_{\perp} - p_{||})}{\omega_0(\mathbf{p})} \, . \tag{5.49a}$$

$$\rho_{\rm el} \sim \int dp_{||} \int d\mathbf{p}_{\perp}^2 \, \frac{(\mathbf{p}_{\perp}^2 + p_{||}^2)^2}{\sinh \frac{\omega_0(\mathbf{p})}{T}} \frac{\delta(\omega_0(\mathbf{p}) - p_{\perp} - p_{||})}{\omega_0(\mathbf{p})} \, . \tag{5.49b}$$

The resonance frequency always scales as the temperature, $\omega_0 \sim T$, and the temperature dependence of the relaxation rates thus is determined by how the momentum components scale with temperature.

5.3.3.1 Generalized helimagnons

For the helical and conical phases we have, from Eq. (4.22), $p_{||} \sim T$, and $p_{\perp} \sim T$ and $\sim T^{1/2}$ at asymptotically low and intermediate temperatures, respectively. This yields the following temperature dependence for the single-particle relaxation rate and the thermal resistivity:

$$\frac{1}{\tau} \propto \rho_{\rm th} \propto \begin{cases} T^3 & \text{if } T \ll \frac{\tilde{c}_{\perp}}{\sqrt{c_{\perp}}} \\ T^{3/2} & \text{if } T \gg \frac{\tilde{c}_{\perp}}{\sqrt{c_{\perp}}} \end{cases} \, . \tag{5.50}$$

The corresponding result for the electrical resistivity is

$$\rho_{\rm el} \propto \begin{cases} T^5 & \text{if } T \ll \frac{\tilde{c}_\perp}{\sqrt{c_\perp}} \\ T^{5/2} & \text{if } T \gg \frac{\tilde{c}_\perp}{\sqrt{c_\perp}} \end{cases} . \tag{5.51}$$

In a vanishing external field, and in a temperature regime where pinning effects are not relevant, we recover the $T^{3/2}$ and $T^{5/2}$ behavior for $1/\tau$ and $\rho_{\rm el}$, respectively, of Refs. [93] and [103].

5.3.3.2 Columnar phase

For the columnar phase, we obtain by using Eq. (4.12)

$$\frac{1}{\tau} \propto \rho_{\rm th} \propto \begin{cases} T^3 & \text{if } T \ll \frac{c_z'}{\sqrt{c_z}} \\ T^2 & \text{if } T \gg \frac{c_z'}{\sqrt{c_z}} \end{cases} . \tag{5.52}$$

for the single-particle relaxation rate, and

$$\rho_{\rm el} \propto \begin{cases} T^5 & \text{if } T \ll \frac{c_z'}{\sqrt{c_z}} \\ T^3 & \text{if } T \gg \frac{c_z'}{\sqrt{c_z}} \end{cases} . \tag{5.53}$$

for the electrical resistivity.

5.4 Systems with quenched disorder

The preceding results hold for clean systems. In the presence of quenched disorder, elastic scattering of the conduction electrons leads to profound effects that manifest themselves in the transport properties. In this section, we evaluate the leading corrections of disordered to the transport properties.

One needs to distinguish between the strong-disorder regime, where the transport is diffusive, and the weak-disorder regime, where it is ballistic. In a Fermi liquid, these two regimes are characterized by $T\tau \ll 1$ and $T\tau \gg 1$, respectively. [104] In the diffusive limit, it is well known that an infinite resummation of impurity diagrams is needed to work to a given order in the disorder. In the ballistic limit, this is not the case, and a straightforward diagrammatic perturbative expansion in the number of impurity lines is possible. This yields impurity corrections to the clean conductivity. In a helical magnet, the weak-disorder or ballistic regime is characterized by [95, 103]

$$\sqrt{\frac{(\epsilon_{\mathrm{F}}\tau_{\mathrm{el}})^2 T}{\lambda}} \gg 1, \tag{5.54}$$

where τ_{el} is the elastic relaxation time, which enters the disordered average Green function in the following section.

5.4.1 Elastic relaxation time

Helimagnetism modifies the elastic scattering rate, even in the absence of interaction effects. To see this we calculate the quasiparticle self energy from the action $S_0 + S_{\mathrm{dis}}$ from Eqs. (5.15a) and (5.17). To first order in the disorder the relevant diagram is given by the diagram in Fig. 5.4. Analytically it is given by,

$$\Sigma^{el}_{\sigma}(\mathbf{p}, i\omega) = -\frac{1}{8\pi N_{\mathrm{F}}\tau}\frac{1}{V}\sum_{\mathbf{k}}[1 + \alpha_{\mathbf{p}}\alpha_{\mathbf{k}}]^2 G_{0,\sigma}(\mathbf{k}, i\omega), \tag{5.55}$$

with G_0 the noninteracting Green function from Eq. (5.15c). For simplicity we put $\nu = 0$ in Eq. (5.21), i.e., we consider nearly free electrons. In the limit $qv_{\mathrm{F}} \ll \lambda$ we

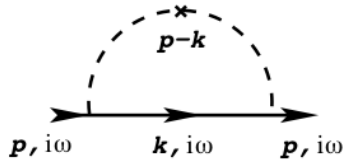

Figure 5.4: Quasiparticle self energy due to weak disorder. The directed solid line denotes the Green function, the dashed lines denote the disorder potential, and the cross denotes the disorder average.

obtain for the elastic scattering rate, $\frac{1}{\tau_{\rm el}} = -2{\rm Im}\,\Sigma_\sigma(\mathbf{p}, i0)$,

$$\frac{1}{\tau_{\rm el}} = \frac{1}{\tau}\sqrt{1 - \frac{\lambda}{\epsilon_{\rm F}}}, \tag{5.56a}$$

In the opposite limit, $qv_{\rm F} \gg \lambda$, we find

$$\frac{1}{\tau_{\rm el}} = \frac{1}{4\tau}\left[1 - \frac{q}{2k_{\rm F}} + O\left(\frac{q}{k_{\rm F}}\right)^2\right]. \tag{5.56b}$$

To first order in the disorder and to zeroth order in interactions, the disorder averaged Green function is [105]

$$G_\sigma(p) = \frac{1}{i\omega - \omega_\sigma(\mathbf{p}) + \frac{i}{2\tau_{\rm el}}{\rm sgn}\,(\omega)}. \tag{5.57}$$

5.4.2 Single-particle relaxation rate

With the disorder Green's function, we can calculate its leading correction to relaxation rates. To first order in the disorder there are two types of diagrammatic contributions to the single-particle relaxation rate: (A) diagrams that are formally the same as those shown in Fig. 5.2, except that the solid lines represent the disorder-averaged Green function given by Eq. (5.57), and (B) diagrams that have one explicit impurity line. The latter are shown in Fig. 5.5. It is easy to show that

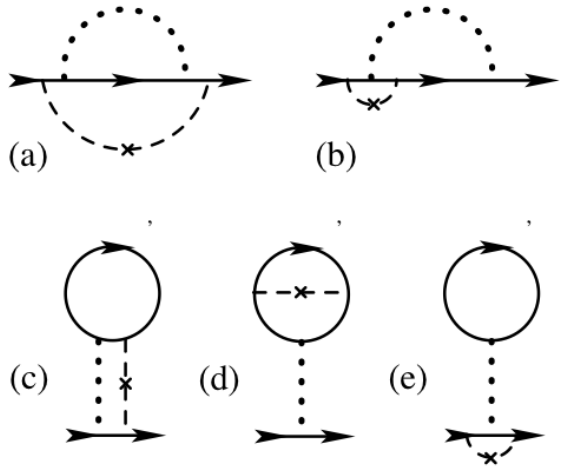

Figure 5.5: Fock (a,b) and Hartree (c-e) ontributions to the self-energy in the ballistic limit.

the various Hartree diagrams do not contribute. The class (A) Fock contribution to the self energy is given by Eq. (5.31), with $G_{0,\sigma}$ replaced by G_σ from Eq. (5.57).

Power counting shows that, (1) the leading contribution to the single-particle relaxation rate in the ballistic limit is proportional to T for helimagnons, and $T^{3/2}$ for columnar phase, (2) the diagrams of class (A) do not contribute to this leading term, and (3) of the diagrams of class (B) only diagram (a) in Fig. 5.5 contributes. Analytically, the contribution of this diagram to the self energy is

$$\begin{aligned}\Sigma_\sigma^{(a)}(\mathbf{p}, i\omega) &\equiv \Sigma_\sigma^{(a)}(i\omega) \\ &= -\frac{1}{2\pi N_{\mathrm{F}}\tau}\frac{T}{V}\sum_{\mathbf{k},i\Omega}\frac{1}{V}\sum_{\mathbf{p}'} V(\mathbf{k}, i\Omega; \mathbf{p}'-\mathbf{k}, \mathbf{p}') G_\sigma^2(\mathbf{p}', i\omega) G_\sigma(\mathbf{p}'-\mathbf{k}, i\omega - i\Omega)\end{aligned} \tag{5.58}$$

Notice that $\Sigma^{(a)}$ does not depend on the wave vector. This leads to the following leading disorder correction to the clean single-particle rate in Eqs. (5.50) and (5.52),

$$\delta\left(\frac{1}{\tau(\mathbf{p})}\right) \equiv \delta\left(\frac{1}{\tau}\right)$$
$$= \frac{V_0}{2\pi N_{\rm F}\tau}\frac{1}{V}\sum_{\mathbf{k}}\int_{-\infty}^{\infty}\frac{du}{\pi}n_{\rm F}\left(\frac{u}{T}\right)\chi''(\mathbf{k},u){\rm Im}\, L^{++,-}(\mathbf{k}). \qquad (5.59a)$$

Here χ'' is the spectral function is the spectral function of the susceptibility, given by Eq. (5.9), and $L^{++,-}$ is an integral

$$L^{++,-}(\mathbf{k}) = \frac{1}{V}\sum_{\mathbf{p}}\gamma(\mathbf{k},\mathbf{p})\gamma(\mathbf{k},\mathbf{p}-\mathbf{k})G_R^2(\mathbf{p})G_A(\mathbf{p}-\mathbf{k})$$
$$= i\nu^2\frac{2\pi}{3}\frac{N_{\rm F}m_{\rm e}^2}{\lambda^2 k_{\rm F}^2} + O(1/\tau, \mathbf{k}_\perp^2), \qquad (5.59b)$$

with $G_{R,A}(\mathbf{p}) = G_1(\mathbf{p}, i\omega \to \pm i0)$ the retarded and advanced Green functions respectively. For temperature scaling purpose, the leading correction to the relaxation time is given by [48]

$$\delta\left(\frac{1}{\tau}\right) \propto \delta\rho_{\rm el} \propto \delta\rho_{\rm th}$$
$$\sim \int du\, n_{\rm F}\left(\frac{u}{T}\right)\int dp_{||}\int dp_\perp^2\frac{1}{\omega_0(\mathbf{p})}\,\delta(u-\omega_0(\mathbf{p})). \qquad (5.60)$$

5.4.3 Electrical conductivity

Now we come to electrical conductivity. Using the bare disorder averaged Green function in Eq. (5.57), the Green function $\mathcal{G}$ can now be written as

$$\mathcal{G}(\mathbf{p}, i\omega) = \frac{1}{G^{-1}(\mathbf{p}, i\omega) - \delta\Sigma(\mathbf{p}, i\omega)}, \qquad (5.61)$$

where the self energy $\delta\Sigma$ does not contain the simple impurity self-energy that is incorporated in G.

We are interested in the leading disorder correction to the clean resistivity, and in the leading temperature dependence of that correction. To find this, it suffices to work to first order in both the disorder and the effective potential, and we can expand the conductivity up to linear order in $\delta\Sigma$ and the vertex function $\mathbf{\Gamma}$. From Eqs. (5.35a), (5.37) and (5.61) we find the following expression for the static conductivity $\sigma_{ij} = \mathrm{Re}\,\lim_{\Omega\to 0}\sigma_{ij}(i\Omega \to \Omega + i0)$:

$$\sigma_{ij} = \sigma_{ij}^{(0)} + \delta\sigma_{ij}^{\Sigma} + \delta\sigma_{ij}^{\Gamma}, \tag{5.62a}$$

with

$$\sigma_{ij}^{(0)} = \frac{1}{V}\sum_{\mathbf{p}} j_i(\mathbf{p})\, j_j(\mathbf{p}) \frac{1}{2T}\int \frac{d\epsilon}{4\pi} \frac{1}{\cosh^2\left(\frac{\epsilon}{2T}\right)} \left[G_R(\mathbf{p},\epsilon)G_A(\mathbf{p},\epsilon) - \mathrm{Re}\,\left(G_R(\mathbf{p},\epsilon)\right)^2\right], \tag{5.62b}$$

$$\delta\sigma_{ij}^{\Sigma} = \frac{1}{V}\sum_{\mathbf{p}} j_i(\mathbf{p})\, j_j(\mathbf{p}) \frac{1}{2T}\int \frac{d\epsilon}{4\pi} \frac{1}{\cosh^2\left(\frac{\epsilon}{2T}\right)} 2\mathrm{Re}\,\left[\left(G_R(\mathbf{p},\epsilon)\right)^2 G_A(\mathbf{p},\epsilon)\delta\Sigma_R(\mathbf{p},\epsilon) + \left(G_R(\mathbf{p},\epsilon)\right)^3 \delta\Sigma_R(\mathbf{p},\epsilon)\right], \tag{5.62c}$$

$$\delta\sigma_{ij}^{\Gamma} = \frac{1}{V}\sum_{\mathbf{p}} j_i(\mathbf{p}) \frac{1}{2T}\int \frac{d\epsilon}{4\pi} \frac{1}{\cosh^2\left(\frac{\epsilon}{2T}\right)} \mathrm{Re}\,\Big[G_R(\mathbf{p},\epsilon)G_A(\mathbf{p},\epsilon)\Gamma_j(\mathbf{p};\epsilon+i0,\epsilon-i0) - \left(G_R(\mathbf{p},\epsilon)\right)^2 \Gamma_j(\mathbf{p};\epsilon+i0,\epsilon+i0)\Big]. \tag{5.62d}$$

To write Eqs. (5.62) we have performed the Matsubara frequency sums and have introduced retarded and advanced Green functions $G_{R,A}(\mathbf{p},\epsilon) = G(\mathbf{p}, i\omega \to \epsilon \pm i0)$, and a retarded self energy $\delta\Sigma_R(\mathbf{p},\epsilon) = \delta\Sigma(\mathbf{p}, i\omega \to \epsilon + i0)$. Diagrammatically, these contributions to the conductivity are shown in Fig. 5.6. In evaluating these diagrams, we again make use of the small parameter $\frac{q}{k_\mathrm{F}} \ll 1$. To lowest order in $\frac{q}{k_\mathrm{F}}$, in many cases the Green function G can be replaced by the free-electron Green function, which greatly simplifies the integrals.

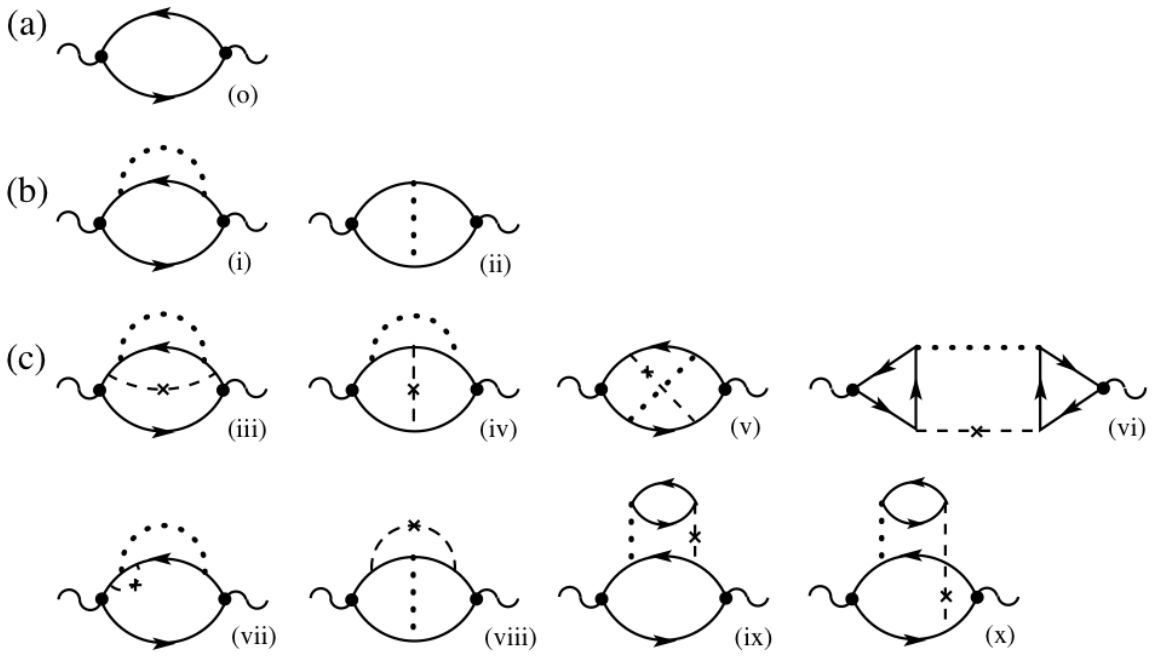

Figure 5.6: Leading disorder corrections to the clean conductivity. Solid lines denote the Green function G, dotted lines denote the effective potential, and dashed lines with crosses denote the impurity factor u_0.

Furthermore, the conductivity tensor is not isotropic, since the integrand depends on the helix pitch vector $\mathbf{q}$. However, simple symmetry considerations show that it is still diagonal, with different components in the directions parallel and perpendicular to $\mathbf{q}$, respectively,

$$\delta\sigma_{ij} = \delta_{ij}\left[\delta_{iz}\delta\sigma_{\mathrm{L}} + (1-\delta_{iz})\delta\sigma_{\perp}\right]. \tag{5.63}$$

The diagrams can be classified as follows. Diagram (o) in Fig. 5.6(a) represents $\sigma^{(0)}$. To lowest order in the disorder, and in $\frac{q}{k_{\mathrm{F}}}$, it yields the Drude conductivity,

$$\sigma_{ij}^{(0)} = \delta_{ij}\sigma_0\left[1 + O\left(\frac{1}{\epsilon_{\mathrm{F}}\tau}, \left(\frac{q}{k_{\mathrm{F}}}\right)^2\right)\right], \tag{5.64}$$

where

$$\sigma_0 = \frac{ne^2\tau}{m_e}, \tag{5.65}$$

with n the electron number density, e the electron charge, $m_{\rm e}$ the effective electron mass, and τ the elastic mean-free time between collisions.

Diagrams (i), (iii), (vii), and (ix) contribute to $\delta\sigma^{\Sigma}$, and the remaining diagrams contribute to $\delta\sigma^{\Gamma}$. Diagrams (i) and (ii) in Fig. 5.6(b) do not contain explicit impurity lines, and hence need to be evaluated to next-to-leading order in the disorder. The diagrams in Fig. 5.6(c) contain an explicit impurity line, and evaluating them to leading order suffices.

5.4.3.1 Diagrams without explicit impurity lines

Let us first consider the diagrams (i) and (ii). Standard techniques yield

$$\begin{aligned}\delta\sigma_{ij}^{(i)} &= -\frac{V_0}{4\pi}\frac{1}{T}\int_{-\infty}^{\infty}\frac{d\epsilon}{\cosh^2\left(\frac{\epsilon}{2T}\right)}\frac{1}{V}\sum_{\mathbf{k}}\int_{-\infty}^{\infty}\frac{du}{\pi}\chi''(\mathbf{k},u)\Bigg[n_{\rm B}\left(\frac{u}{T}\right)\mathrm{Re}\,J_{ij}^{++-,+}(k) \\ &\qquad +\frac{1}{2}n_{\rm F}\left(\frac{u-\epsilon}{T}\right)\mathrm{Re}\,\left[J_{ij}^{++-,+}(k)-J_{ij}^{++-,-}(k)\right]\Bigg], \qquad (5.66a)\\ \delta\sigma_{ij}^{(ii)} &= -\frac{V_0}{8\pi}\frac{1}{T}\int_{-\infty}^{\infty}\frac{d\epsilon}{\cosh^2\left(\frac{\epsilon}{2T}\right)}\frac{1}{V}\sum_{\mathbf{k}}\int_{-\infty}^{\infty}\frac{du}{\pi}\chi''(\mathbf{k},u)\Bigg[n_{\rm B}\left(\frac{u}{T}\right)\mathrm{Re}\,\left[J_{ij}^{+-,+-}(k)-I_{ij}^{+-,+-}(k)\right] \\ &\qquad +n_{\rm F}\left(\frac{u-\epsilon}{T}\right)\mathrm{Re}\,\left[J_{ij}^{+-,+-}(k)-I_{ij}^{+-,+-}(k)-J_{ij}^{+-,++}(k)+I_{ij}^{+-,++}(k)\right]\Bigg]. \qquad (5.66b)\end{aligned}$$

Here the J are defined by convolutions of Green functions,

$$J_{ij}^{++-,+}(k) = \frac{1}{V}\sum_{\mathbf{p}} j_i(\mathbf{p})j_j(\mathbf{p})\gamma(\mathbf{k},\mathbf{p})\gamma(\mathbf{k},\mathbf{p}-\mathbf{k})G_R(\mathbf{p})G_R(\mathbf{p})G_A(\mathbf{p})G_R(\mathbf{p}-\mathbf{k}), \tag{5.67a}$$

$$J_{ij}^{++-,-}(k) = \frac{1}{V}\sum_{\mathbf{p}} j_i(\mathbf{p})j_j(\mathbf{p})\gamma(\mathbf{k},\mathbf{p})\gamma(\mathbf{k},\mathbf{p}-\mathbf{k})G_R(\mathbf{p})G_R(\mathbf{p})G_A(\mathbf{p})G_A(\mathbf{p}-\mathbf{k}), \tag{5.67b}$$

$$J_{ij}^{+-,+-}(k) = \frac{1}{V}\sum_{\mathbf{p}} j_i(\mathbf{p})j_j(\mathbf{p})\gamma(\mathbf{k},\mathbf{p})\gamma(\mathbf{k},\mathbf{p}-\mathbf{k})G_R(\mathbf{p})G_A(\mathbf{p})G_R(\mathbf{p}-\mathbf{k})G_A(\mathbf{p}-\mathbf{k}), \tag{5.67c}$$

$$I_{ij}^{+-,+-}(k) = \frac{1}{V}\sum_{\mathbf{p}} j_i(\mathbf{p})j_j(\mathbf{k})\gamma(\mathbf{k},\mathbf{p})\gamma(\mathbf{k},\mathbf{p}-\mathbf{k})G_R(\mathbf{p})G_A(\mathbf{p})G_R(\mathbf{p}-\mathbf{k})G_A(\mathbf{p}-\mathbf{k}), \tag{5.67d}$$

where $G_{R,A}(\mathbf{p}) = G_{R,A}(\mathbf{p}, \epsilon = 0)$. Other convolutions are defined analogously, with the upper $\pm$ indices denoting retarded and advanced Green functions, and the comma separating them denoting the momentum structure of the convolution. In writing Eqs. (5.66), we have neglected contributions from other convolutions of four Green functions that are easily shown to be of higher order in the disorder than the ones we kept. For instance, a complete expression for diagram (i) contains contributions from $J_{ij}^{+++,-}$ and $J_{ij}^{+++,+}$, which are subleading in this sense. Also, a complete evaluation of the diagrams yields nominal contributions proportional to χ', the Kramers-Kronig transform of χ''. These vanish once the real part is taken, as is to be expected: by Fermi's golden rule, to first order in the interaction potential, the scattering cross-section and hence the conductivity depend only on the spectrum of the potential. Finally, we have used the fact that the internal frequencies u and ϵ

in Eqs. (5.66) scale as the temperature T. To find the leading temperature dependence, we therefore can drop the frequency dependence of the Green functions, and this is reflected in Eqs. (5.67).

To evaluate the integrals in Eqs. (5.67) we work to lowest order in $\frac{q}{k_{\mathrm{F}}}$. We further neglect λ, since in our effective single-spin-projection model it amounts (at $q = 0$) to just a shift of the Fermi energy. That is, we replace $\omega_1(\mathbf{p})$ in Eq. (5.15b) by $\xi_{\mathbf{p}}$. We further use a nearly-free electron expression for $\xi_{\mathbf{p}}$, i.e., we put $\nu = 0$ in Eq. (5.21). These simplifications lead in particular to $j_i(\mathbf{p}) = \frac{p_i}{m_{\mathrm{e}}}$, and to lowest order in the disorder the integrals can be evaluated in the familiar approximation that replaces the integration over $|\mathbf{p}|$ by a contour integration over $\xi_{\mathbf{p}}$, [53] which we refer to as the Abrikosov-Gorkov-Dzyaloshinskii (AGD) approximation. With calculations outlined in Appendix F, we obtain, for helimagnons,

$$\delta\sigma_{ij}^{(i)} + \delta\sigma_{ij}^{(ii)} = O(\tau^2 T^{5/2}) + o(\tau T). \tag{5.68a}$$

and for A phase,

$$\delta\sigma_{ij}^{(i)} + \delta\sigma_{ij}^{(ii)} = O(\tau^2 T^{7/2}) + o(\tau T^2). \tag{5.68b}$$

5.4.3.2 Diagrams with explicit impurity lines

We now turn to the diagrams in Fig. 5.6(c), which carry an explicit impurity line. Their contribution to the conductivity is of $O(\tau)$, and it thus suffices to calculate them to leading order in the disorder. Before we do so, we identify the small parameter that controls our disorder expansion. As we point out in Appendix F for diagrams (i) and (ii), the expansion parameter for the convolutions J that appear

in the integrand in Eqs. (5.66) is $\delta = \frac{1}{v_{\rm F} k_\perp \tau}$, with $v_{\rm F} = \frac{k_{\rm F}}{m_{\rm e}}$ the Fermi velocity. According to Eq. (4.22), the transverse wave number scales as the square root of the helimagnon frequency at intermediate temperatures. For helimagnons, the small expansion parameter is thus

$$\delta = \frac{\lambda}{\sqrt{(\epsilon_{\rm F}\tau)^2 T}}, \tag{5.69}$$

and this will turn out to be true for the diagrams in Fig. 5.6(c) as well. For A phase, as the transverse wavenumber scales as the frequency of the corresponding Goldstone modes, the small parameter that controls the ballistic regime is $\frac{1}{T\tau}$, just as the Coulomb case [104].

The diagrams in Fig. 5.6(c) all contain six Green functions that factorize into two sets of momentum convolutions containing n and $6-n$ Green functions, respectively, with $n = 3$ or $n = 4$. Diagrams (iii) - (vi) contain the $(3,3)$ partitions, whereas diagrams (vii) - (x) contain the $(4,2)$ partitions. The same power-counting arguments that we employed for diagrams (i) and (ii), and that are explained in Appendix F, reveal the following:

First, to lowest order in the small parameter $\frac{q}{k_{\rm F}}$ (i.e., replacing the helimagnon Green functions by nearly-free electron Green functions), only the $(3,3)$ partitions contribute to $O(\tau T)$, whereas the $(4,2)$ partitions are of higher order in the temperature. That is,

$$\delta\sigma_{ij}^{(vii)-(x)} = o(\tau T) \tag{5.70}$$

to lowest order in $\frac{q}{k_{\rm F}}$, and we will evaluate all other diagrams to lowest order in this small parameter as well. Details can be found with diagram (vii) in Appendix F.

Second, for the conductivity correction $\delta\sigma_\perp$ in $\perp$ (x, y) directions, only diagram (iii) contributes to $O(\tau T)$, whereas for $\delta\sigma_z$ the other $(3, 3)$ partitions also contribute.

In addition, by considering the reality properties of the convolutions involved, one finds that, third, diagram (vi) is given in terms of the real part of a convolution that is purely imaginary, and hence does not contribute.

Finally, a cursory inspection of the integrals in addition to power counting shows that the terms that contain a bosonic distribution function (in analogy to the first terms in Eqs. (5.66a) and (5.66b), respectively), have a potential to be of $O(\tau T \ln \delta)$ rather than of $O(\tau T)$. However, the leading contribution to diagram (iii) does not contain such terms. Diagrams (iv) and (v) do, but the logarithmic terms cancel between these two diagrams, and this can be seen without performing the integrals.

Hence we give analytic expression for different terms.

Diagram (iii) After the above preliminary considerations, we now evaluate diagram (iii). The leading contribution can be written

$$\delta\sigma_{ij}^{(iii)} = \frac{u_0 V_0}{8\pi}\frac{1}{T}\int_{-\infty}^{\infty}\frac{d\epsilon}{\cosh^2\left(\frac{\epsilon}{2T}\right)}\frac{1}{V}\sum_{\mathbf{k}}\int_{-\infty}^{\infty}\frac{du}{\pi}n_{\mathrm{F}}\left(\frac{u-\epsilon}{T}\right)\chi''(\mathbf{k},u)K_{ij}^{++-}L^{++,-}(\mathbf{k}). \tag{5.71}$$

Here

$$\begin{aligned} K_{ij}^{++-} &= \frac{1}{V}\sum_{\mathbf{p}}\frac{p_i p_j}{m_{\mathrm{e}}^2}G_R(\mathbf{p})G_R(\mathbf{p})G_A(\mathbf{p}) \\ &= -\delta_{ij}\frac{2\pi i}{3}\frac{k_{\mathrm{F}}^2 N_{\mathrm{F}}}{m_{\mathrm{e}}^2}\tau^2 + O(\tau), \end{aligned} \tag{5.72}$$

and

$$L^{++,-}(\mathbf{k}) = \frac{1}{V}\sum_{\mathbf{p}} \gamma(\mathbf{k};\mathbf{p})\gamma(\mathbf{k};\mathbf{p}-\mathbf{k})G_R(\mathbf{p})G_R(\mathbf{p})G_A(\mathbf{p}-\mathbf{k})$$
$$= i\nu^2 \frac{2\pi}{3}\frac{N_{\rm F} m_{\rm e}^2}{\lambda^2 k_{\rm F}^2} + O(\frac{1}{\tau}, k_\perp^2). \quad (5.73)$$

The second lines in Eqs. (5.72) and (5.73) are easy to obtain in the AGD approximation. Only the term proportional to $\mathbf{k}_\perp$ for helimagnon, or k_z, in $\gamma(\mathbf{k};\mathbf{p})$, Eq. (5.23c), contributes to the leading temperature dependence, hence the proportionality to ν^2. We again have dropped the frequency dependence of the Green functions, since it does not contribute to the leading temperature dependence. Consequently, the integral over ϵ in Eq. (5.71) can be performed. Using the fact that the helimagnon spectrum χ'' is an odd function of the frequency, we can write

$$\delta\sigma_{ij}^{(iii)} = -\frac{u_0 V_0}{4\pi}\frac{1}{V}\sum_{\mathbf{k}}\int_{-\infty}^{\infty}\frac{du}{\pi}\chi''(\mathbf{k},u)C(u/2T)K_{ij}^{++-}L^{++,-}(\mathbf{k}), \quad (5.74a)$$

with

$$C(x) = \coth x - \frac{x}{\sinh^2 x}. \quad (5.74b)$$

We next cast the expressions corresponding to diagrams (iv) and (v) in an analogous form, before performing the final integrals.

Diagrams (iv) **and** (v) Using the same techniques as for diagram (iii), we find for the leading contributions to diagrams (iv) and (v)

$$\delta\sigma_{ij}^{(iv)+(v)} = -\frac{u_0 V_0}{2\pi}\frac{1}{V}\sum_{\mathbf{k}}\int_{-\infty}^{\infty}\frac{du}{\pi}\chi''(\mathbf{k},u)C(u/2T)M_i^{+-,+}(\mathbf{k})M_j^{+-,+}(\mathbf{k}) \quad (5.75)$$

Here

$$M_i^{+-,+}(\mathbf{k}) = \frac{1}{V}\sum_{\mathbf{p}} \frac{p_i}{m_{\rm e}} \gamma(\mathbf{k};\mathbf{p}) G_R(\mathbf{p}) G_A(\mathbf{p}) G_R(\mathbf{p}-\mathbf{k}) = -\delta_{iz}\frac{2\pi}{3}\nu\frac{N_{\rm F}}{\lambda}\tau + O(\tau^0). \quad (5.76)$$

5.4.3.3 The conductivity in the ballistic limit

Collecting our results of the leading order, we now have

$$\delta\sigma_{ij} = -\frac{u_0 V_0}{4\pi}\frac{1}{V}\sum_{\mathbf{k}}\int_{-\infty}^{\infty}\frac{du}{\pi}\chi''(\mathbf{k},u) C\left(\frac{u}{2T}\right)\left[K_{ij}^{++,-}L^{++,-}(\mathbf{k}) + 2M_i^{+-,+}(\mathbf{k})M_j^{+-,+}(\mathbf{k})\right]. \quad (5.77)$$

Because the terms in the square bracket in Eq. (5.77) do not depend on the temperatures, its dependence of temperature depends on the other part of the integrals. For temperature scaling purposes, the change in conductivity can be seen as

$$\delta\sigma \propto \delta\rho_{\rm el} \propto \delta\rho_{\rm th} \sim \int du\, n_{\rm F}\left(\frac{u}{T}\right)\int dp_{||}\int dp_\perp^2\, \frac{1}{\omega_0(\mathbf{p})}\,\delta(u-\omega_0(\mathbf{p})), \quad (5.78)$$

which is the same as the correction of single-particle relaxation time in Eq. (5.60). The expression Eq. (5.78) can be seen as the correction to the transport rate $\frac{1}{\tau_{\rm el}}$ through Taylor's expansion.

5.4.4 Summary

In the ballistic regime there is an additional contribution $\delta\left(\frac{1}{\tau}\right)$ to the relaxation rates that is qualitatively the same for both the single-particle rate and the

electron transport rate, and thus provides the temperature dependence of the corrections to both the electrical and thermal resistivities. It was shown above that, for temperature scaling purposes, this contribution can be represented by

$$\begin{aligned}\delta(1/\tau) &\propto \delta\rho_{\rm el} \propto \delta\rho_{\rm th} \\ &\sim \int du\, n_{\rm F}\left(\frac{u}{T}\right)\int dp_{||}\int dp_{\perp}^2\ \frac{1}{\omega_0(\mathbf{p})}\delta(u-\omega_0(\mathbf{p})).\end{aligned} \tag{5.79}$$

5.4.4.1 Generalized helimagnons

From Eq. (5.79), we see that at temperatures where pinning effects are not important, generalized helimagnons lead to $\delta\left(\frac{1}{\tau}\right) \propto T$, a result first obtained in Ref. [103]. At asymptotically low temperatures, characterized by $T \ll \frac{\tilde{c}_\perp}{\sqrt{c_\perp}}$, one finds a T^2-behavior. In the pinned helical phase the crossover temperature between these two regimes is determined by the strength of the crystal-field effects; in the conical phase the magnetic field also cuts off the universal hydrodynamics T-behavior.

5.4.4.2 Columnar phase

For the columnar phase, Eq. (4.12) yields

$$\delta\left(\frac{1}{\tau}\right) \propto \begin{cases} T^2 & \text{if } T \ll \frac{c_z'}{\sqrt{c_z}} \\ \\ T^{3/2} & \text{if } T \gg \frac{c_z'}{\sqrt{c_z}} \end{cases}. \tag{5.80}$$

The pinning effects in the columnar phase are very weak due to the hexagonal nature of the lattice, with c_z' only of $O(g_{\rm so}^6)$, see Sections 3.4.4 and 4.4.4. The size of the asymptotic region is therefore likely to be dominated by the H-dependence of c_z'. Whether or not the universal hydrodynamic $T^{3/2}$-behavior is observable in the

columnar phase (there currently are no experimental indications that it is) would require a detailed quantitative analysis that goes beyond the scope of the this thesis.

5.5 NFL region

The preceding result is also of interest with respect to the non-Fermi-liquid region shown in Fig. 1.11, which is *not* a phase with long-range order, but where the electrical conductivity shows a pronounced $T^{3/2}$-behavior. [23] An explanation that has been proposed [50] is as follows. The $T^{3/2}$-behavior derived above is a consequence of the structure of the Goldstone modes due to columnar fluctuations, Eq. (4.12), in conjunction with weak quenched disorder. In the columnar phase, which displays long-range order in the form of a columnar lattice, there are two such Goldstone modes, see Sections 4.3. If the NFL region can be interpreted as a melted columnar lattice, then the resulting liquid of columns will still have one Goldstone mode with the same structure, namely, the compression mode mentioned in Sec. 4.3. Weak quenched disorder will then still produce a contribution to the electrical resistivity, as well as to the single-particle relaxation rate, that is proportional to $T^{3/2}$ in a pre-asymptotic region. The NFL region is observed to extend to a vanishing external magnetic field, so the low-T boundary of the universal hydrodynamic region is determined by the pinning effects, which are very weak, see Secs. 3.4.4 and 4.4.4. The universal hydrodynamic $T^{3/2}$ behavior is therefore expected to extend to very low temperatures. A remaining question is the size of the prefactor, which in a bare theory is expected to be small due to the long length scale set by the lattice in the

columnar phase. The resolution proposed in Ref. [50] is that mode-mode coupling effects drastically enhance the magnitude of the effect, in analogy to what is believed to happen in the blue phases of liquid crystals. [39] (See Chapter 3.)

5.6 Conclusion

In this chapter, we analyzed the effects of the Goldstone modes in helimagnets to the temperature dependences of specific heat, thermal resistivity and electrical resistivity. The specific heat was calculated by treating the Goldstone modes as gases in the system. The transport properties were treated by a microscopic model that couples the Goldstone modes and the fluctuations of electronic density. We calculated the thermal and electrical resistivities by considering the effect of coupling to the Green functions. We also evaluated the corrections to the resistivities due to weak disorder. Our results are summarized in Table 5.1. We successfully met our result in NFL phase with the experimental results, that the electrical resistivity $\Delta\rho \sim T^{3/2}$. On the other hand, we deduced the temperature dependences of these transport properties in other ordered phases.

			pinned helical /conical	columnar	NFL
		no. of Goldstone modes	1	2	1
clean	$C(T)$	universal hydrodynamic regime	T^2	$T^{5/2}$	$T^{5/2}$
		crystal-field regime	T^3	T^3	
	$\tau(T)^{-1}$ $\rho_{\rm th}(T)$	universal hydrodynamic regime	$T^{3/2}$	T^2	T^2
		crystal-field regime	T^3	T^3	
	$\rho_{\rm el}(T)$	universal hydrodynamic regime	$T^{5/2}$	T^3	T^3
		crystal-field regime	T^5	T^5	
ballistic disorder	$\delta\rho_{\rm el}(T)$	universal hydrodynamic regime	T	$T^{3/2}$	$T^{3/2}$
	$\delta\rho_{\rm th}(T)$	crystal-field regime	T^2	T^2	

Table 5.1: Properties of various ordered phases and the proposed state representing the non-Fermi-liquid region. Listed are the number of Goldstone modes, and the temperature dependence of various observables. The universal hydrodynamic regime is the temperature region where crystal-field effects are not important. It is bounded above by T_q, see Eq. (4.25). The true asymptotic behavior as $T \to 0$ is dominated by the crystal-field effects and is realized only at very low temperatures. In the presence of weak ballistic disorder, the regime dominated by crystal-field effects is bounded below as well as above and does not represent the true asymptotic low-temperature regime, see Eq. (5.54).

Chapter 6

Basics of Skyrmions

The columnar phase in helimagnets has been identified as a hexagonal lattice of columnar Skyrmions. It has been described by the superposition of three helimagnets with pitch vectors perpendicular to the applied magnetic field, as in Section 3.3.1, and an Abrikosov lattice, as in Section 3.3.2. On the other hand, the NFL-phase in Fig. 1.11 is believed to be a phase of Skyrmion liquid, from its electronic properties, [48] see Section 4.3. Therefore, it is important to understand more about isolated Skyrmions, or Wannier Skyrmions, as opposed to Skyrmion lattice, or Bloch Skyrmions, as excitations. In this chapter, we review some basic properties of a Skyrmion. We discuss about Skyrmions as excitations in the next chapter.

6.1 Winding number

Skyrmions are two-dimensional topological objects. Assume that

$$\mathbf{M}(\mathbf{x}) = m(\mathbf{x})\mathbf{n}(\mathbf{x}), \tag{6.1}$$

where $m(\mathbf{x})$ and $\mathbf{n}(\mathbf{x})$ denotes the magnitude and direction of $\mathbf{M}$. The winding number for Skyrmion is defined as, [67]

$$W = \int dx \int dy \frac{1}{4\pi} \mathbf{n} \cdot \left(\frac{\partial \mathbf{n}}{\partial x} \times \frac{\partial \mathbf{n}}{\partial y} \right), \tag{6.2}$$

as in Eq. (1.4). Upon continuous deformation of the configurations, the winding number W remains unchanged. A Skyrmion is topologically non-trivial because its winding number is non-zero.

Note that all phases in Chapter 3, except the columnar phase, have $W = 0$, which means they are all topologically trivial.

6.2 Skyrmion as a saddle point of the non-linear σ model

A Skyrmion embedded in a ferromagnet can be studied with the two-dimensional non-linear σ model, with the action given by [106, 107]

$$\mathcal{S}[\mathbf{n}] = \frac{J}{2}\int d^2x(\nabla\mathbf{n})^2, \tag{6.3}$$

with a constraint $\mathbf{n}^2(\mathbf{x}) = 1$. There exists a metastable mean-field solution that corresponds to a Skyrmion given by [1] [108, 109, 110]

$$n_x = -\frac{2l\rho\sin\varphi}{l^2+\rho^2}, \tag{6.4a}$$

$$n_y = \frac{2l\rho\cos\varphi}{l^2+\rho^2}, \tag{6.4b}$$

$$n_z = \frac{\rho^2-l^2}{\rho^2+l^2}. \tag{6.4c}$$

where l is an arbitrary length that characterizes the size of the Skyrmion core. From Eq. (6.2), this solution has a winding number $W = -1$, confirming that it is a Skyrmion. This refers to an azimuthal Skyrmion. However, Ref. [110] does not exclude the possibility of a radial Skyrmion. For example, the Skyrmion in the p-wave superconductors [58, 59] is a radial one.

[1] We adopt the cylindical coordinates, $\mathbf{x} = \rho\cos\varphi\hat{\mathbf{x}} + \rho\sin\varphi\hat{\mathbf{y}} + z\hat{\mathbf{z}}$, which is the notation that we are using in this and the next chapters.

In CP^1 representation (see Appendix B), the Skyrmion in Eqs. (6.4) can be written as, as in Eq. (B.9a),

$$\mathbf{z} = \sqrt{\frac{\rho^2}{\rho^2 + l^2}} \begin{bmatrix} e^{i\left(\frac{\pi}{2} - \varphi\right)} \\ \\ \frac{l}{\rho} \end{bmatrix}, \tag{6.5}$$

which is an anti-vortex. [68] This provides the basis of using the analogy of Abrikosov vortices to study the Skyrmion lattice as in Section 3.3.2.

This Skyrmion has the asymptotic expression for its tail ($\rho \to \infty$) given by

$$\theta(\rho) \approx \begin{cases} \pi - \frac{\rho}{2l}, & \text{for } \rho \approx 0 \\ \\ \frac{2l}{\rho}, & \text{for } \rho \to \infty. \end{cases} \tag{6.6}$$

We cannot determine l unless we have additional interactions that give extra length scales to the system, [110, 74] see Chapter 7.

6.3 Description of Skyrmions

To illustrate a topologically non-trivial solution, we write the configuration in the form of [24] (in cylindrical coordinates)

$$\mathbf{n}(\mathbf{x}) = \sin\theta(\mathbf{x})\cos\alpha(\mathbf{x})\hat{\rho} + \sin\theta(\mathbf{x})\sin\alpha(\mathbf{x})\hat{\varphi} + \cos\theta(\mathbf{x})\hat{\mathbf{z}}, \tag{6.7}$$

so that the winding number can be written as

$$W = \frac{1}{4\pi}\int_0^\infty d\rho \int_0^{2\pi} d\varphi \cdot \sin\theta(\mathbf{x}) \left[-\frac{\partial\theta(\mathbf{x})}{\partial\varphi}\frac{\partial\alpha(\mathbf{x})}{\partial\rho} + \left(1 + \frac{\partial\alpha(\mathbf{x})}{\partial\varphi}\right)\frac{\partial\theta(\mathbf{x})}{\partial\rho} \right]. \tag{6.8}$$

In terms of this representation, the Skyrmion in the non-linear σ model in the Section 6.2 is [111, 58]

$$\alpha(\mathbf{x}) = \frac{\pi}{2}, \tag{6.9a}$$

$$\theta(\mathbf{x}) = 2\tan^{-1}\frac{l}{\rho}. \tag{6.9b}$$

Note that this refers to an azimuthal Skyrmion.

For all the Skyrmions we review and present in this thesis, $\theta(\rho = 0) = \pi$ and $\theta(\rho = \infty) = 0$. This means a reverse spin at the core of the Skyrmion. In addition, we set $\alpha = \frac{\pi}{2}$, meaning it is an azimuthal Skyrmion. We exclude the consideration of a radial Skyrmion because the presence of DM interaction forces the Skyrmions be azimuthal. This also ensures that $W = -1$. [74] Such a Skyrmion is depicted in Fig. 6.1. The winding number describes how the electron changes its spin when it passes through the core, as shown in Fig. 1.20. [66]

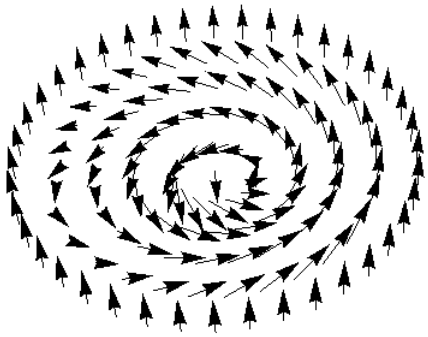

Figure 6.1: The picture of an isolated azimuthal Skyrmion with $W = -1$.

Although Skyrmions are topological objects, linear response ensures that the asymptotic behaviors of the tails of Skyrmions are no different from the decay of other kinds of perturbations, see Appendix C. It is the characteristics of the core that constitutes the topology. In understanding Skyrmions in various ordered phases of the helimagnets, we study the core by differential equations with boundary conditions that give a non-zero winding number, and the tail through perturbation theory.

6.4 Saddle-point equations for $m(\mathbf{x})$, $\theta(\mathbf{x})$ and $\alpha(\mathbf{x})$

To study Skyrmions, from now onwards, we consider only the Landau-Ginzburg terms, Zeeman terms and the DM interactions in Eq. (2.1), which corresponds to the saddle-point equation [112]

$$r\mathbf{M} - a\nabla^2\mathbf{M} + c\nabla\times\mathbf{M} + uM^2\mathbf{M} - \mathbf{H} = 0. \tag{6.10}$$

6.4.1 In paramagnets and ferromagnets

Putting Eqs. (6.1) and (6.7) with $\alpha(\mathbf{x}) = \frac{\pi}{2}$ in Eq. (6.10), the saddle-point equation becomes

$$\begin{aligned} rm - a\left[\left(\frac{\partial^2 m}{\partial\rho^2} + \frac{1}{\rho}\frac{\partial m}{\partial\rho}\right) - m\left(\frac{\partial\theta}{\partial\rho}\right)^2 - \frac{1}{\rho^2}m\sin^2\theta\right] \\ +cm\left(\frac{\partial\theta}{\partial\rho} + \frac{1}{\rho}\sin\theta\cos\theta\right) + um^3 - H\cos\theta = 0, \end{aligned} \tag{6.11a}$$

$$\begin{aligned} am\left(\frac{\partial^2\theta}{\partial\rho^2} + \frac{1}{\rho}\frac{\partial\theta}{\partial\rho} - \frac{1}{\rho^2}\sin\theta\cos\theta + \frac{2}{m}\frac{\partial m}{\partial\rho}\frac{\partial\theta}{\partial\rho}\right) \\ +c\left(\frac{\partial m}{\partial\rho} + \frac{1}{\rho}m\sin^2\theta\right) - H\sin\theta = 0. \end{aligned} \tag{6.11b}$$

These two equations are useful for describing a Skyrmion in paramagnets and ferromagnets in Chapter 7.

6.4.2 In helimagnetic phases

Putting Eqs. (6.1) and (6.7), and with

$$\xi = qz - \varphi, \tag{6.12}$$

in Eq. (6.10), the Eq. (6.10) gives the following equations:

$$\begin{aligned} rm_s\sin\theta\cos\alpha - a\left\{\frac{1}{\rho}\frac{\partial}{\partial\rho}\left[\rho\frac{\partial}{\partial\rho}(m_s\sin\theta\cos\alpha)\right]\right\} \\ -a\left\{\left(\frac{1}{\rho^2}+q^2\right)\frac{\partial^2}{\partial\xi^2}(m_s\sin\theta\cos\alpha) + \frac{2}{\rho^2}\frac{\partial}{\partial\xi}(m_s\sin\theta\sin\alpha) - \frac{1}{\rho^2}m_s\sin\theta\cos\alpha\right\} \\ +c\left[-\frac{1}{\rho}\frac{\partial}{\partial\xi}(m_s\cos\theta) - q\frac{\partial}{\partial\xi}(m_s\sin\theta\sin\alpha)\right] + um_s^3\sin\theta\cos\alpha = 0, \end{aligned} \tag{6.13a}$$

$$\begin{aligned} rm_s\sin\theta\sin\alpha - a\left\{\frac{1}{\rho}\frac{\partial}{\partial\rho}\left[\rho\frac{\partial}{\partial\rho}(m_s\sin\theta\sin\alpha)\right]\right\} \\ -a\left\{\left(\frac{1}{\rho^2}+q^2\right)\frac{\partial^2}{\partial\xi^2}(m_s\sin\theta\sin\alpha) - \frac{2}{\rho^2}\frac{\partial}{\partial\xi}(m_s\sin\theta\cos\alpha) - \frac{1}{\rho^2}m_s\sin\theta\sin\alpha\right\} \\ +c\left[-\frac{\partial}{\partial\rho}(m_s\cos\theta) + q\frac{\partial}{\partial\xi}(m_s\sin\theta\cos\alpha)\right] + um_s^3\sin\theta\sin\alpha = 0, \end{aligned} \tag{6.13b}$$

$$\begin{aligned} rm_s\cos\theta - a\left\{\frac{1}{\rho}\frac{\partial}{\partial\rho}\left[\rho\frac{\partial}{\partial\rho}(m_s\cos\theta)\right] + \left(\frac{1}{\rho^2}+q^2\right)\frac{\partial^2}{\partial\xi^2}(m_s\cos\theta)\right\} \\ +c\left[\frac{1}{\rho}\frac{\partial}{\partial\rho}(\rho m_s\sin\theta\sin\alpha) + \frac{1}{\rho}\frac{\partial}{\partial\xi}(m_s\sin\theta\cos\alpha)\right] + um_s^3\cos\theta - H = 0. \end{aligned} \tag{6.13c}$$

These equations are particularly hard to solve. But they are important for detailed analysis for Skyrmions in anti-conical phases in Chapter 7.

6.5 Conclusion

In this chapter, we reviewed the basis of a single Skyrmiom, such as its topological winding number. We defined a form of representation, Eq. (6.7), suitable for describing Skyrmions in helimagnet, with the corresponding saddle-point equations, Eqs. (6.13).

Chapter 7

Skyrmions and Their Sizes

In this chapter, we discuss the core and tail behaviors of a single Skyrmion, as an excitation, for various phases in helimagnets, as shown in Fig. 7.1, without considering crystal-field effects. We find the core and tail solution of the Skyrmions, and match the two solutions together. We estimate the size of Skyrmions with different definitions. At the end, we estimate the core-to-core distance with the Abrikosov solution of Skyrmion lattice in Sec. 3.3.2.

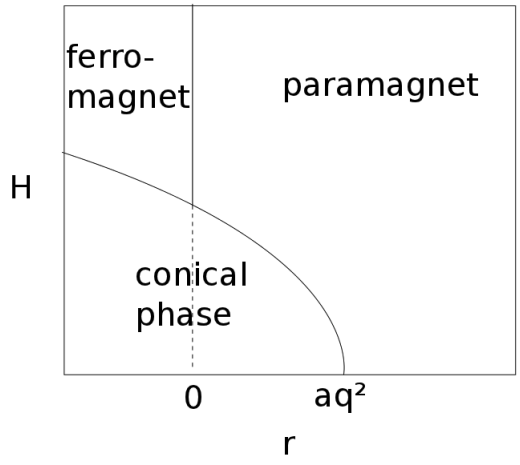

Figure 7.1: Phase diagram predicted by the action with $S_{\rm M}[\mathbf{M}] + S_{\rm DM}[\mathbf{M}]$ in Eqs. (2.2a) and (2.3a).

7.1 Skyrmion cores

7.1.1 Ferromagnet and paramagnet

We first explore the cases of paramagnets and ferromagnets. And as we have stated in Section 6.3, $\theta(\rho = 0) = \pi$. Then we write, for $\rho \to 0$,

$$m(\mathbf{x}) = m_\infty + \delta m(\rho), \tag{7.1a}$$

$$\theta(\mathbf{x}) = \pi + \delta\theta(\rho), \tag{7.1b}$$

where all behavior depends only on the radial distance ρ, and where $m_\infty = M_P$ (for paramagnet, $r > 0$, as in Eq. (A.2a)) or M_F (for ferromagnet, $r < 0$, as in Eq. (A.3a)). Putting Eqs. (7.1) in the saddle-point equations, Eqs. (6.11), ignoring all higher order terms, we can find that for $\rho \to 0$, $\delta\theta = \Theta_c \rho$ and $\delta m = M_c \rho^2$, with

$$M_c = \frac{m_\infty}{2\bar{l}_H^2(1 + 4q^2\bar{l}_H^2)}, \tag{7.2a}$$

$$\Theta_c = -\frac{2q}{1 + 4q^2\bar{l}_H^2}, \tag{7.2b}$$

where $\bar{l}_H$ is the transverse correlation length for paramagnets or ferromagnets in Eq. (2.12a), Eq. (2.12b) or Eq. (2.12c). Note that this calculation breaks down if there is no DM interaction, or the Skyrmion is in an ordered phase.

The size of the core can be estimated with this solution as R, where $\theta = \pi\left(1 - \frac{\rho}{R}\right)$, as shown in Fig. 7.2. [69] Let us consider different cases in ferromagnets and paramagnets, and the relation of Skyrmion in paramagnets in some situations to the Skyrmion lattice.

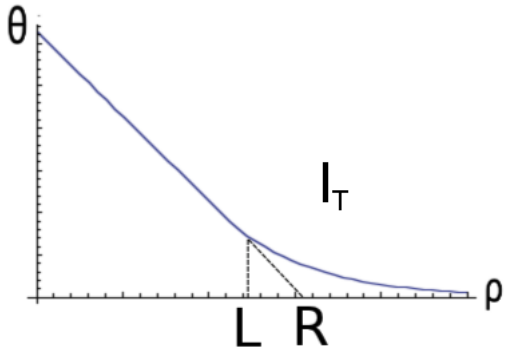

Figure 7.2: Different characterizations of the Skyrmion sizes. [74]

7.1.1.1 Ferromagnet

For a ferromagnet with non-zero magnetic field, the core size R is given by the following cases (with the phase stable or metastable):

1. $\bar{l}_H \ll q^{-1}$: $R \approx \frac{\pi}{2q}$.

2. $q^{-1} \ll \bar{l}_H$: $R \approx 2\pi q \bar{l}_H^2$.

The first case refers to the region where the magnetic field is much larger than the critical field H_{c2}. The core size is proportional to q^{-1}. The second case refers to the region closer to $H = H_{c2}$, where the magnetic length $\bar{l}_H$ plays a role.

7.1.1.2 Paramagnet

For a paramagnet, the core size R is given by (in which the phase can be stable or metastable):

1. $\xi_p \ll q^{-1}$: $R \approx \frac{\pi}{2q}$.

2. $\xi_p \approx q^{-1}$ and along $H \approx H_{c2}$: $R \approx \frac{5\pi}{2q}$.

The magnetic field does not play a role in the core behavior for paramagnets. It is because close to $r \approx 0$, the paramagnet appears for $H > H_{c2}$ and $\bar{l}_H$ is less significant than the contribution of q^{-1}. For $r > u^{\frac{1}{3}} H^{\frac{2}{3}}$, $\bar{l}_H \approx \xi_p$, as in Eq. (2.12a).

7.1.2 Aligned conical phase

The core behavior for aligned conical phase is different from paramagnets and ferromagnets in Section 7.1.1 because of the Goldstone mode in this phase. To understand it, we first study ferromagnet without external magnetic field and DM interaction. This is for illustrative purpose, because it breaks a continuous symmetry just like the conical phase does.

7.1.2.1 Ferromagnet without external magnetic field and DM interaction

With $H = 0$ and $q = 0$, the ferromagnet (with $r < 0$) is an ordered phase that breaks the continuous rotational symmetry of the action in Eq. (2.2a). The differential equation for $\delta\theta$ in Eq. (7.1b) as in Eq. (6.11b) becomes

$$\frac{d^2\delta\theta}{d\rho^2} + \frac{1}{\rho}\frac{d\delta\theta}{d\rho} - \frac{1}{\rho^2}\delta\theta = 0. \tag{7.3}$$

The differential equation is due to the gradient term in the action. Then

$$\delta\theta = A\rho, \tag{7.4}$$

with an arbitrary coefficients A. In fact, the approximation in Eq. (6.6) from the exact Skyrmion solution to the non-linear σ model near the core gives the same.

Therefore, we cannot determine the core size. To determine the core size just from the core behavior, external perturbations that provide extra length scales are needed. See Section 7.2.2.1.

7.1.2.2 Aligned conical phase

The aligned conical phase breaks the continuous translational symmetry of the action in Eq. (2.1), see Chapter 4. [48] Because of the helical nature of this phase, we expect $m(\mathbf{x})$, $\theta(\mathbf{x})$ and $\alpha(\mathbf{x})$ depend on ξ (defined in Eq. (D.17)) in addition to the radial distance ρ. After analyzing Eqs. (6.13), the dominant variation near the core is $\rho \sin \xi$. However, the coefficients is undetermined for the same reason as the ferromagnet above. The perturbation for conical phase can be written as Eq. (7.10). The differential equations for the fluctuations for conical phase can be written as a Laplace equation as in Eq. (7.11), although both gradient terms and curl term (due to DM interaction) in the action in Eq. (2.1) are important for the aligned conical phase.

7.2 Skyrmion tails

The tail behavior of the Skyrmions is closely related to the correlations in the bulk of the phase. [97] This can be shown by linear response theory, see Appendix C. In the following, we show by each case that the presence of spontaneous symmetry breaking gives the Skyrmion an algebraic tail, but an exponentially decaying tail otherwise. The decay length of the tail, l_T, is in general not the same as the core

size, as shown in Fig. 7.2.

7.2.1 Paramagnet and Ferromagnet

We study the system using perturbation techniques. As we have stated in Section 6.3, $\theta(\rho = \infty) = 0$. Then we write, for $\rho \to \infty$,

$$m(\mathbf{x}) = m_\infty + \delta m(\rho), \tag{7.5a}$$

$$\theta(\mathbf{x}) = 0 + \delta\theta(\rho), \tag{7.5b}$$

where all behavior depends only on the radial distance ρ, and $m_\infty = M_P$ (for paramagnet, $r > 0$, as in Eq. (A.2a)) or M_F (for ferromagnet, $r < 0$, as in Eq. (A.3a)) as in Section 7.1. We expect that the tail is exponential. Hence, we assume $\delta m = \tilde{M} e^{-K\rho}$ and $\delta\theta = \Theta e^{-K\rho}$. One of the solutions for K, called K_-, is used to define the length of the tail

$$l_T = \frac{1}{|K_-|}, \tag{7.6}$$

which is another measure of the size of Skyrmions. In some cases, K_- has an imaginary part, which indicates the tails are oscillating in addition to the exponential decay, but we will omit oscillations below despite its existence in some cases.

7.2.1.1 Ferromagnet

For ferromagnet, the lengths of the Skyrmion tails are:

1. $\bar{l}_H \ll q^{-1} \ll \xi_f$: $l_T \approx \bar{l}_H$.

2. $\bar{l}_H \ll \xi_f \ll q^{-1}$ and $\xi_f \ll \bar{l}_H \ll q^{-1}$: $l_T \approx \bar{l}_H$.

For both cases, the tails has a length $l_T \sim H^{-\frac{1}{2}}$ as in Eq. (2.12c). We expect this because the transverse fluctuations of ferromagnet have the spectrum schematically in the form of $\omega(\mathbf{k}) = k^2 + H$, as in Eq. (4.3).

7.2.1.2 Paramagnet

For paramagnet, the lengths of the tails are:

1. $\bar{l}_H \ll q^{-1} \ll \xi_p$: $l_T \approx \bar{l}_H$.

2. $\xi_p \ll q^{-1} \ll \bar{l}_H$: $l_T \approx \xi_p$.

3. $\xi_p \lesssim q^{-1}$ and small H: $l_T \approx \xi_h$.

4. Along $H \approx H_{c2}$: $l_T \approx \frac{\sqrt{2}}{\kappa_-}$,

where for the fourth case,

$$\kappa_\pm = \sqrt{q\sqrt{q^2 + \frac{2}{\xi_h'^2}} \pm \left(q^2 - \frac{1}{\xi_h'^2}\right)}. \tag{7.7}$$

The first case corresponds to the the paramagnet with large magnetic field and the boundary with ferromagnet, where $\bar{l}_H$ is given by Eq. (2.12a). The second case refers to the paramagnet far away from the transition points, making $l_T \approx \xi_p$. The third case refers to the paramagnet very close to the helimagnetic transition point, making $l_T \approx \xi_h$.

The fourth case refers to the paramagnet along $H \approx H_{c2}$, the critical field in Eq. (3.11). The Skyrmion lattice is formed along part of this critical line.

7.2.2 Aligned Conical Phase

By Goldstone theorem and linear response, any perturbation in the conical phase shows long distance algebraic decay. Therefore, a Skyrmion in this phase shows a long tail. For illustrative purpose, we study the ferromagnet without magnetic field and DM interaction which breaks the rotational symmetry.

7.2.2.1 Ferromagnet without external magnetic field and DM interaction

The spectrum of the Goldstone modes in ferromagnet in $H = 0$ and $q = 0$ is $\omega(\mathbf{k}) = k^2$, [71] and the modes are readily diagonalized as δm_x and δm_y. As a result, they behaves $|\mathbf{r}|^{-1}$, as illustrated in Appendix C. We expect the Skyrmion tail to behave in the same way.

We still employ the perturbation schemes in Eqs. (7.5) for this ferromagnet with $H = 0$ and $q = 0$. The differential equations kept to the relevant order is given as

$$\frac{\partial^2 \delta m}{\partial \rho^2} + \frac{1}{\rho}\frac{\partial \delta m}{\partial \rho} - M_F^{(0)} \left(\frac{\partial \delta\theta}{\partial \rho}\right)^2 - \frac{M_F^{(0)}}{\rho^2}(\delta\theta)^2 = \frac{\delta m}{\xi_f^2}, \tag{7.8a}$$

$$\frac{\partial^2 \delta\theta}{\partial \rho} + \frac{1}{\rho}\frac{\partial \delta\theta}{\partial \rho} - \frac{1}{\rho^2}\delta\theta = 0. \tag{7.8b}$$

From an analysis of the differential equations, Eqs. (6.11), we get

$$\delta\theta = \frac{\Theta_f}{\rho}, \tag{7.9a}$$

$$\delta m = -2\xi_f^2 M_F^{(0)} \frac{\Theta_f^2}{\rho^4}. \tag{7.9b}$$

From Eq. (7.8b), we know that the coefficients Θ_f is arbitary, as in core solution the coefficients in Eq. (7.4) in Section 7.1.2 is undetermined as well. It is the result of the equation for the fluctuations given by a Laplace equation for a symmetry-breaking ferromagnet. $\delta m(\rho)$ and $\delta\theta(\rho)$ can be expressed in the scaling form $f\left(\frac{\xi_f^2}{L^2}, \frac{\rho}{L}\right)$, for some length scale L. Moreover, the approximation in Eq. (6.6) far from the Skyrmion core in the non-linear σ model has the same behavior.

Similarly, as in the Skyrmion core, the coefficients can be fixed by additional interactions that carry other length scales as discussed in Section 7.1.2. To fix the Skyrmion size, these interactions have to change the symmetries of the system such that the ferromagnet is no longer a phase of spontaneous symmetry breaking. Examples include cubic anisotropy, magnetic field, longitudinal stiffness etc. However, interactions such as DM interaction cannot fix the Skyrmion size because it removes the merely spatial inversion symmetry but the ferromagnet remains to be symmetry-breaking. [1]

7.2.2.2 Aligned conical phase

While the ferromagnet has the readily diagonalized Goldstone modes with spectrum $\omega(\mathbf{k}) = k^2$, the aligned conical phase has the Goldstone modes given by Eqs. (4.9), similar to that of the cholesteric liquid crystal. [43] For zero magnetic

[1] This can be confirmed by analyzing Eq. (6.11b) for $c \neq 0$ and $H = 0$ asymtotically and numerically. For both $\rho \to 0$ and $\rho \to \infty$, terms with coefficient a vanish, and terms with coefficient c alone cannot fix the Skyrmion core size and tail length. The numerical analysis is also disastrous because the solution is sensitive to step and system sizes.

field makes, the second term vanishes. [44] For the parametrization of fluctuations about the conical phase can be written as in Eq. (4.6). The Goldstone mode that corresponds to Eq. (4.9) is given by the "diagonalized" form as

$$\begin{aligned}
& \delta m_G(\mathbf{x}) \\
\approx\ & \phi_0(\mathbf{x}) - \frac{q^2+\xi_h'^{-2}\left[1-\left(\frac{H}{H_{c2}}\right)^2\right]}{q(q^2+\xi_h'^{-2})}\frac{\partial\varphi_+(\mathbf{x})}{\partial y} + \frac{q^2+\xi_h'^{-2}\left[1-\left(\frac{H}{H_{c2}}\right)^2\right]}{q(q^2+\xi_h'^{-2})}\frac{\partial\varphi_-(\mathbf{x})}{\partial x} \\
& -\frac{\xi_h'^{-2}\left[1-\left(\frac{H}{H_{c2}}\right)^2\right]}{q(q^2+\xi_h'^{-2})}\frac{\partial\pi_1(\mathbf{x})}{\partial x} + \frac{\xi_h'^{-2}\left[1-\left(\frac{H}{H_{c2}}\right)^2\right]}{q(q^2+\xi_h'^{-2})}\frac{\partial\pi_2(\mathbf{x})}{\partial y},
\end{aligned} \tag{7.10}$$

which satisfies the partial differential equation

$$\left[\frac{\partial^2}{\partial z^2} + \frac{\xi_h'^{-2}}{q^2+\xi_h'^{-2}}\left(\frac{H}{H_{c2}}\right)^2\nabla_\perp^2\right]\delta m_G(\mathbf{x}) \approx 0, \tag{7.11}$$

for $H \neq 0$. Eq. (7.11) has a solution

$$\delta m_G(\mathbf{x}) = \frac{A}{\rho}\sin(\varphi + B), \tag{7.12}$$

with undetermined coefficients A and B. (Note that the Skyrmion core in conical phase has arbitrary size R and goes like $\rho\sin(\varphi + B)$ for the same argument.) Therefore, similar to ferromagnets, the Skyrmion tail in the conical phase has a power law form. A detailed analysis of the saddle-point equations, Eqs. (6.13), shows that Skyrmion tail in the conical phase goes like $\rho^{-1}\sin\xi$, where ξ is defined in Eq. (D.17), with arbitrary coefficients.

7.3 Core size as the matching distance between core behavior and Skyrmion tail

The definition of R in Section 7.1.1 deals only with the core behavior. Here we introduce a new distance L, which is defined as tbe distance where the core behavior and tail of the Skyrmion meet. By finding L, we consider both the core and the tail of the Skyrmion, as shown in Fig. 7.2. In some cases, R and L are not too different in terms of order of magnitudes, but their difference becomes greater when the magnetic field becomes large.

In the following cases, we match the core behavior and the tail at a point L, and then we solve for L.

7.3.1 Paramagnet and ferromagnet

For paramagnet and ferromagnet, by matching the core behavior in Section 7.1 and the tail in Section 7.2, we solve for the matching point L tabulated in Table 7.1. We verify that for all cases in Table 7.1 have winding number $W = -1$, by putting the solutions of $\theta(\mathbf{x})$ back to Eq. (6.8).

From Table 7.1, we can see that R's are mostly of the order of magnitude of q^{-1}, and l_T's are mostly the thermal correlation lengths. However, L shows much more complicated dependence on the various length scales. l_T is generally not a good measure of a Skyrmion size because the correlation length is related to the thermodynamic phase of the bulk, the size of an additional object. Both R and L is of the order of magnitude of q^{-1} near the helimagnetic transition point at $H \approx 0$,

Table 7.1: Isolated Skyrmions in ferromagnets and paramagnets in different regions of the phase diagram in Fig. 7.1. (PM = paramagnet, FM = ferromagnet)

PM/FM	Region in Phase Diagram	l_T	R	L
FM	$\xi_f \ll q^{-1} \ll \bar{l}_H$	$\bar{l}_H$	$2\pi q\bar{l}_H^2$	$\sqrt{32\pi q^3\bar{l}_H^3}\xi_f$
FM	$\xi_f \ll \bar{l}_H \ll q^{-1}$	$\bar{l}_H$	$\frac{\pi}{2q}$	$\sqrt{4\pi q\bar{l}_H}\xi_f$
FM	$\bar{l}_H \ll \xi_f \ll q^{-1}$	$\bar{l}_H$	$\frac{\pi}{2q}$	$\sqrt{2\pi q\bar{l}_H}\bar{l}_H$
FM	$\bar{l}_H \ll q^{-1} \ll \xi_f$	$\bar{l}_H$	$\frac{\pi}{2q}$	$\sqrt{2\pi q\bar{l}_H}\bar{l}_H$
PM	$\xi_p \ll q^{-1} \ll \bar{l}_H$	ξ_p	$\frac{\pi}{2q}$	$\frac{[2\pi(q\xi_p)^2]^{\frac{1}{3}}}{q}$
PM	$q^{-1} \ll \bar{l}_H \ll \xi_p$	$q^{-2}\bar{l}_H^{-1}$	$2\pi q\bar{l}_H^2$	$2\pi q\bar{l}_H^2$
PM	$\bar{l}_H \ll q^{-1} \ll \xi_p$	$\bar{l}_H$	$\frac{\pi}{2q}$	$\sqrt{2\pi q\bar{l}_H}\bar{l}_H$
PM	$\xi_p \lesssim q^{-1}$	ξ_h	$\frac{5\pi}{2q}$	$1.48q^{-1}$
PM	Along $H \approx H_{c2}$	$\frac{\sqrt{2}}{\kappa_-}$	$\frac{5\pi}{2q}$	$\frac{\pi}{\sqrt{2}\kappa_+}$

indicating that the Skyrmion size is of q^{-1} in this region. Far from this point, L and R differs in orders of magnitude. In general, L is better to characterize the size of Skyrmions because it takes into account both the core and the tail. Whether L or R is a better measure depends on the situations, as listed below:

1. If L and R are of the same order of magnitude ($\sim K^{-1}$ or oscillating) as in Fig. 7.3 (a), they are equally good. Examples: paramagnets in $q^{-1} \ll \bar{l}_H \ll \xi_p$ and $\xi_p \lesssim q^{-1}$.

2. If $R \gg L$ as in Fig. 7.3 (b), L is a better measure because L depicts where the tail starts and the slope of the core behavior was underestimated. Examples: ferromagnets in $\xi_f \ll q^{-1} \ll \bar{l}_H$, $\xi_f \ll \bar{l}_H \ll q^{-1}$, $\bar{l}_H \ll \xi_f \ll q^{-1}$ and $\bar{l}_H \ll q^{-1} \ll \xi_f$, and paramagnets in $\bar{l}_H \ll q^{-1} \ll \xi_p$ and $\xi_p \ll q^{-1} \ll \bar{l}_H$.

3. If $L \gg R$ as in Fig. 7.3 (c), R is a better measure. The matching method is not working so well because at $\rho = L$, $\theta(\rho)$ becomes negative. However, There are no such examples in all cases considered in Table 7.1.

Therefore, for our purpose, L is a better characterization of the Skyrmion size in general.

For pure ferromagnets ($q = 0$ and $H = 0$) and aligned conical phase, matching does not fix the size of the Skyrmion due to the same reason stated in Section 7.2.2. For pure ferromagnets, matching the solutions in Eq. (6.6) for small and large ρ does not give L.

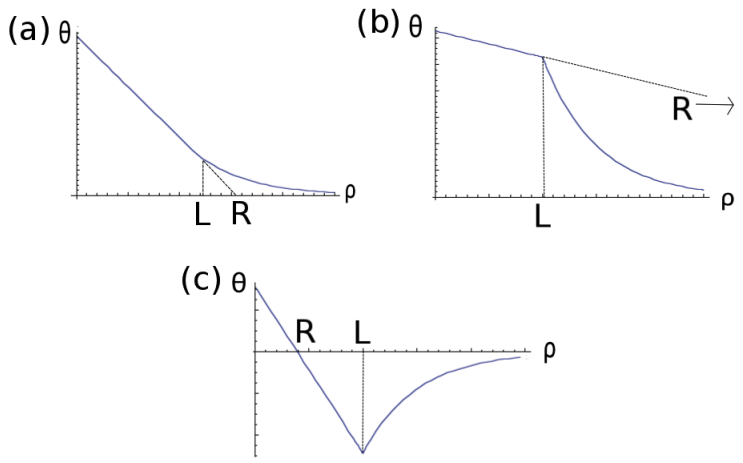

Figure 7.3: Plots for $\theta(\rho)$ for Skyrmions in paramagnets and ferromagnets, and the meanings of R and L as the sizes of the Skyrmion core. (a) $R \approx L$. Both are equally good measures for the core size. (b) $R \gg L$. L is a better measure for the core size. (c) $R \ll L$. R is a better measure for the core size.

7.4 Matching length of aligned conical phase

Because of the technical complexities of aligned conical phase, we do not match the core and tail solutions as we did for other magnets. And due to spontaneous symmetry breaking, it does not have a definite core size and tail length. However, we assume a form of Syrmionic solution here and estimate the range of the core size by matching. We describe an isolated Skyrmion in terms of

$$\begin{aligned}\mathbf{M} = [1 - \eta_1(\rho, \xi)] m_{sp} (\cos qz\hat{\mathbf{x}} + \sin qz\hat{\mathbf{y}}) \\ + m_{||} \hat{\mathbf{n}}_{sk} - \eta_3(\rho, \xi) m_{||} \hat{\mathbf{z}},\end{aligned} \tag{7.13}$$

where $\hat{\mathbf{n}}_{sk}$ is the same Skyrmion in Eqs. (6.4a-6.4c). The first and third term are with variational parameters η_1 and η_3 which does not alter the winding number. The second term with $\hat{\mathbf{n}}_{sk}$ keeps the winding number to be -1. Because Eq. (7.13)

already captures the long-range behavior as $\hat{\mathbf{n}}_{sk} \cdot (-\sin qz\hat{\mathbf{x}} + \cos qz\hat{\mathbf{y}}) \sim \frac{1}{\rho}\sin\xi$ far from the core ($\rho \to \infty$), there is no term in the direction of $(-\sin qz\hat{\mathbf{x}} + \cos qz\hat{\mathbf{y}})$ in Eq. (7.13).

We then solve for η_1 and η_3 by putting Eq. (7.13) to the saddle-point equations, Eqs. (6.13), for regions far from the core ($\rho \to \infty$) and near the core ($\rho \approx 0$). Far from the core ($\rho \to \infty$), we find that

$$\eta_1 \approx \frac{(3aq^2 - 2r)m_{||}}{2um_{sp}^3}\left(\frac{2l}{\rho}\sin\xi\right), \tag{7.14}$$

$$\eta_3 \approx -\frac{m_{||}}{m_{sp}}\left(\frac{2l}{\rho}\sin\xi\right), \tag{7.15}$$

where l is an undetermined parameter that we estimate below. At the core ($\rho \approx 0$), with linearization of the parameters in the saddle-point equations, Eqs. (6.13), we find that

$$\eta_1 \approx -E_1\left(\frac{2\rho}{l}\sin\xi\right), \tag{7.16}$$

$$\eta_3 \approx 1 - B_3\left(\frac{\rho}{l}\right)^2 - E_3\left(\frac{2\rho}{l}\sin\xi\right), \tag{7.17}$$

where (in terms of bare parameters in the action)

$$
\begin{aligned}
E_1 &= \frac{\left[r(1-lq)+\frac{4a}{l^2}(2-q^2l^2)\right]m_{||}}{r-\frac{2aq}{l}+u(3m_{sp}^2+4m_{||}^2)} \\
&\quad -\frac{2u(m_{||}^2-2m_{sp}^2)m_{||}m_{sp}^2}{(7m_{||}^2-4m_{sp}^2)\left[r-\frac{2aq}{l}+u(3m_{sp}^2+4m_{||}^2)\right]} \\
&\quad -\frac{uql(28m_{||}^5-23m_{||}^3m_{sp}^2+4m_{||}m_{sp}^4)}{(7m_{||}^2-4m_{sp}^2)\left[r-\frac{2aq}{l}+u(3m_{sp}^2+4m_{||}^2)\right]}, \qquad (7.18) \\
B_3 &= \frac{4qlm_{sp}^2}{7m_{||}^2-4m_{sp}^2} \\
&\quad +\frac{l^2\left(\frac{4a}{l^2}-\frac{4aq}{l}+r-4um_{||}^2+um_{sp}^2\right)}{2a}, \qquad (7.19) \\
E_3 &= \frac{4m_{||}m_{sp}}{7m_{||}^2-4m_{sp}^2}. \qquad (7.20)
\end{aligned}
$$

Then we match Eq. (7.14) and Eq. (7.16), and η_3 by matching Eq. (7.15) and Eq. (7.17) at some distance $\rho = L$, and we can solve for l. Matching is only possible if B_3 and E_3 are positive, and E_1 is negative. For E_3 to be positive, the denominator $7m_{||}^2 - 4m_{sp}^2$ has to be positive. (This makes the Skyrmion gas to appear only if $H \geq 0.798H_{c2}$.) L depends on ξ slightly. The lack of an analytic solution forces us to explore the core size numerically.

In Table 7.2, the sizes of Skyrmions in the aligned conical phase with different values of the correlation length ξ_h' and $H = 0.8H_{c2}$ are listed. L is the size of a Skyrmion found by matching method. It depends on the phase angle ξ but it does not vary significantly. In general, as the system goes away from the phase boundary (as ξ_h' decreases), the size of the Skyrmion decreases.

Table 7.2: Isolated Skyrmions in aligned conical phase for different values of ξ'_h all for $H = 0.8H_{c2}$.

ξ'_h	l	L	$\xi = qz - \varphi$
$3.16q^{-1}$ $(r = 0.7aq^2)$	$1.59q^{-1}$	$2.38q^{-1}$	0
	$1.59q^{-1}$	$2.31q^{-1}$	$\frac{\pi}{2}$
	$1.59q^{-1}$	$2.38q^{-1}$	π
	$1.58q^{-1}$	$2.24q^{-1}$	$\frac{3\pi}{2}$
$1.83q^{-1}$ $(r = 0.7aq^2)$	$1.13q^{-1}$	$2.13q^{-1}$	0
	$1.13q^{-1}$	$1.88q^{-1}$	$\frac{\pi}{2}$
	$1.13q^{-1}$	$2.13q^{-1}$	π
	$1.12q^{-1}$	$1.38q^{-1}$	$\frac{3\pi}{2}$
$1.41q^{-1}$ $(r = 0.5aq^2)$	$0.88q^{-1}$	$1.35q^{-1}$	0
	$0.88q^{-1}$	$1.29q^{-1}$	$\frac{\pi}{2}$
	$0.88q^{-1}$	$1.35q^{-1}$	π
	$0.88q^{-1}$	$1.23q^{-1}$	$\frac{3\pi}{2}$
$1.29q^{-1}$ $(r = 0.4aq^2)$	$0.79q^{-1}$	$1.13q^{-1}$	0
	$0.79q^{-1}$	$1.15q^{-1}$	$\frac{\pi}{2}$
	$0.79q^{-1}$	$1.13q^{-1}$	π
	$0.80q^{-1}$	$1.20q^{-1}$	$\frac{3\pi}{2}$

7.5 Core-to-core distance of a Skyrmion lattice

Lastly, we discuss the core-to-core distance as a kind of characterization of the Skyrmion size in the columnar phase with the Abrikosov solution given in Section 3.3.2.

With the solution given in Section 3.3.1, the core-to-core distance is q^{-1}. However, it is not the case for the Abrikosov solution given in Section 3.3.2. Near the helimagnetic phase boundary $\xi_p q \approx 1$, as in Eq. (2.10), and in this region the core-to-core distance goes like q^{-1}, agreeing with previous theoretical [64, 77, 69, 33, 68] and experimental studies. [8, 26]. Both description in Sections 3.3.1 and 3.3.2 are good. However, further away from the phase boundary, from Eq. (3.24), the core-to-core distance is $\sim q\xi_p^2$. However, we also predict that the size increases away from the phase boundary, provided the Skyrmion lattice is still the thermodynamic ground state when the correlation length ξ_p gets larger.

7.6 Conclusion

In this chapter, we evaluated the sizes of a single Skyrmion as excitations by defining them from their core and tail behaviors in various phases in helimagnets.

In phases without spontaneous symmetry breaking, the sizes are the competition of various physical length scales in the system, contrary to the belief that the sizes depend merely on the strength of DM interaction.

In phases with symmetry breaking, the sizes are undetermined. More physical length scales or matching the core and tail are needed. An example for latter is the

conical phase, where in our study the size is fixed by imposing one more matching constraint in our problem.

We also discussed about the core-to-core distance of the Skyrmion lattice. It is of the order of q^{-1} near the transition temperature, as shown in various experiments. Our result shows that it increases as the system further decreases its temperature.

Chapter 8

Conclusion and Outlook

We first present a summary of our findings as a conclusion to the dissertation and then discuss open problems that can be pursued in the future. In Chapter 1, we introduced the concept of helimagnetism, and reviewed a number of experimental findings about typical helimagnets such as MnSi, FeGe and $Fe_{1-x}Co_xSi$. In Chapter 2, we introduced the LGW model appropriate for these helimagnets, and the associated energy scales (in terms of the hierarchy of the order of spin-orbit coupling) and the physical length scales. In Chapter 3, we presented the phase diagram realized by our model using mean-field theory. Our model gives the helical, conical, columnar, paramagnetic and ferromagnetic phases, those measured by experiments. We also predicted a new elliptical conical phase between the helical and conical phases. In Chapter 4, we studied the Goldstone modes of various phases by perturbation, and compared these with the fluctuations in liquid crystals. In Chapter 5, we studied the effects of the Goldstone modes on specific heat, thermal conductivity and electrical resistivity by considering a microscopic model of helimagnets with coupling between the Goldstone modes and the conduction electrons. We considered the properties in both clean and ballistic disorder limits. We deduced the $T^{3/2}$-dependence of the resistivity in the NFL phase found in the experiment, and predicted the dependences in other ordered phases. In Chapter 6, we reviewed

the basis of Skyrmions. In Chapter 7, we studied the sizes of Skyrmions through analyzing the saddle-point equations. We found that the sizes of Skyrmions depend not only on helical wavelength, but also other physical length scales permitted by the system.

We now discuss open problems as possible future projects that extend the work in this dissertation. Firstly, further studies are needed to understand the NFL phase at $p > p_c$. This, called the blue quantum flog, is the helimagnetic analog of blue phase in cholestoric liquid crystals. [88] The columnar fluctuations in columnar phase and its consequences on electrical resisitivity in the presence of disorder already shed light on the understanding of NFL phase. It is believed that this NFL phase is the melted columnar crystal, (as in Ref. [56]) which needs verification experimentally and theoretically.

Secondly, the Goldstone boson in the helical phases of helimagnets is called a helimagnon, and the Goldstone modes in the columnar phase are called Skyrmionians. We can study the interaction between the conducting electrons, helimagnons and columns of Skyrmions. This will advance our understanding about the formation of columnar lattice, its transport behavior in the phase of Skyrmion lattice, and the dynamics of Skyrmions in helimagnets. The lattice may melt into a liquid. [56] The columns are moving freely like particles, as in vortices in high-temperature superconductors [113] and two-dimensional superfluids. [114, 115] They are formed by crossing the energy barrier due to different topologies, just like vortices in two-dimensional Bose gas. [116] Skyrmions are magnetic vortices, with their dynamics that is still yet to explore. [117] The dynamics is also related to the interac-

tions between these Skyrmions, Goldstone bosons and conduction electrons, just like electron-phonon interactions. [99]

Thirdly, we can study the helimagnet with pitch vector perpendicular to the external magnetic field. Such a helimagnet was proposed as a candidate for the columnar phase before the discovery of the six-fold neutron scattering pattern, [76] and its electronic properties were analyzed in our paper [48] as well. This is possible if the longitudinal magnetic susceptibility is larger than the transverse one, while in aligned conical phase it is the opposite, as in cholestoric liquid crystals. [24] The helical period increases as the magnetic field increases until the helix is unwound. [78]

Lastly, we can study the dynamics of the formation of ordered phases in helimagnets. Suppose that there is a quench in the system (sudden change of temperature or magnetic field), or a slow decrease of temperature across the phase transition, as in Kibble-Zurek (KZ) mechanism. [118, 119, 120, 121] We expect that the magnet evolves to the thermodynamically stable phase. However, because the helimagnet has a softer Goldstone modes than ferromagnets, we expect the formation of ordered phases in helimagnets be different from that of ferromagnets (with domain size grows as $t^{\frac{1}{2}}$, where t is the time). The dynamics of the formation or growth of the new magnetic order can be studied with a time-dependent equation for magnets. [71] If the quenching occurs at absolute zero, the dynamics of the growth of the new ordered can be studied with influence functional. [122]

Appendix A

Analytic Expressions for the Paramagnet and the Ferromagnet in Mean-field LGW Model

For the paramagnet and the ferromagnet, the magnetization can be solved by the saddle-point equation derived from LGW functional,

$$rm + um^3 - H = 0. \tag{A.1}$$

Its analytic solutions are given in the following.

A.1 Paramagnet

The paramagnet phase is only valid for $r > 0$. Its full analytic expression is given by

$$M_P = \frac{H}{r} f_1\left(\sqrt{\frac{u}{r^3}}H\right), \tag{A.2a}$$

where

$$f_1(x) = \frac{1}{x}\left[\frac{x}{2} + \sqrt{\frac{1}{27} + \left(\frac{x}{2}\right)^2}\right]^{\frac{1}{3}} + \frac{1}{x}\left[\frac{x}{2} - \sqrt{\frac{1}{27} + \left(\frac{x}{2}\right)^2}\right]^{\frac{1}{3}}. \tag{A.2b}$$

A Taylor's expansion for small H confirms that $M_p \approx \chi_p H$, where $\chi_p = \frac{1}{r}$. However, when r approaches 0, $M_p \approx \left(\frac{H}{u}\right)^{\frac{1}{3}}$, giving the critical exponent $\delta = 3$ for the mean-field theory. [71]

A.2 Ferromagnet

The ferromagnet is valid only for $r < 0$. In general the magnetization is given by

$$M_F = \begin{cases} M_F^{(0)} \left(\cos\frac{\gamma}{3} + \frac{1}{\sqrt{3}} \sin\frac{\gamma}{3} \right), & \text{for } H < \frac{2|r|}{\sqrt{27}} \sqrt{\frac{|r|}{u}} \\ \frac{H}{|r|} f_2 \left(\sqrt{\frac{u}{|r|^3}} H \right), & \text{for } H > \frac{2|r|}{\sqrt{27}} \sqrt{\frac{|r|}{u}} \end{cases} \tag{A.3a}$$

where $M_F^{(0)}$ is given by

$$M_F^{(0)} = \sqrt{\frac{|r|}{u}}, \tag{A.3b}$$

$$f_2(x) = \frac{1}{x} \left[\frac{x}{2} + \sqrt{-\frac{1}{27} + \left(\frac{x}{2}\right)^2} \right]^{\frac{1}{3}} + \frac{1}{x} \left[\frac{x}{2} - \sqrt{-\frac{1}{27} + \left(\frac{x}{2}\right)^2} \right]^{\frac{1}{3}}. \tag{A.3c}$$

and

$$\sin\gamma = \frac{\sqrt{27}}{2|r|} \sqrt{\frac{u}{|r|}} H. \tag{A.3d}$$

A Taylor's expansion for small H confirms that $m \approx M_F^{(0)} + \chi_f H$, where $\xi_f = \frac{1}{2|r|}$.

Appendix B

Model in CP^1 Representation

B.1 Basics

To facilitate the study of topologically non-trivial Skyrmions, it is useful to write the model $\mathcal{S}_{\rm H}+\mathcal{S}_{\rm DM}$ in Eqs. (2.2a) and (2.3a) in terms of the CP^1 representation, which is commonly used in the study of quantum Hall ferromagnets. [55] We first write

$$\mathbf{M}(\mathbf{x}) = m(\mathbf{x})\mathbf{n}(\mathbf{x}), \tag{B.1}$$

where $m(\mathbf{x})$ and $\mathbf{n}(\mathbf{x})$ denotes the magnitude and direction of $\mathbf{M}(\mathbf{x})$. The direction $\mathbf{n}$ can be written in terms of two-component spin through the Hopf mapping: [123]

$$n_\alpha = z_i^* \sigma_\alpha^{ij} z_j, \tag{B.2}$$

where σ_α is the Pauli matrix. Greek indices denote spatial component and Latin indices matrix component in spins. The constraint $\mathbf{n}^2 = 1$ gives

$$z_i^* z_i = 1. \tag{B.3}$$

Because $\mathbf{n}$ has a definite magnitude, there are only two degrees of freedom. Therefore, $\mathbf{z}$ should have two degrees of freedom only, accomplished by the constraint Eq. (B.3) and fixing the gauge [68]

$$A_\alpha = -\frac{i}{2}(z_i^* \partial_\alpha z_i - z_i \partial_\alpha z_i^*), \tag{B.4}$$

such that the transformation $z_i(\mathbf{x}) \to e^{-i\theta(\mathbf{x})} z_i(\mathbf{x})$ and $z_i^*(\mathbf{x}) \to e^{i\theta(\mathbf{x})} z_i^*(\mathbf{x})$ does not lead to a change in the physical system.

In this representation, we write the action as

$$\begin{aligned} & \mathcal{S}[m, \mathbf{A}, \mathbf{z}] \\ = & \int d^3x \left[\frac{r}{2} m^2 + \frac{u}{4} m^4 + \frac{a}{2} \partial_\alpha m \partial_\alpha m - H_\alpha m z_i^* \sigma_\alpha^{ij} z_j \right] \\ & + 2am^2 \left[(\partial_\alpha z_i^*)(\partial_\alpha z_i) - A_\alpha A_\alpha \right] \\ & + cm^2 \left[z_i^* \sigma_\alpha^{ij} z_j A_\alpha + \frac{i}{2} (\partial_\alpha z_i^*) \sigma_\alpha^{ij} z_j - \frac{i}{2} z_i^* \sigma_\alpha^{ij} \partial_\alpha z_j \right]. \end{aligned} \tag{B.5}$$

The saddle-point equation associated with this representation has to be done with Lagrangian multiplier because of the constraint in Eq. (B.3). Consider $\mathcal{S} + \lambda \int d^3x (z_i^* z_i - 1)$ with λ being the Lagrangian multiplier, the saddle-point equations are

$$\begin{aligned} & (r - 3aq^2 - 4aA_\alpha A_\alpha) m - a \partial_\alpha \partial_\alpha m - 4aqmn_\alpha A_\alpha + um^3 \\ & - H_\alpha n_\alpha + 4am \left[\left(\delta_{ij} \partial_\alpha - \frac{iq}{2} \sigma_\alpha^{ij} \right) z_j^* \right] \left[\left(\delta_{ik} \partial_\alpha + \frac{iq}{2} \sigma_\alpha^{ik} \right) z_k \right] &= 0, \qquad \text{(B.6a)} \\ & m \left(\delta_{ij} \partial_\alpha - i\delta_{ij} A_\alpha + \frac{iq}{2} \sigma_\alpha^{ij} \right) \left(\delta_{jk} \partial_\alpha - i\delta_{jk} A_\alpha + \frac{iq}{2} \sigma_\alpha^{jk} \right) z_k \\ & \qquad - iqm \left(n_\alpha \partial_\alpha z_i + \frac{1}{2} z_i \partial_\alpha n_\alpha \right) + \frac{H_\alpha}{2a} \sigma_\alpha^{ij} z_j &= \lambda z_i, \qquad \text{(B.6b)} \end{aligned}$$

where $q = \frac{c}{2a}$ as in Eq. (2.5). These are convenient for studying a lattice of Skyrmions.

B.2 CP^1 representation of some phases in helimagnets

B.2.1 Ferromagnet and paramagnet

The magnitudes of ferromagnet and paramagnet can be expressed as Eqs. (A.2a) and (A.3a), with details given in Appendix A. Its direction can be given in CP^1 representation as

$$\mathbf{z} = \begin{bmatrix} 1 \\ \\ 0 \end{bmatrix}, \tag{B.7a}$$

with

$$\mathbf{A} = 0. \tag{B.7b}$$

B.2.2 Aligned conical phase

The magnitude of aligned conical phase is given by m_H in Eq. (3.10d). Its direction can be given in CP^1 representation as

$$\mathbf{z} = \begin{bmatrix} e^{-\frac{iqz}{2}}\sqrt{\frac{1}{2}\left(1+\frac{m_{||}}{m_H}\right)} \\ e^{\frac{iqz}{2}}\sqrt{\frac{1}{2}\left(1-\frac{m_{||}}{m_H}\right)} \end{bmatrix}, \tag{B.8a}$$

with

$$\mathbf{A} = \frac{qm_{||}}{2m_H}\hat{\mathbf{z}}. \tag{B.8b}$$

B.2.3 Isolated Skyrmion

The isolated Skyrmion, given as a solution of the non-linear σ model in Eqs. (6.4), can be expressed in CP^1 representation as [68]

$$\mathbf{z} = \sqrt{\frac{\rho^2}{\rho^2 + l^2}} \begin{bmatrix} e^{i\left(\frac{\pi}{2} - \varphi\right)} \\ \\ \frac{l}{\rho} \end{bmatrix}, \tag{B.9a}$$

with

$$\mathbf{A} = -\frac{\rho\hat{\varphi}}{\rho^2 + l^2}. \tag{B.9b}$$

Appendix C

Linear Response Theory

Linear response theory relates external perturbations of a physical system to the correlation functions in the unperturbed one. [97] This ensures that the perturbations have long-ranged behaviors if there exist correlation functions for massless modes for fluctuations. In contrast, the perturbations are of short-ranged if there do not exist any massless modes. This explains the behaviors of Skyrmion tails in different phases in Chapter 7 in relation to the Goldstone theorem. This appendix also briefly explains the ideas behind the calculation of transport properties in Chapter 5. Linear response theory was treated in various standard textbooks. [94, 97, 124, 125, 126]

Assume there is a field $\mathbf{M}(\mathbf{x})$ with a known mean-field solution $\mathbf{M}_0$, with the corresponding free energy per temperature being S_0. Let the kernel matrix for fluctuations be $\mathbf{K}(\mathbf{x}, \mathbf{x}')$ and an external perturbation $\mathbf{H}(\mathbf{x})$. Then the corresponding partition function is

$$\begin{aligned} Z &= e^{-S_0} \int D\mathbf{M} \cdot \\ &\quad \exp\left[- \int d^d x \int d^d x' \frac{1}{2} \delta M_i(\mathbf{x}) K_{ij}(\mathbf{x}, \mathbf{x}') \delta M_j(\mathbf{x}') \right. \\ &\quad \left. + \beta \int d^d x \cdot H_i(\mathbf{x}) \delta M_i(\mathbf{x}) \right], \end{aligned} \tag{C.1}$$

where summation is on repeated indices and $\beta = (k_B T)^{-1}$. By carrying out the functional integral, we get the fluctuation determinant. [127] The equation for δM,

by variational principle, is

$$\int d^d x' \cdot K_{ij}(\mathbf{x}, \mathbf{x}') \delta M_j(\mathbf{x}') - \beta H_i(\mathbf{x}) = 0, \tag{C.2}$$

and hence,

$$\delta M_i(\mathbf{x}) = \beta \int d^d x' \cdot K_{ij}^{-1}(\mathbf{x}, \mathbf{x}') H_j(\mathbf{x}'). \tag{C.3}$$

Note that the inverse of the kernel matrix is actually the correlation matrix. We can see from here that the perturbation $\delta\mathbf{M}(\mathbf{x})$ has the same behavior as the correlation functions $\mathbf{K}(\mathbf{x}, \mathbf{x}')$. If $K^{-1}(\mathbf{x}, \mathbf{x}') = K^{-1}(\mathbf{x} - \mathbf{x}')$, the Fourier representation of Eq. (C.3) is

$$\delta M_i(\mathbf{k}) = \beta K_{ij}^{-1}(\mathbf{k}) H_j(\mathbf{k}). \tag{C.4}$$

We illustrate this with the example of a pure ferromagnet with $q = 0$ and $H = 0$. Assume that the magnet is aligned along z direction. Then the kernel matrices (the inverse of the correlation functions) are given by [71]

$$K_{ij}(\mathbf{k}) = \delta_{ij}(ak^2 - 2r\delta_{jz}).$$

This indicates that along x and y directions, the fluctuations are massless as expected by Goldstone theorem. Along z direction, it is massive. Then, we get

$$ak^2 \delta M_x(\mathbf{k}) - \beta H_x(\mathbf{k}) = 0,$$

$$ak^2 \delta M_y(\mathbf{k}) - \beta H_y(\mathbf{k}) = 0,$$

$$(ak^2 - 2r)\delta M_z(\mathbf{k}) - \beta H_z(\mathbf{k}) = 0.$$

This gives $\delta M_x(\mathbf{x}), \delta M_y(\mathbf{x}) \sim |\mathbf{x}|^{-1}$ and $\delta M_z(\mathbf{x}) \sim |\mathbf{x}|^{-1} e^{-\frac{|\mathbf{x}|}{\xi_f}}$. Here, we have demonstrated that the correlation function of a massless mode leads to long-range behaviors

of the perturbations. Similar behavior exists in the perturbations to aligned conical phase in Section 7.2.2.

Here, we illustrate an example of a pure paramagnet with $q = 0$ and $H = 0$ here. In this case, $\mathbf{M}_0 = 0$. The kernel matrices are [71]

$$K_{ij}(\mathbf{k}) = \delta_{ij}(ak^2 - r).$$

Then

$$(ak^2 - r)\delta M_i(\mathbf{k}) - \beta H_i(\mathbf{k}) = 0,$$

for $i = x, y$ and z. This gives $\delta\mathbf{M}(\mathbf{x}) \sim |\mathbf{x}|^{-1} e^{-\frac{|\mathbf{x}|}{\xi_p}}$. Here we have demonstrated that if the correlation functions of all modes are massive, then the perturbations are short-ranged.

Appendix D

Hertz's Theory of Quantum Critical Phenomena

This appendix reviews the derivation of the Landau-Ginzburg Hamiltonian from the microscopic Hubbard Model, as shown in Hertz's article. [83] This is a theory of quantum critical phenomena.

D.1 Hubbard Model

The Hubbard model is given by

$$H = \int d^3x \cdot \hat{\psi}^\dagger_\alpha(\mathbf{x}) \left(-\frac{\nabla^2}{2m}\right) \hat{\psi}_\alpha(\mathbf{x}) + \frac{U}{2} \int d^3x \cdot \hat{\psi}^\dagger_\alpha(\mathbf{x}) \hat{\psi}^\dagger_\beta(\mathbf{x}) \hat{\psi}_\beta(\mathbf{x}) \hat{\psi}_\alpha(\mathbf{x}) \tag{D.1}$$

where $\hat{\psi}_\alpha(\mathbf{x})$ is the field operator for the electrons. Since it is a fermionic operator, by anti-commutation relation we have

$$\hat{\psi}^\dagger_\alpha(\mathbf{x}) \hat{\psi}^\dagger_\beta(\mathbf{x}) \hat{\psi}_\beta(\mathbf{x}) \hat{\psi}_\alpha(\mathbf{x}) = \hat{\psi}^\dagger_\alpha(\mathbf{x}) \hat{\psi}_\alpha(\mathbf{x}) \hat{\psi}^\dagger_\beta(\mathbf{x}) \hat{\psi}_\beta(\mathbf{x}) - \hat{\psi}^\dagger_\alpha(\mathbf{x}) \hat{\psi}_\alpha(\mathbf{x}) \tag{D.2}$$

The identity about the Pauli matrices [123]

$$\sigma^i_{\alpha\beta} \sigma^i_{\alpha'\beta'} = 2\delta_{\alpha\beta'}\delta_{\beta\alpha'} - \delta_{\alpha\beta}\delta_{\alpha'\beta'} \tag{D.3}$$

applied in (D.2) gives

$$\hat{\psi}^\dagger_\alpha(\mathbf{x}) \hat{\psi}^\dagger_\beta(\mathbf{x}) \hat{\psi}_\beta(\mathbf{x}) \hat{\psi}_\alpha(\mathbf{x}) = -\frac{1}{4} \hat{\psi}^\dagger_\alpha(\mathbf{x}) \sigma^i_{\alpha\beta} \hat{\psi}_\beta(\mathbf{x}) \hat{\psi}^\dagger_{\alpha'}(\mathbf{x}) \sigma^i_{\alpha'\beta'} \hat{\psi}_{\beta'}(\mathbf{x}) \tag{D.4}$$

As a result, the Hubbard model (D.1) can be rewritten in terms of the magnetization as

$$H = \int d^3x \cdot \hat{\psi}^\dagger_\alpha(\mathbf{x}) \left(-\frac{\nabla^2}{2m}\right) \hat{\psi}_\alpha(\mathbf{x}) - \frac{U}{8} \int d^3x \cdot \hat{\psi}^\dagger_\alpha(\mathbf{x}) \sigma^i_{\alpha\beta} \hat{\psi}_\beta(\mathbf{x}) \hat{\psi}^\dagger_{\alpha'}(\mathbf{x}) \sigma^i_{\alpha'\beta'} \hat{\psi}_{\beta'}(\mathbf{x}) \tag{D.5}$$

The quantum partition function Z is then given by

$$\begin{aligned} Z &= \int D\bar{\psi} D\psi \cdot e^{-\int_0^\beta d\tau \int d^3x \{\bar{\psi}_\alpha(\mathbf{x},\tau)\left(\frac{\partial}{\partial\tau} - \mu\right)\psi_\alpha(\mathbf{x},\tau) + H[\bar{\psi}(\mathbf{x},\tau), \psi(\mathbf{x},\tau)]\}} \\ &= \int D\bar{\psi} D\psi \cdot e^{-\int_0^\beta d\tau \int d^3x \left[\bar{\psi}_\alpha(\mathbf{x},\tau)\left(\frac{\partial}{\partial\tau} - \frac{\nabla^2}{2m} - \mu\right)\psi_\alpha(\mathbf{x},\tau) - \frac{U}{8}\bar{\psi}_\alpha(\mathbf{x},\tau)\sigma^i_{\alpha\beta}\psi_\beta(\mathbf{x},\tau)\bar{\psi}_{\alpha'}(\mathbf{x},\tau)\sigma^i_{\alpha'\beta'}\psi_{\beta'}(\mathbf{x},\tau)\right]} \end{aligned}$$

Using Hubbard-Stratonovich transformation

$$\int d\mathbf{M} \cdot e^{-\frac{1}{2}\mathbf{M}^2 + \lambda \mathbf{M} \cdot (\bar{\Phi}\sigma\psi)} \sim e^{\frac{\lambda^2}{2}(\bar{\Phi}\sigma\psi)^2} \tag{D.6}$$

the partition function can be rewritten in terms of the new Grassman variable $\mathbf{M}$:

$$\begin{aligned} Z &= \int D\bar{\psi} D\psi \cdot e^{-\int_0^\beta d\tau \int d^3x \left[\bar{\psi}_\alpha(\mathbf{x},\tau)\left(\frac{\partial}{\partial\tau} - \frac{\nabla^2}{2m} - \mu\right)\psi_\alpha(\mathbf{x},\tau)\right]} \\ &\quad \cdot \int DM \cdot e^{-\int_0^\beta d\tau \int d^3x \left[\frac{M^2(\mathbf{x},\tau)}{2} - \frac{\sqrt{U}}{2} M^i(\mathbf{x},\tau)\bar{\psi}_\alpha(\mathbf{x},\tau)\sigma^i_{\alpha\beta}\psi_\beta(\mathbf{x},\tau)\right]} \\ &= \int DM \cdot e^{-\frac{1}{2}\int_0^\beta d\tau \int d^3x \cdot M^2(\mathbf{x},\tau)} \\ &\quad \cdot \int D\psi D\bar{\psi} \cdot e^{-\int_0^\beta d\tau \int d^3x \cdot \bar{\psi}_\alpha(\mathbf{x},\tau)\left[\left(\frac{\partial}{\partial\tau} - \frac{\nabla^2}{2m} - \mu\right) - \frac{\sqrt{U}}{2} M^i(\mathbf{x},\tau)\sigma^i_{\alpha\beta}\right]\psi_\beta(\mathbf{x},\tau)} \\ &= \int DM \cdot e^{-\frac{1}{2}\int_0^\beta d\tau \int d^3x \cdot M^2(\mathbf{x},\tau)} \mathrm{Det}\left[\left(\frac{\partial}{\partial\tau} - \frac{\nabla^2}{2m} - \mu\right) - \frac{\sqrt{U}}{2} M^i \sigma^i_{\alpha\beta}\right] \end{aligned}$$

For we write the partition function in the form of the following functional integral

$$Z = \int DM \cdot e^{-\mathcal{H}[M]} \tag{D.7}$$

the functional on the exponent is then given by

$$\begin{aligned}
\mathcal{H}[M] &= \frac{1}{2}\int_0^\beta d\tau \int d^3x \cdot M^2(\mathbf{x},\tau) - \ln\left\{\mathrm{Det}\left[\left(\frac{\partial}{\partial\tau} - \frac{\nabla^2}{2m} - \mu\right) - \frac{\sqrt{U}}{2}M^i\sigma^i_{\alpha\beta}\right]\right\} \\
&= \frac{1}{2}\int_0^\beta d\tau \int d^3x \cdot M^2(\mathbf{x},\tau) - \mathrm{Tr}\left\{\ln\left[\left(\frac{\partial}{\partial\tau} - \frac{\nabla^2}{2m} - \mu\right) - \frac{\sqrt{U}}{2}M^i\sigma^i_{\alpha\beta}\right]\right\} \\
&= \frac{1}{2}\int_0^\beta d\tau \int d^3x \cdot M^2(\mathbf{x},\tau) - \mathrm{Tr}\ln\left(1 - \mathcal{G}^0\frac{\sqrt{U}}{2}M^i\sigma^i_{\alpha\beta}\right) \qquad \text{(D.8)}
\end{aligned}$$

where in the second line we use $\mathrm{Tr}\ln A = \ln\mathrm{Det}(A)$, and in the third line we invoke the definition of the non-interacting Green's function

$$(\mathcal{G}^0)^{-1} = \frac{\partial}{\partial\tau} - \frac{\nabla^2}{2m} - \mu \qquad \text{(D.9)}$$

and an additive constant term is omitted.

The next task is to expand the trace term. Using the identity

$$\ln(1-x) = -x - \frac{x^2}{2} - \frac{x^3}{3} - \frac{x^4}{4} - \ldots \qquad \text{(D.10)}$$

and the fact that the traces of an odd power of the Pauli matrices are zero, we have

$$\mathrm{Tr}\ln\left(1 - \mathcal{G}^0\frac{\sqrt{U}}{2}M^i\sigma^i_{\alpha\beta}\right) = -\frac{1}{2}\mathrm{Tr}\left(\mathcal{G}^0\frac{\sqrt{U}}{2}M^i\sigma^i_{\alpha\beta}\right)^2 - \frac{1}{4}\mathrm{Tr}\left(\mathcal{G}^0\frac{\sqrt{U}}{2}M^i\sigma^i_{\alpha\beta}\right)^4 - \ldots \qquad \text{(D.11)}$$

D.2 The ϕ^2 Term

With the identity [123]

$$\mathrm{Tr}(\sigma^i\sigma^j) = 2\delta^{ij} \qquad \text{(D.12)}$$

the second order term of the expansion (D.11) is given by

$$
\begin{aligned}
-\frac{1}{2}\mathrm{Tr}\left(\mathcal{G}^0\frac{\sqrt{U}}{2}M^i\sigma^i\right)^2 &= -\frac{U}{8}\mathrm{Tr}\left(\mathcal{G}^0M^i\mathcal{G}^0M^j\sigma^i\sigma^j\right) = -\frac{U}{4}\mathrm{Tr}\left(\mathcal{G}^0M^i\mathcal{G}^0M^i\right) \\
&= -\frac{U}{4}\int d^3x_1\int_0^\beta d\tau_1\int d^3x_2\int_0^\beta d\tau_2 \\
&\quad \mathcal{G}^0(\mathbf{x}_1-\mathbf{x}_2,\tau_1-\tau_2)M^i(\mathbf{x}_2,\tau_2)\mathcal{G}^0(\mathbf{x}_2-\mathbf{x}_1,\tau_2-\tau_1)M^i(\mathbf{x}_1,\tau_1) \\
&= -\frac{1}{(2\pi)^6\beta^2}\frac{U}{4}\int d^3k_1\sum_{n_1=-\infty}^{\infty}\int d^3k_2\sum_{n_2=-\infty}^{\infty} \\
&\quad \mathcal{G}^0(\mathbf{k}_1,\omega_{n_1})M^i(\mathbf{k}_2,\omega_{n_2})\mathcal{G}^0(\mathbf{k}_1-\mathbf{k}_2,\omega_{n_1}-\omega_{n_2})M^i(-\mathbf{k}_2,-\omega_{n_2}) \\
&= -\frac{1}{(2\pi)^3\beta}\frac{U}{4}\int d^3k\sum_{n=-\infty}^{\infty}|M(\mathbf{k},\omega_n)|^2\Gamma(\mathbf{k},\omega_n)
\end{aligned}
$$

Fourier transform has been carried out. The bosonic Matsubara frequency ω_n is given by

$$\omega_n = \frac{2n\pi}{\beta} \tag{D.13}$$

for any integers n. The function $\Gamma(\mathbf{k},\omega_n)$ is given by the integral

$$
\begin{aligned}
\Gamma(\mathbf{k},\omega_n) &= \frac{1}{(2\pi)^3\beta}\int d^3k'\sum_{n'=-\infty}^{\infty}\mathcal{G}^0(\mathbf{k}',\omega_{n'})\mathcal{G}^0(\mathbf{k}'-\mathbf{k},\omega_n-\omega_{n'}) \qquad \text{(D.14)} \\
&= \frac{1}{(2\pi)^3\beta}\int d^3k'\sum_{n'=-\infty}^{\infty}\frac{1}{i\omega_{n'}-\left(\frac{\mathbf{k}'^2}{2m}-\mu\right)}\frac{1}{i(\omega_{n'}-\omega_n)-\left[\frac{(\mathbf{k}'-\mathbf{k})^2}{2m}-\mu\right]}
\end{aligned}
$$

where the frequency $\omega_{n'}$ in the summation is fermionic and is given by

$$\omega_{n'} = \frac{(2n'+1)\pi}{\beta} \tag{D.15}$$

We first carry out the frequency summation. Consider the contour C which is circular, centered at origin and with radius tending to infinity.

$$\begin{aligned}
0 &= \oint_C \frac{dz}{2\pi i}\frac{1}{e^{\beta z}+1}\frac{1}{z-\left(\frac{\mathbf{k}'^2}{2m}-\mu\right)}\frac{1}{(z-i\omega_n)-\left[\frac{(\mathbf{k}'-\mathbf{k})^2}{2m}-\mu\right]} \\
&= \frac{1}{e^{\beta\left(\frac{(\mathbf{k}'-\mathbf{k})^2}{2m}-\mu+i\omega_n\right)}+1}\cdot\frac{1}{i\omega_n+\frac{(\mathbf{k}'-\mathbf{k})^2}{2m}-\frac{\mathbf{k}'^2}{2m}} \\
&\quad -\frac{1}{e^{\beta\left(\frac{\mathbf{k}'^2}{2m}-\mu\right)}+1}\cdot\frac{1}{i\omega_n+\frac{(\mathbf{k}'-\mathbf{k})^2}{2m}-\frac{k'^2}{2m}} \\
&\quad -\frac{1}{\beta}\sum_{n'=-\infty}^{\infty}\frac{1}{i\omega_{n'}-\left(\frac{\mathbf{k}'^2}{2m}-\mu\right)}\cdot\frac{1}{i(\omega_{n'}-\omega_n)-\left[\frac{(\mathbf{k}'-\mathbf{k})^2}{2m}-\mu\right]}
\end{aligned}$$

$$\frac{1}{\beta}\sum_{n'=-\infty}^{\infty}\frac{1}{i\omega_{n'}-\left(\frac{\mathbf{k}'^2}{2m}-\mu\right)}\cdot\frac{1}{i(\omega_{n'}-\omega_n)-\left[\frac{(\mathbf{k}'-\mathbf{k})^2}{2m}-\mu\right]}=\frac{n_F(\xi_{\mathbf{k}'-\mathbf{k}})-n_F(\xi_{\mathbf{k}'})}{i\omega_n+\xi_{\mathbf{k}'-\mathbf{k}}-\xi_{\mathbf{k}'}} \tag{D.16}$$

where

$$\xi_{\mathbf{k}}=\frac{\mathbf{k}^2}{2m}-\mu \tag{D.17}$$

and the Fermi distribution function is

$$n_F(\xi_{\mathbf{k}})=\frac{1}{e^{\beta\xi_{\mathbf{k}}}+1} \tag{D.18}$$

As a result, the function $\Gamma(\mathbf{k},\omega_n)$ is given by

$$\Gamma(\mathbf{k},\omega_n)=\int\frac{d^3k'}{(2\pi)^3}\cdot\frac{n_F(\xi_{\mathbf{k}'-\mathbf{k}})-n_F(\xi_{\mathbf{k}'})}{\xi_{\mathbf{k}'-\mathbf{k}}-\xi_{\mathbf{k}'}+i\omega_n} \tag{D.19}$$

To evaluate this function, consider the following expression for susceptibility

$$\chi_0^R(\mathbf{k},\omega+i\eta)=\int\frac{d^3k'}{(2\pi)^3}\cdot\frac{n_F(\xi_{\mathbf{k}'-\mathbf{k}})-n_F(\xi_{\mathbf{k}'})}{\xi_{\mathbf{k}'-\mathbf{k}}-\xi_{\mathbf{k}'}-\omega-i\eta} \tag{D.20}$$

This is the famous Lindhard function that the result of the integral can be found in any textbook. Its real part is given by [105]

$$\mathrm{Re}\,\chi_0^R(\mathbf{k},\omega+i\eta)=-d(\epsilon_F)\left(\frac{1}{2}+\frac{f(x,x_0)+f(x,-x_0)}{8x}\right) \tag{D.21}$$

where $x = \frac{k}{2k_F}$ and $x_0 = \frac{\omega}{4\epsilon_F}$. The density of states is given by

$$d(\epsilon_F) = \frac{1}{2\pi^2}(2m)^{\frac{3}{2}}{\epsilon_F}^{\frac{1}{2}} \tag{D.22}$$

and the function $f(x, x_0)$ is

$$f(x, x_0) = \left[1 - \left(\frac{x_0}{x} - x\right)^2\right] \ln\left|\frac{x + x^2 - x_0}{x - x^2 + x_0}\right| \tag{D.23}$$

The imaginary part is given by [105]

$$\mathrm{Im}\,\chi_0^R(\mathbf{k}, \omega) = -\frac{d(\epsilon_F)}{2} \begin{cases} \frac{\pi}{8x}\left[1 - \left(\frac{x_0}{x} - x\right)^2\right] & \text{for } |x - x^2| < x_0 < x + x^2 \\ \frac{\pi x_0}{2x} & \text{for } 0 < x_0 < x - x^2 \\ 0 & \text{for other } x_0 >= 0 \end{cases} \tag{D.24}$$

For long-wavelength approximation, we can expand the functions for small x and $\frac{x_0}{x}$,

$$\begin{aligned} \ln\left|\frac{x + x^2 - x_0}{x - x^2 + x_0}\right| &= \ln\left|\frac{1 + x - \frac{x_0}{x}}{1 - x + \frac{x_0}{x}}\right| \\ &\approx 2\left(x - \frac{x_0}{x}\right) + \frac{2}{3}\left(x - \frac{x_0}{x}\right)^3 + \ldots \\ f(x, x_0) &\approx 2\left[1 - \left(x - \frac{x_0}{x}\right)^2\right]\left(x - \frac{x_0}{x}\right) + \ldots \\ f(x, -x_0) &\approx 2\left[1 - \left(x + \frac{x_0}{x}\right)^2\right]\left(x + \frac{x_0}{x}\right) + \ldots \\ f(x, x_0) + f(x, -x_0) &\approx 4x - 2\left(x - \frac{x_0}{x}\right)^3 - 2\left(x + \frac{x_0}{x}\right)^3 = 4x - \frac{12{x_0}^2}{x} - 4x^3 \\ \frac{f(x, x_0) + f(x, -x_0)}{8x} &\approx \frac{1}{2} - \frac{x^2}{2} - \frac{3}{2}\frac{{x_0}^2}{x^2} \approx \frac{1}{2} - \frac{x^2}{2} \end{aligned}$$

As a result, the real and the imaginary parts of the Lindhard function (D.17) is given by

$$\mathrm{Re}\,\chi_0^R(\mathbf{k}, \omega) \approx -d(\epsilon_F)\left(1 - \frac{x^2}{2}\right) \tag{D.25}$$

$$\mathrm{Im}\,\chi_0^R(\mathbf{k}, \omega) \approx -d(\epsilon_F)\frac{\pi x_0}{4x} \tag{D.26}$$

Substituting the expressions for x and x_0, we get the total Lindhard function under long-wavelength approximation as

$$\begin{aligned}\chi_0^R(\mathbf{k},\omega) &\approx -d(\epsilon_F)\left(1-\frac{x^2}{2}+i\frac{\pi x_0}{4x}\right)\\ &= -\frac{(2m)^{\frac{3}{2}}}{2\pi^2}{\epsilon_F}^{\frac{1}{2}}\left(1-\frac{k^2}{8{k_F}^2}+i\frac{\pi m}{4k_F}\cdot\frac{\omega}{k}\right)\end{aligned} \tag{D.27}$$

By the analytic continuation $i\omega_n \to \omega + i\eta$, the long-wavelength approximation for $\Gamma(\mathbf{k},\omega_n)$ is given by

$$\Gamma(\mathbf{k},\omega_n) \approx -\frac{(2m)^{\frac{3}{2}}}{2\pi^2}{\epsilon_F}^{\frac{1}{2}}\left(1-\frac{1}{2}\left(\frac{k}{2k_F}\right)^2-\frac{\pi m}{4k_F}\frac{|\omega_n|}{k}\right) \tag{D.28}$$

Putting (D.28) back to (D.11) and (D.8), we know that the ψ^2 is

$$\mathcal{H}^{(2)}[M] \approx \int \frac{d^3k}{(2\pi)^3\beta}\sum_{n=-\infty}^{\infty}\left\{\left[\frac{1}{2}-\frac{(2m)^{\frac{3}{2}}}{2(2\pi)^2}{\epsilon_F}^{\frac{1}{2}}U\right]+\frac{(2m)^{\frac{3}{2}}}{4(2\pi)^2}{\epsilon_F}^{\frac{1}{2}}U\left(\frac{k}{2k_F}\right)^2+\frac{(2m)^{\frac{3}{2}}}{2(2\pi)^2}\frac{\pi}{4}\frac{|\omega_n|}{v_F k}\right\}|M(\mathbf{k},\omega$$

Or it can be written in the compact form

$$\mathcal{H}^{(2)}[M] \approx \int \frac{d^3k}{(2\pi)^3\beta}\sum_{n=-\infty}^{\infty}\frac{1}{2}\left(r_0+c_1k^2+c_2\frac{|\omega_n|}{k}\right)|M(\mathbf{k},\omega_n)|^2 \tag{D.29}$$

where r_0 is a parameter which can be controlled (by U) so that it can be positive or negative, thus it is a control parameter around the criticality. At criticality, $r_0 = 0$.

D.3 The ϕ^4 Term

Using the identity [123]

$$Tr(\sigma^a\sigma^b\sigma^c\sigma^d) = 2(\delta^{ab}\delta^{cd}-\delta^{ac}\delta^{bd}+\delta^{ad}\delta^{bc}) \tag{D.30}$$

the fourth order term of the expansion (D.11) is given by

$$\begin{aligned}
-\frac{1}{4}Tr\left(\mathcal{G}^0\frac{\sqrt{U}}{2}M^i\sigma^i\right)^4 &= -\frac{3U^2}{2^5}Tr(\mathcal{G}^0M^i\mathcal{G}^0M^i\mathcal{G}^0M^j\mathcal{G}^0M^j) \\
&= -\frac{3U^2}{2^5}\int d^3x_1\int_0^\beta d\tau_1\int d^3x_2\int_0^\beta d\tau_2\int d^3x_3\int_0^\beta d\tau_3\int d^3x_4\int_0^\beta d\tau_4 \\
&\quad \cdot\mathcal{G}^0(\mathbf{x}_1-\mathbf{x}_2,\tau_1-\tau_2)M^i(\mathbf{x}_2,\tau_2)\mathcal{G}^0(\mathbf{x}_2-\mathbf{x}_3,\tau_2-\tau_3)M^i(\mathbf{x}_3,\tau_3) \\
&\quad \cdot\mathcal{G}^0(\mathbf{x}_3-\mathbf{x}_4,\tau_3-\tau_4)M^i(\mathbf{x}_4,\tau_4)\mathcal{G}^0(\mathbf{x}_4-\mathbf{x}_1,\tau_4-\tau_1)M^i(\mathbf{x}_1,\tau_1) \\
&= -\frac{3U^2}{2^5}\int d^3k_1\sum_{n_1=-\infty}^{\infty}\int d^3k_2\sum_{n_2=-\infty}^{\infty}\int d^3k_3\sum_{n_3=-\infty}^{\infty} \\
&\quad \cdot\Gamma(\mathbf{k}_1,\omega_{n_1};\mathbf{k}_2,\omega_{n_2};\mathbf{k}_3,\omega_{n_3})M^i(\mathbf{k}_1,\omega_{n_1})M^i(\mathbf{k}_2,\omega_{n_2}) \\
&\quad \cdot M^j(\mathbf{k}_3,\omega_{n_3})M^j(-\mathbf{k}_1-\mathbf{k}_2-\mathbf{k}_3,-\omega_{n_1}-\omega_{n_2}-\omega_{n_3})
\end{aligned}$$

where the function $\Gamma(\mathbf{k}_1,\omega_{n_1};\mathbf{k}_2,\omega_{n_2};\mathbf{k}_3,\omega_{n_3})$ is given by

$$\begin{aligned}
\Gamma(\mathbf{k}_1,\omega_{n_1};\mathbf{k}_2,\omega_{n_2};\mathbf{k}_3,\omega_{n_3}) &= \frac{1}{\beta}\sum_{n=-\infty}^{\infty}\int\frac{d^3k}{(2\pi)^3} \\
&\quad \cdot\mathcal{G}^0(\mathbf{k},\omega_n)\mathcal{G}^0(\mathbf{k}+\mathbf{k}_1,\omega_n+\omega_{n_1})\mathcal{G}^0(\mathbf{k}-\mathbf{k}_2,\omega_n-\omega_{n_2}) \\
&\quad \cdot\mathcal{G}^0(\mathbf{k}-\mathbf{k}_1-\mathbf{k}_2,\omega_n-\omega_{n_1}-\omega_{n_2}) \qquad \text{(D.31)}
\end{aligned}$$

For long-wavelength approximation, take $k_i \approx 0$ and $\omega_{n_i} \approx 0$ for $i = 1, 2, 3$, then

$$\Gamma(\mathbf{k}_1,\omega_{n_1};\mathbf{k}_2,\omega_{n_2};\mathbf{k}_3,\omega_{n_3}) \approx \Gamma(\mathbf{0},0;\mathbf{0},0;\mathbf{0},0) = \frac{1}{\beta}\sum_{n=-\infty}^{\infty}\int\frac{d^3k}{(2\pi)^3}[\mathcal{G}^0(\mathbf{k},\omega_n)]^4 \qquad \text{(D.32)}$$

which is a positive constant and we denote it as u. Then, up to a constant factor,

the fourth-order term of the functional is given by

$$\begin{aligned}\mathcal{H}^{(4)}[M] \approx & \frac{u}{4}\int\frac{d^3k_1}{(2\pi)^3\beta}\sum_{n_1=-\infty}^{\infty}\int\frac{d^3k_2}{(2\pi)^3\beta}\sum_{n_2=-\infty}^{\infty}\int\frac{d^3k_3}{(2\pi)^3\beta}\sum_{n_3=-\infty}^{\infty} \\ & \cdot M^i(\mathbf{k}_1,\omega_{n_1})M^i(\mathbf{k}_2,\omega_{n_2})M^j(\mathbf{k}_3,\omega_{n_3}) \\ & \cdot M^j(-\mathbf{k}_1-\mathbf{k}_2-\mathbf{k}_3,-\omega_{n_1}-\omega_{n_2}-\omega_{n_3}) \end{aligned} \tag{D.33}$$

D.4 LGW Functional

From the Hubbard model, the Landau-Ginzburg form of the Hamiltonian can be derived. The result can be generalized to other dimensions and written as

$$\begin{aligned}\mathcal{H}[M] \approx & \int\frac{d^dk}{(2\pi)^d\beta}\sum_{n=-\infty}^{\infty}\frac{1}{2}\left(r_0+c_1k^2+c_2\frac{|\omega_n|}{k}\right)|M(\mathbf{k},\omega_n)|^2 \\ & +\frac{u}{4}\int\frac{d^dk_1}{(2\pi)^d\beta}\sum_{n_1=-\infty}^{\infty}\int\frac{d^dk_2}{(2\pi)^d\beta}\sum_{n_2=-\infty}^{\infty}\int\frac{d^dk_3}{(2\pi)^d\beta}\sum_{n_3=-\infty}^{\infty} \\ & \cdot M^i(\mathbf{k}_1,\omega_{n_1})M^i(\mathbf{k}_2,\omega_{n_2})M^j(\mathbf{k}_3,\omega_{n_3}) \\ & \cdot M^j(-\mathbf{k}_1-\mathbf{k}_2-\mathbf{k}_3,-\omega_{n_1}-\omega_{n_2}-\omega_{n_3}) \end{aligned} \tag{D.34}$$

And this Hamiltonian is the starting point of studying quantum critical phenomena.

This Hamiltonian can be expressed in real space. The real space representation of terms with r, c_1 and u can be found easily by Fourier transform, but the term involving c_2 is more complicated and is shown below. The Fourier transform of the order parameter is given by

$$\mathbf{M}(\mathbf{k},\omega_n)=\int d^dx\int_0^\beta d\tau\mathbf{M}(\mathbf{x},\tau)e^{-i(\mathbf{k}\cdot\mathbf{x}-\omega_n\tau)} \tag{D.35}$$

Then the term involving c_2 is

$$\begin{aligned}
& \int \frac{d^d k}{(2\pi)^d \beta} \sum_{n=-\infty}^{\infty} \frac{\omega_n}{k} |\mathbf{M}(\mathbf{k}, \omega_n)|^2 \\
= & \int \frac{d^d k}{(2\pi)^d \beta} \sum_{n=-\infty}^{\infty} \frac{\omega_n}{k} \int d^d x_1 \int_0^\beta d\tau_1 M^i(\mathbf{x}_1, \tau_1) e^{-i(\mathbf{k}\cdot\mathbf{x}_1 - \omega_n \tau_1)} \\
& \cdot \int d^d x_2 \int_0^\beta d\tau_2 M^i \mathbf{x}_2, \tau_2) e^{-i(\mathbf{k}\cdot\mathbf{x}_2 - \omega_n \tau_2)} \\
= & \int d^d x_1 \int_0^\beta d\tau_1 \int d^d x_2 \int_0^\beta d\tau_2 M^i(\mathbf{x}_1, \tau_1) M^i(\mathbf{x}_2, \tau_2) \\
& \cdot \int \frac{d^d k}{(2\pi)^d \beta} \sum_{n=-\infty}^{\infty} \frac{e^{-i\mathbf{k}\cdot(\mathbf{x}_1 - \mathbf{x}_2)}}{ik} \left[\frac{\partial}{\partial \tau_1} e^{i\omega_n(\tau_1 - \tau_2)} \right] \\
= & i \int_0^\beta d\tau \int d^d x_1 \int d^d x_2 \left(\frac{\partial}{\partial \tau} M^i(\mathbf{x}_1, \tau_1) \right) M^i(\mathbf{x}_2, \tau_2) \int \frac{d^d k}{(2\pi)^d} \frac{e^{-i\mathbf{k}\cdot(\mathbf{x}_1 - \mathbf{x}_2)}}{k}
\end{aligned}$$

The integral in the momentum space can be evaluated using the technique in Appendix E with the use of (E.3):

$$\begin{aligned}
\int \frac{d^d k}{(2\pi)^d} \frac{e^{-i\mathbf{k}\cdot(\mathbf{x}_1 - \mathbf{x}_2)}}{k} &= \frac{K_{d-1}}{2\pi} \int_0^\Lambda dk \int_0^\pi d\theta k^{d-1} \sin^{d-2}\theta \frac{e^{-ik|\mathbf{x}_1 - \mathbf{x}_2|\cos\theta}}{k} \\
&= \frac{K_{d-1}}{2\pi} \int_0^\Lambda dk \cdot k^{d-2} \int_0^\pi d\theta \sin^{d-2}\theta \cdot e^{-ik|\mathbf{x}_1 - \mathbf{x}_2|\cos\theta} \\
&= \frac{K_{d-1}(d-2)!}{2\pi(i|\mathbf{x}_1 - \mathbf{x}_2|)^{d-1}} \left[1 - e^{-i\Lambda|\mathbf{x}_1 - \mathbf{x}_2|} e_{d-2}(i\Lambda|\mathbf{x}_1 - \mathbf{x}_2|) \right] \int_0^\pi d\theta \sin^{d-2}\theta
\end{aligned}$$

where K_d is given in (E.4) and $e_n(x)$ is the exponential sum function as

$$e_n(x) = \sum_{j=0}^{n} \frac{x^j}{j!} \tag{D.36}$$

The integral involving the powers of sine and angle is given as

$$\frac{1}{2} \int_0^\pi d\theta \cdot \sin^{d-2}\theta = \frac{(d-3)!!}{(d-2)!!} \begin{cases} \frac{\pi}{2} & \text{for even } d \\ 1 & \text{for odd } d \end{cases} \tag{D.37}$$

As a result, this term becomes

$$-\int_0^\beta d\tau \int d^d x_1 \int d^d x_2 \frac{E_d[1 - e^{-i\Lambda|\mathbf{x}_1 - \mathbf{x}_2|} e_{d-2}(i\Lambda|\mathbf{x}_1 - \mathbf{x}_2|)]}{|\mathbf{x}_1 - \mathbf{x}_2|^{d-1}} \left[\frac{\partial \mathbf{M}(\mathbf{x}_1, \tau_1)}{\partial \tau} \right] \cdot \mathbf{M}(\mathbf{x}_2, \tau_2) \tag{D.38}$$

where E_d is given by

$$E_d = \frac{K_{d-1}(d-2)!}{i^d \pi} \frac{(d-3)!!}{(d-2)!!} \begin{cases} \frac{\pi}{2} & \text{for even } d \\ 1 & \text{for odd } d \end{cases} \tag{D.39}$$

Appendix E

Multiple Integrals Involving Angles

In the study of field theory in condensed matter, integrals of the following form are always encountered:

$$I_m(\mathbf{k}_1, \mathbf{k}_2, \ldots, \mathbf{k}_m) = \int \frac{d^d k}{(2\pi)^d} f(k^2; \mathbf{k}\cdot\mathbf{k}_1, \mathbf{k}\cdot\mathbf{k}_2, \ldots, \mathbf{k}\cdot\mathbf{k}_m) \tag{E.1}$$

Usually, the situations are either $m = 0$ or $m = 1$. It has been listed in Ref. [128] that

$$I_0 = \int \frac{d^d k}{(2\pi)^d} f(k^2) = K_d \int dk \cdot k^{d-1} f(k^2) \tag{E.2}$$

and

$$I_1(\mathbf{k}_1) = \int \frac{d^d k}{(2\pi)^d} f(k^2, \mathbf{k}\cdot\mathbf{k}_1) = \frac{K_{d-1}}{2\pi} \int dk \int_0^\pi d\theta k^{d-1} \sin^{d-2}\theta f(k^2; k_1 k\cos\theta) \tag{E.3}$$

where K_d is defined by

$$K_d = \frac{2^{-(d-1)}\pi^{-\frac{d}{2}}}{\Gamma\left(\frac{d}{2}\right)} \tag{E.4}$$

Appendix F

Power counting in calculating diagrams for conductivity

In this appendix, we discuss the power counting for diagrams in Fig. 5.6.

F.1 Power counting for diagrams (i) and (ii)

Here we provide the arguments that lead to Eq. (5.68). We first do a power-counting analysis of Eqs. (5.66). We first discuss the result of helimagnons, and for columnar phase, there is one more order of T. From Eqs. (4.22), (5.7) and (5.66) we see that the soft helimagnon wave number k scales with temperature as $k_z \sim k_\perp^2 \sim T$. The frequencies scale as $u \sim \epsilon \sim T$, and $\chi''(\mathbf{k}, u) \sim 1/T^2$. Consequently, the conductivity corrections $\delta\sigma^{(i,ii)}$ scale as $\delta\sigma \sim TJ$ for a given integrand $J(k)$ (or $I(k)$).

First consider the integral $J_{ij}^{++-,+}(k)$, Eqs. (5.67). For power-counting purposes, the integration variable $\mathbf{p}$ scales as T^0, and the leading term in the vertex γ scales as $\gamma(\mathbf{k}, \mathbf{p}) \sim k_\perp \sim T^{1/2}$. [1] A representation that suffices for power counting is thus

$$J_{ij}^{++-,+}(k) \propto k_\perp^2 \int_{-\infty}^{\infty} d\xi \int_{-1}^{1} d\eta \frac{1}{(\xi - i/2\tau)^2} \frac{1}{\xi + i/2\tau} \frac{1}{\xi - i/2\tau - v_{\mathrm{F}} k\eta} \propto \frac{\tau^2 k_\perp^2}{k} \int_0^{v_{\mathrm{F}} k\tau} \frac{dx}{1+x^2} \tag{F.1a}$$

in the AGD approximation. [53] For $v_{\mathrm{F}} k \gg 1/\tau$ we thus have $J_{ij}^{++-,+}(k) \propto \tau^2 k_\perp^2 / k$,

[1] For columnar phase, $\gamma(\mathbf{k}, \mathbf{p}) \sim k_z \sim T^{1/2}$.

with corrections carrying an extra factor of $1/v_{\rm F}k\tau \sim 1/\tau T^{1/2}$, or

$$J_{ij}^{++-,+}(k) \sim \tau^2 T^{1/2} + \tau, \tag{F.1b}$$

which leads to $\delta\sigma \propto \tau^2 T^{3/2} + \tau T$. Analogous arguments yield

$$J_{ij}^{++-,-}(k) \sim \tau^2 T^{1/2} + \tau, \tag{F.2}$$

$$J_{ij}^{+-,+-}(k) \sim \tau^2 T^{1/2} + \tau, \tag{F.3}$$

$$J_{ij}^{+-,++}(k) \sim \tau. \tag{F.4}$$

The convolutions I, compared to the corresponding J, carry an additional factor of $k_\perp \sim T^{1/2}$. In addition, the resulting vector nature of the integrand leads to an another factor of either $k_\perp \sim T^{1/2}$, or $k_z \sim T$. Therefore, the I carry an additional factor of T compared to the corresponding J. Terms that were dropped in writing Eqs. (5.66) involved $J^{+++,+}$, $J^{+++,-}$, $J^{++,++}$, and $J^{++,--}$, which are of higher order in the disorder by at least three powers of $1/\tau$. Including terms of $O(\tau T)$, we thus can write the conductivity correction, Eqs. (5.66),

$$\begin{aligned}
&\delta\sigma_{ij}^{(i)} + \delta\sigma_{ij}^{(ii)} \\
= \; & -\frac{V_0}{4\pi}\frac{1}{T}\int_{-\infty}^{\infty}\frac{d\epsilon}{\cosh^2(\epsilon/T)}\frac{1}{V}\sum_{\mathbf{k}}\int_{-\infty}^{\infty}\frac{du}{\pi}\chi''(\mathbf{k},u)\Bigg[n_{\rm B}\left(\frac{u}{T}\right)\,{\rm Re}\,\left[J_{ij}^{++-,+}(k)+\frac{1}{2},J_{ij}^{+-,+-}(k)\right] \\
& +\frac{1}{2}\,n_{\rm F}\left(\frac{u-\epsilon}{T}\right)\,{\rm Re}\,\left[J_{ij}^{++-,+}(k)+J_{ij}^{+-,+-}(k)-J_{ij}^{++-,-}(k)-J_{ij}^{+-,++}(k)\right]\Bigg].
\end{aligned} \tag{F.5}$$

The J can be simplified by means of partial fraction decompositions. For the relevant combinations one finds for helimagnons

$${\rm Re}\,\left[J_{ij}^{++-,+}(k)+\frac{1}{2},J_{ij}^{+-,+-}(k)\right] \propto \tau^2 k_\perp^3 \sim \tau^2 T^{3/2}, \tag{F.6a}$$

$${\rm Re}\,\left[J_{ij}^{++-,+}(k)+J_{ij}^{+-,+-}(k)-J_{ij}^{++-,-}(k)-J_{ij}^{+-,++}(k)\right] = o(\tau T^0). \tag{F.6b}$$

This leads to Eq. (5.68a) for helimagnons.

For the columnar phase, there is an extra power of T in Eqs. (F.6).

F.2 Diagram (vii)

Here we consider diagram (vii) in Fig. 5.6(c) as a prototype of a class of diagrams that do not contribute to the leading behavior of the conductivity if evaluated to lowest order in $q/k_{\rm F}$. We first perform the calculation for helimagnons. The leading contribution to the conductivity correction from this diagram can be written

$$\begin{aligned}\delta\sigma_{ij}^{(vii)} &= -\frac{u_0 V_0}{8\pi m_{\rm e}^2}\frac{1}{T}\int_{-\infty}^{\infty}\frac{d\epsilon}{\cosh^2(\epsilon/2T)} \\ &\quad \int_{-\infty}^{\infty}\frac{du}{\pi}n_{\rm F}\left(\frac{u-\epsilon}{T}\right)\mathrm{Im}\,\frac{1}{V}\sum_{\mathbf{k}}\chi_R(\mathbf{k},u)\frac{1}{V}\sum_{\mathbf{p}}\gamma(\mathbf{k},\mathbf{p})G_R(\mathbf{p})G_A(\mathbf{p}-\mathbf{k}) \\ &\quad \times\frac{1}{V}\sum_{\mathbf{p}'}p_i' p_j'\gamma(\mathbf{k},\mathbf{p}')G_R(\mathbf{p}')G_R(\mathbf{p}')G_A(\mathbf{p}')G_A(\mathbf{p}'-\mathbf{k}), \qquad \text{(F.7)}\end{aligned}$$

which shows the (2,4) structure mentioned in Section 5.4.3.2. The bosonic distribution function does not contribute to this diagram, so it can be at most of $O(\tau T)$. With the convolutions evaluated for $q = 0$, power counting shows that it is of $O(\tau T^2)$, and an explicit calculation confirms this. Now we expand the resonance frequency $\omega_1(\mathbf{p})$, Eq. (5.15b), to first order in q: $\omega_1(\mathbf{p}) = \xi_{\mathbf{p}} + \mathbf{p}\cdot\mathbf{q}/2m_{\rm e} + O(q^2)$. For the leading contribution to the first convolution in Eq. (F.7) we then find

$$\begin{aligned}N^{+,-}(\mathbf{k}) &\equiv \frac{1}{V}\sum_{\mathbf{p}}\gamma(\mathbf{k},\mathbf{p})G_R(\mathbf{p})G_A(\mathbf{p}-\mathbf{k}) \\ &\propto \frac{\nu}{\lambda k_{\rm F}^2}\left[\frac{k_\perp^2 k_z}{k^3}+\frac{k_\perp^2 q}{k^2 k_{\rm F}}+O(q^2)\right]. \qquad \text{(F.8)}\end{aligned}$$

We see that, at linear order in q, a factor that used to be $k_z/k \sim k_z/k_\perp \sim T^{1/2}$ gets replaced by $q/k_\mathrm{F} \sim T^0$. The same holds for the other convolution. As a result, the diagram is of $O(\tau T)$, and an explicit calculation shows that the dependence of the prefactor on $\epsilon_\mathrm{F}/\lambda$ and q/k_F are the same as for diagram (iii), with the exception of the additional factor of $(q/k_\mathrm{F})^2$. We thus have

$$\delta\sigma_{ij}^{(vii)} \propto T. \tag{F.9}$$

For the columnar phase, both terms in Eq. (F.8) have dependence $\sim T$, which leads to

$$\delta\sigma_{ij}^{(vii)} \propto T^{7/2}, \tag{F.10}$$

which is not the leading term.

Bibliography

[1] John David Jackson. *Classical Electrodynamics*. Wiley, third edition, 1998.

[2] Charles Kittel. *Introduction to Solid State Physics*. Wiley, Hoboken, NJ, 1996.

[3] H. J. Williams, J. H. Wernick, R. C. Sherwood, and G. K. Wertheim. Magnetic properties of the monosilicides of some 3*d* transition elements. *J. Appl. Phys.*, 37:1256, 1966.

[4] P. J. Brown, J. B. Forsyth, and G. H. Lander. Spatial distribution of the magnetic moment in MnSi. *J. Appl. Phys.*, 39:1331, 1968.

[5] Y. Ishikawa, K. Tajima, D. Bloch, and M. Roth. Helical spin structure in manganese silicide MnSi. *Solid State Commun.*, 19:525, 1976.

[6] T. Moriya. Theory of helical spin structure in itinerant electron systems. *Solid State Commun.*, 20:291, 1976.

[7] Masaya Uchida, Yoshinori Onose, Yoshio Matsui, and Yoshinori Tokura. Real-space observation of helical spin order. *Science*, 311:359, 2006.

[8] X. Z. Yu, Y. Onose, N. Kanazawa, J. H. Park, J. H. Han, Y. Matsui, N. Nagaosa, and Y. Tokura. Real-space observation of a two-dimensional skyrmion crystal. *Nature*, 465:901, 2010.

[9] I. E. Dzyaloshinski. A thermodynamics theory of "weak" ferromagnetism of antiferromagnetics. *J. Phys. Chem. Solids*, 4:241, 1958.

[10] Tôru Moriya. Anisotropic superexchange interaction and weak ferromagnetism. *Phys. Rev.*, 120:91, 1960.

[11] D. Belitz and T. R. Kirkpatrick. Quantum electrodynamics and the origins of the exchange, dipole-dipole, and Dzyaloshinsky-Moriya interactions in itinerant Fermion systems. *Phys. Rev. B*, 81:184419, 2010.

[12] O. Nakanishi, A. Yanase, A. Hasegawa, and M. Kataoka. The origin of the helical spin density wave in MnSi. *Solid State Commun.*, 35:995, 1980.

[13] A. Bauer, A. Neubauer, C. Franz, W. Münzer, M. Garst, and C. Pfleiderer. Quantum phase transitions in single-crystal $Mn_{1-x}Fe_xSi$ and $Mn_{1-x}Co_xSi$: Crystal growth, magnetization, ac susceptibility, and specific heat. *Phys. Rev. B*, 82:064404, 2010.

[14] M. Uchida, N. Nagaosa, J. P. He, Y. Kaneko, S. Iguchi, Y. Matsui, and Y. Tokura. Topological spin textures in the helimagnet FeGe. *Phys. Rev. B*, 77:184402, 2008.

[15] J. Beille, J. Voiron, F. Towfiq, M. Roth, and Z. Y. Zhang. Helimagnetic structure of the $Fe_xCo_{1-x}Si$ alloys. *J. Phys. F: Metal Phys.,*, 11:2153, 1981.

[16] K. Ishimoto, Y. Yamaguchi, J. Suzuki, M. Arai, M. Furusaka, and Y. Endoh. Small-angle neutron diffraction from the helical magnet $Fe_{0.8}Co_{0.2}Si$. *Physica B*, 213 & 214:381, 1995.

[17] J. W. Cable, M. K. Wilkinson, E. O. Wollan, and W. C. Koehler. Neutron-diffraction study of antiferromagnetic $FeCl_3$. *Phys. Rev.*, 127:714, 1962.

[18] A. Yoshimori. A new type of antiferromagnetic structure in the rutile type crystal. *J. Phys. Soc. Jpn.*, 14:807, 1959.

[19] T. A. Kaplan. Classical spin-configuration stability in the presence of competing exchange forces. *Phys. Rev.*, 116:888, 1959.

[20] Norberto Majlis. *The Quantum Theory of Magnetism*. World Scientific, 2000.

[21] R. M. White. *Quantum Theory of Magnetism: Magnetic Properties of Materials*. Springer-Verlag, New York, NY, 2007.

[22] Y. Tokunaga, Y. Kaneko, D. Okuyama, S. Ishiwata, T. Arima, S. Wakimoto, K. Kakurai, Y. Taguchi, and Y. Tokura. Multiferroic m-type hexaferrites with a room-temperature conical state and magnetically controllable spin helicity. *Phys. Rev. Lett.*, 105:257201, 2010.

[23] C. Pfleiderer, S. R. Julian, and G. G. Lonzarich. Non-Fermi-liquid nature of the normal state of iteinerant-electron ferromagnets. *Nature*, 414:427, 2001.

[24] Pierre Gilles de Gennes and Jacques Prost. *The Physics of Liquid Crystals*. Oxford University Press, New York, NY, 1993.

[25] S. M. Stishov and A. E. Petrova. Itinerant helimagnet MnSi. *Physics - Uspekhi*, 54:1117, 2011.

[26] C. Thessieu, C. Pfleiderer, A. N. Stepanov, and J. Flouquet. Field dependence of the magnetic quantum phase transition in MnSi. *J. Phys.: Condens. Matter*, 9:6677, 1997.

[27] H. Wilhelm, M. Barnitz, M. Schmidt, U. K. Röβler, A. A. Leonov, and A. N. Bogdanov. Precursor phenomena at the magnetic ordering of the cubic helimagnet FeGe. *Phys. Rev. Lett.*, 107:127203, 2011.

[28] C. Pfleiderer, G. J. McMullan, S. R. Julian, and G. G. Lonzarich. Magnetic quantum phase transition in MnSi under hydrostatic pressure. *Phys. Rev. B*, 55:8330, 1997.

[29] D. Belitz, T. R. Kirkpatrick, and Thomas Vojta. First order transitions and multicritical points in weak itinerant ferromagnets. *Phys. Rev. Lett.*, 82:4707, 1999.

[30] D. Belitz, T. R. Kirkpatrick, and Jörg Rollbühler. Tricritical behavior in itinerant quantum ferromagnets. *Phys. Rev. Lett.*, 94:247205, 2005.

[31] C. Pappas, E. Leliévre-Berna, P. Falus, P. M. Bentley, E. Moskvin, S. Grigoriev, P. Fouquet, and B. Farago. Chiral paramagnetic skyrmion-like phase in mnsi. *Phys. Rev. Lett.*, 102:197202, 2009.

[32] C. Pappas, E. Leliévre-Berna, P. Bentley, P. Falus, P. Fouquet, and B. Farago. Magnetic fluctuations and correlations in MnSi: Evidence or a chiral skyrmion spin liquid phase. *Phys. Rev. B*, 83:224405, 2011.

[33] A. Mühlbauer, B. Binz, F. Jonietz, C. Pfleiderer, A. Rosch, A. Neubauer, R. Georgii, and P. Böni. Skyrmion lattice in a chiral manget. *Science*, 323:915, 2009.

[34] T. Adams, S. Mühlbauer, A. Neubauer, W. Münzer, F. Jonietz, R. Georgii, B. Pedersen, P. Böni, A. Rosch, and C. Pfleiderer. Skyrmion lattice domains in $Fe_xCo_{1-x}Si$. *J. Phys.: Conf. Ser.*, 200:032001, 2010.

[35] A. A. Abrikosov. On the magnetic properties of superconductors of the second group. *Sov. Phys. JETP*, 5(6):1174, 1957.

[36] Alexander L. Fetter. Rotating trapped Bose-Einstein condensates. *Rev. Mod. Phys.*, 81:647, 2009.

[37] Elisabetta A. Matsumoto, Gareth P. Alexander, and Randall D. Kamien. Helical nanofilaments and the high chirality limit of smectics *a*. *Phys. Rev. Lett.*, 103:257804, 2009.

[38] Elisabetta A. Matsumoto. The taming of the screw: or how i learned to stop worrying and love elliptic functions. PhD Thesis, University of Pennsylvannia, 2011.

[39] O. Henrich, D. Marenduzzo, K. Stratford, and M. E. Cates. Thermodynamics of blue phases in electric fields. *Phys. Rev. E*, 81:031706, 2010.

[40] X. Z. Yu, N. Kanazawa, Y. Onose, W. Z. Zhang, S. Ishiwata, Y. Matsui, and Y. Tokura. Near room-temperature formation of skyrmion crystal in thin-films of the helimagnet FeGe. *Nat. Mat.*, 10:106, 2010.

[41] B. Roessli, P. Böni, W. E. Fischer, and Y. Endoh. Chiral fluctuations in MnSi above the Curie temperature. *Phys. Rev. Lett.*, 88:237204, 2002.

[42] J. Goldstone. Field theories with superconductor solutions. *Nuovo Cimento*, 19(1):154, 1961.

[43] Tom C. Lubensky. Hydrodynamics of cholesteric liquid crystals. *Phys. Rev. A*, 6:452, 1972.

[44] D. Belitz, T. R. Kirkpatrick, and A. Rosch. Theory of helimagnons in itinerant quantum systems. *Phys. Rev. B*, 73:054431, 2006.

[45] N. D. Mermin and H. Wagner. Absence of ferromagnetism or antiferromagnetism in one- or two-dimensional isotropic Heisenberg models. *Phys. Rev. Lett.*, 17:1133, 1966.

[46] P. C. Hohenberg. Existence of long-range order in one and two dimensions. *Phys. Rev.*, 158:383, 1967.

[47] S. Coleman. There are no Goldstone bosons in two dimensions. *Comm. Math. Phys.*, 31:259, 1973.

[48] Kwan-Yuet Ho, T. R. Kirkpatrick, Yan Sang, and D. Belitz. Ordered phases of itinerant Dzyaloshinsky-Moriya magnets and their electronic properties. *Phys. Rev. B*, 82:134427, 2010.

[49] P. G. de Gennes. An analogy between superconductors and smectics A. *Solid State Commun.*, 10:753, 1972.

[50] T. R. Kirkpatrick and D. Belitz. Columnar fluctuations as a source of non-Fermi-liquid behavior in weak metallic magnets. *Phys. Rev. Lett.*, 104:256404, 2010.

[51] T. R. Kirkpatrick and D. Belitz. Nonanalytic corrections to Fermi-liquid behavior in helimagnets. *Phys. Rev. B*, 72:180402, 2005.

[52] C. Pfleiderer. Experimental studies of weakly magnetic transition metal compounds. *J. Mag. Mag. Mater.*, 226-230:23, 2001.

[53] A. A. Abrikosov, L. P. Gorkov, and I. E. Dzyaloshinski. *Methods of Quantum Field Theory in Statistical Physics*. Dover, New York, NY, 1975.

[54] Tony Hilton Royle Skyrme. A nonlinear field theory. *Proc. Roy. Soc. London A*, 260:127, 1961.

[55] H. A. Fertig, Luis Brey, R. Côté, A. H. MacDonald, A. Karlhede, and S. L. Sondhi. Hartree-Fock theory of Skyrmions in quantum Hall ferromagnets. *Phys. Rev. B*, 55:10671, 1997.

[56] Carsten Timm, S. M. Girvin, and H. A. Fertig. Skyrmion lattice melting in the quantum Hall system. *Phys. Rev. B*, 58:10634, 1998.

[57] A. N. Bogdanov, U. K. Röβler, and A. A. Shestakov. Skyrmions in nematic liquid crystals. *Phys. Rev. E*, 67:016602, 2003.

[58] Qi Li, John Toner, and D. Belitz. Skyrmion versus vortex flux lattices in p-wave superconductors. *Phys. Rev. B*, 79:014517, 2009.

[59] Qi Li. Short-range interacting skyrmion charges in the long-range interacting skyrmion lattice. *Phys. Lett. A*, 374:3987, 2010.

[60] Tin-Lun Ho. Spinor Bose condensates in optical traps. *Phys. Rev. Lett.*, 81:742, 1998.

[61] L. S. Leslie, A. Hansen, K. C. Wright, B. M. Deutsch, and N. P. Bigelow. Creation and detection of skyrmions in a bose-einstein condensate. *Phys. Rev. Lett.*, 103:250401, 2009.

[62] Tarun Grover and T. Senthil. Topological spin Hall states, charged Skyrmions, and superconductivity in two dimensions. *Phys. Rev. Lett.*, 100:156804, 2008.

[63] A. Bogdanov. New localized solutions of the nonlinear field equations. *JETP Letters*, 62:231, 1995.

[64] A. Bogdanov and A. Hubert. Thermodynamically stable magnetic vortex states in magnetic crystals. *J. Mag. Mag. Mater.*, 138:255, 1994.

[65] A. N. Bogdanov and D. A. Yablonskiĭ. Thermodynamically stable "vortices" in magnetically ordered crystals. the mixed state of magnets. *Sov. Phys. JETP*, 68:101, 1989.

[66] Christian Pfleiderer and Achim Rosch. Condensed-matter physics: Single skyrmions spotted. *Nature*, 465:880, 2010.

[67] R. Rajaraman. *Solitons and Instantons*. Elsevier, New York, NY, 1987.

[68] Jung Hoon Han, Jiadong Zang, Zhihua Yang, Jin-Hong Park, and Naoto Nagaosa. Skyrmion lattice in two-dimensional chiral magnet. *Phys. Rev. B*, 82:094429, 2010.

[69] Ulrich K. Röβler, Andrei A. Leonov, and Alexei N. Bogdanov. Chiral Skyrmionic matter in non-centrosymmetrtic magnets. *J. Phys.: Conf. Ser.*, 303:012105, 2011.

[70] I. S. Gradshteyn and I. M. Ryzhik. *Table of Integrals, Series and Products*. Elsevier, Oxford, Great Britain, 2007.

[71] S. K. Ma. *Modern Theory of Critical Phenomena*. Benjamin/Cummings, Reading, MA, 1976.

[72] Space group 198. *International Tables for Crystallography*, A:610, 2006.

[73] Per Bak and M Høgh Jensen. Theory of helical magnetic structures and phase transitions in MnSi and FeGe. *J. Phys. C: Solid State Phys.*, 13:L881, 1980.

[74] Kwan-Yuet Ho, T. R. Kirkpatrick, and D. Belitz. Skyrmions and their sizes in helimagnets. 2011.

[75] D. Belitz, T. R. Kirkpatrick, and Thomas Vojta. How generic scale invariance influences quantum and classical phase transitions. *Rev. Mod. Phys.*, 77:579, 2005.

[76] S. V. Grigoriev, S. V. Maleyev, A. I. Okorokov, Yu. O. Chetverikov, and H. Eckerlebe. Field-induced reorientation of the spin helix in MnSi near t_c. *Phys. Rev. B*, 73:224440, 2006.

[77] U. K. Röβler, A. N. Bogdanov, and C. Pfleiderer. Spontaneous skyrmion ground states in magnetic metals. *Nature*, 442:797, 2006.

[78] P. G. de Gennes. Calcul de la distorsion d'une structure cholesterique par un champ magnetique. *Solid State Commun.*, 6:163, 1968.

[79] W. H. Kleiner, L. M. Roth, and S. H. Autler. Bulk solution of ginzburg-landau equations for type ii superconductors: Upper critical field region. *Phys. Rev.*, 133:A1226, 1964.

[80] James F. Annett. *Superconductivity, Superfluids, and Condensates*. Oxford Master Series in Condensed Matter Physics. Oxford University Press, 2004.

[81] M. L. Plumer and M. B. Walker. Wavevector and spin reorientation in MnSi. *J. Phys. C: Solid State Phys.*, 14:4689, 1981.

[82] M. B. Walker. Phason instabilities and successive wave-vector reorientation phase transitions in MnSi. *Phys. Rev. B*, 40:9315, 1989.

[83] J. A. Hertz. Quantum critical phenomena. *Phys. Rev. B*, 14:1165, 1975.

[84] A. J. Millis. Effect of a nonzero temperature on quantum critical points in itinerant fermion systems. *Phys. Rev. B*, 48:7183, 1993.

[85] Subir Sachdev. *Quantum Phase Transitions*. Cambridge University Press, 2001.

[86] Thomas Vojta and Rastko Sknepnek. The quantum phase transition of itinerant helimagnets. *Phys. Rev. B*, 64:052404, 2001.

[87] Jörg Schmalian and Misha Turlakov. Quantum phase transitions of magnetic rotons. *Phys. Rev. Lett.*, 93:036406, 2004.

[88] Sumanta Tewari, D. Belitz, and T. R. Kirkpatrick. Blue quantum flog: Chiral condensation in quantum helimagnets. *Phys. Rev. Lett.*, 96:047207, 2006.

[89] N. D. Mermin. The topological theory of defects in ordered media. *Rev. Mod. Phys.*, 51:591, 1979.

[90] Jean Zinn-Justin. *Quantum Field Theory and Critical Phenomena*. Oxford University Press, Oxford, 1996.

[91] T. R. Kirkpatrick and D. Belitz. Soft modes in electronic stripe phases and their consequences for thermodynamics and transport. *Phys. Rev. B*, 80:075121, 2009.

[92] Olga Petrova and Oleg Tchernyshyov. Spin waves in a skyrmion crystal. *Phys. Rev. B*, 84:214433, 2011.

[93] D. Belitz, T. R. Kirkpatrick, and A. Rosch. Theory of helimagnons in itinerant quantum systems II: Nonanalytic corrections to Fermi-liquid behavior. *Phys. Rev. B*, 74:024409, 2006.

[94] Alexander L. Fetter and John Dirk Walecka. *Quantum Theory of Many-Particle Systems*. Dover, New York, NY, 2003.

[95] T. R. Kirkpatrick, D. Belitz, and Ronojoy Saha. Theory of helimagnons in itinerant quantum systems III: quasiparticle description. *Phys. Rev. B*, 78:094407, 2008.

[96] Bogdan Mihaila. Lindhard function of a d-dimensional Fermi gas. 2011.

[97] Dieter Forster. *Hydrodynamic Fluctuations, Broken Symmetry, and Correlation Functions*. Advanced Book Classics. Perseus, 1989.

[98] Gordon Baym and Leo P. Kadanoff. Conservation laws and correlation functions. *Phys. Rev.*, 124:287, 1961.

[99] Gerald D. Mahan. *Many-Particle Physics*. KA/PP, third edition, 2000.

[100] D. Belitz and T. R. Kirkpatrick. Electronic transport at low temperatures: Diagrammatic approach. *Physica E*, 42:497, 2009.

[101] A. H. Wilson. *The Theory of Metals*. Cambridge University Press, Cambridge, 1954.

[102] J. M. Ziman. *Principles of the Theory of Solids*. Cambridge University Press, Cambridge, 1972.

[103] T. R. Kirkpatrick, D. Belitz, and Ronojoy Saha. Theory of helimagnons in itinerant quantum systems iv: Transport in the weak-disorder regime. *Phys. Rev. B*, 78:094408, 2008.

[104] Gábor Zala, B. N. Narozhny, and I. L. Aleiner. Interaction corrections at intermediate temperatures: Longitudinal conductivity and kinetic equation. *Phys. Rev. B*, 64:214204, 2001.

[105] Henrik Bruus and Karsten Flensberg. *Many-Body Quantum Theory in Condensed Matter Physics - an Introduction*. Oxford, Oxford, United Kingdom, 2004.

[106] M. E. Peskin and D. V. Schroeder. *An Introduction To Quantum Field Theory*. Westview Press, New York, NY, 1995.

[107] Alexei M. Tsvelik. *Quantum Field Theory in Condensed Matter Physics*. Cambridge University Press, New York, NY, second edition, 2003.

[108] A. A. Belavin and A. M. Polyakov. Metastable states of two-dimensional isotropic ferromagnets. *Sov. Phys. JETP*, 22:245, 1975.

[109] T. P. Cheng and L. F. Li. *Gauge Theory of Elementary Particle Physics*. Oxford University Press, Oxford, United Kingdom, 1984.

[110] Ar. Abanov and V. L. Pokrovsky. Skyrmion in a real magnetic film. *Phys. Rev. B*, 58:R8889, 1998.

[111] A. Knigavko, B. Rosenstein, and Y. F. Chen. Magnetic skyrmions and their lattices in triplet superconductors. *Phys. Rev. B*, 60:550, 1999.

[112] Richard P. Feynman, Albert R. Hibbs, and Daniel F. Styer. *Quantum Mechanics and Path Integrals*. Dover, Mineola, NY, NY, 2010.

[113] G. Blatter, M. V. Feigel'man, V. B. Geshkenbein, A. I. Larkin, and V. M. Vinokur. Vortices in high-temperature superconductors. *Rev. Mod. Phys.*, 66(4):1125, 1994.

[114] C.-C. Joseph Wang, R. A. Duine, and A. H. MacDonald. Quantum vortex dynamics in two-dimensional neutral superfluids. *Phys. Rev. A*, 81:013609, 2010.

[115] Netanel H. Lindner, Assa Auerbach, and Daniel P. Arovas. Vortex dynamics and Hall conductivity of hard core Bosons. 2010.

[116] Esteban Calzetta, Kwan-Yuet Ho, and Bei-Lok Hu. Vortex formation in two-dimensional Bose gas. *J. Phys. B: At. Mol. Opt. Phys.*, 43:095004, 2010.

[117] Esteban Calzetta and Kwan-Yuet Ho. Density profiles of a two-dimensional Bose gas after free expansion. in preparation, 2012.

[118] T. W. B. Kibble. Topology of cosmic domains and strings. *J. Phys. A: Math. Gen.*, 9:1387, 1976.

[119] T. W. B. Kibble. Some implications of a cosmological phase transition. *Phys. Rep.*, 67:183, 1980.

[120] W. H. Zurek. Cosmological experiments in condensed matter systems. *Phys. Rep.*, 276:177, 1996.

[121] Anushya Chandran, Amir Erez, Steven S. Gubser, and S. L. Sondhi. The Kibble-Zurek problem: Universality and the scaling limit. 2012.

[122] R. Feynman and F. Vernon. The theory of a general quantum system interacting with a linear dissipative system. *Ann. Phys.*, 24:118, 1963.

[123] Edwardo Fradkin. *Field Theories of Condensed Matter Systems*. Westview Press, 1998.

[124] Alexander Altland and Ben Simons. *Condensed Matter Field Theory*. Cambridge, Cambridge, England, second edition, 2010.

[125] Philip R. Wallace. *Mathematical Analysis of Physical Problems*. Dover, 1984.

[126] Jørgen Rammer. *Quantum Transport Theory*. Frontiers in Physics. Perseus, 1998.

[127] Hagen Kleinert. *Path Integrals in Quantum Mechanics, Statistics and Polymer Physics*. World Scientific, London, England, 1995.

[128] Michael N. Barber. An introduction to the fundamentals of the renormalization group in critical phenomena. *Phys. Rep.*, 29:240, 1977.